HAL open science

# Overview of the Morphology and Chemistry of Diagenetic Features in the Clay-Rich Glen Torridon Unit of Gale Crater, Mars

Patrick Gasda, J. Comellas, A. Essunfeld, D. Das, A. Bryk, E. Dehouck, S. Schwenzer, L. Crossey, K. Herkenhoff, J. Johnson, et al.

**To cite this version:**

Patrick Gasda, J. Comellas, A. Essunfeld, D. Das, A. Bryk, et al.. Overview of the Morphology and Chemistry of Diagenetic Features in the Clay-Rich Glen Torridon Unit of Gale Crater, Mars. Journal of Geophysical Research. Planets, In press, ⟨10.1029/2021JE007097⟩. ⟨hal-03840928v1⟩

**HAL Id: hal-03840928**

**https://hal.science/hal-03840928v1**

Submitted on 6 Nov 2022 (v1), last revised 27 Dec 2022 (v2)

**HAL** is a multi-disciplinary open access archive for the deposit and dissemination of scientific research documents, whether they are published or not. The documents may come from teaching and research institutions in France or abroad, or from public or private research centers.

L'archive ouverte pluridisciplinaire **HAL**, est destinée au dépôt et à la diffusion de documents scientifiques de niveau recherche, publiés ou non, émanant des établissements d'enseignement et de recherche français ou étrangers, des laboratoires publics ou privés.

Autorisation HAL

HAL Authorization

# Overview of the Morphology and Chemistry of Diagenetic Features in the Clay-Rich Glen Torridon Unit of Gale Crater, Mars

Patrick J. Gasda[1], J. Comellas[1], A. Essunfeld[1], D. Das[2], A. B. Bryk[3], E. Dehouck[4], S. P. Schwenzer[5], L. Crossey[6], K. Herkenhoff[7], J. R. Johnson[8], H. Newsom[6], N. L. Lanza[1], W. Rapin[9], W. Goetz[10], P.-Y. Meslin[9], J. C. Bridges[11], R. Anderson[7], G. David[9], S. M. R. Turner[5], M. T. Thorpe[12], L. Kah[13], J. Frydenvang[14], R. Kronyak[15], G. Caravaca[9,16], A. Ollila[1], S. Le Mouélic[16], M. Nellessen[6], M. Hoffman[6], D. Fey[17], A. Cousin[9], R. C. Wiens[1], S. M. Clegg[1], S. Maurice[9], O. Gasnault[9], D. Delapp[1], A. Reyes-Newell[1]

1) Los Alamos National Laboratory, Los Alamos, New Mexico, USA

2) McGill University, Montreal, Canada

3) University of California Berkeley, CA, USA

4) Université de Lyon, France

5) AstrobiologyOU, School of Environment, Earth and Ecosystem Sciences, The Open University, Milton Keynes, UK.

6) University of New Mexico, Albuquerque, NM, USA

7) U.S. Geological Survey, Flagstaff, AZ, USA

8) Johns Hopkins University Applied Physics Laboratory, Laurel, MD, USA

9) IRAP, Université de Toulouse, CNRS, CNES, Toulouse, France

10) Max Planck Institute for Solar System Research, Göttingen, Germany

11) University Leicester, UK

12) Texas State University; NASA Johnson Space Center, Houston, TX, USA

13) University of Tennessee, Knoxville, TN, USA

14) Globe Institute, University of Copenhagen, Denmark

15) Jet Propulsion Laboratory, Pasadena, CA, USA

16) Laboratoire de Planétologie et Géodynamique, CNRS UMR 6112, Université Nantes, Université Angers, 44322 Nantes, France.

17) Malin Space Science Systems

**Key Points**

- Glen Torridon in Gale crater underwent multiple generations of diagenesis of the bedrock, which widely varies in chemistry and morphology
- We hypothesize that an initial enrichment of elements occurred during the Gale's post-impact hydrothermal alteration phase of evolution
- We estimate that at least one type of vein in Glen Torridon required warm temperatures and highly reducing and alkaline fluid to form

**Abstract**

The clay-rich Glen Torridon region of Gale crater, Mars, was explored between sols 2300 and 3007. Here, we analyzed the diagenetic features observed by *Curiosity*, including veins, cements, nodules, and nodular bedrock, using the ChemCam, Mastcam, and Mars Hand Lens Imager instruments. We discovered many diagenetic features in Glen Torridon, including dark-toned iron- and manganese-rich veins, magnesium- and fluorine-rich linear features, Ca-sulfate cemented bedrock, manganese-rich nodules, and iron-rich strata. We have characterized the chemistry and morphology of these features, which are most widespread in the higher stratigraphic members in Glen Torridon, and exhibit a wide range of chemistries. These discoveries are strong evidence for multiple generations of fluids from multiple chemical endmembers that likely underwent redox reactions to form some of these features. In a few cases, we may be able to use mineralogy and chemistry to constrain formation conditions of the diagenetic features. For example, the dark-toned veins likely formed in warmer, highly alkaline, and highly reducing conditions, while manganese-rich nodules likely formed in oxidizing and circumneutral conditions. We also hypothesize that an initial enrichment of soluble elements, including fluorine, occurred during hydrothermal alteration early in Gale crater history to account for elemental enrichment in nodules and veins. The presence of redox-active elements, including Fe and Mn, and elements required for life, including P and S, in these fluids is strong evidence for habitability of Gale crater groundwater. Hydrothermal alteration also has interesting implications for prebiotic chemistry during the earliest stages of the crater's evolution and early Mars.

**Plain Language Summary**

The NASA *Curiosity* rover explored the ancient lakebed rocks within the Glen Torridon region of Mars from January 2019 to January 2021. The rover observed many signs that the bedrock was changed by groundwater, especially in the higher elevations along the rover's path. We used data from the rover's ChemCam instrument to record chemistry, and images from four cameras on the rover to look for physical changes to the rocks. When the rock in Glen Torridon was altered by groundwater, it introduced a variety of physical and chemical changes to the rock, and the amount of some elements (sodium, calcium, iron, magnesium, or manganese) increased in the rocks in association with these physical changes to the rocks. We can use these changes in the rock's characteristics to determine the type of water that changed these rocks on Mars (its chemical composition, its temperature, acidic versus basic, oxidizing versus reducing) at the time that the changes occurred. We found that many types of groundwater mixed at different times to cause changes to the rocks. At least one of the groundwater types was warmer than what was previously expected and could be related to the impact that formed the crater.

## 1. Introduction

Diagenetic features are important tracers of past aqueous environments. These features include fracture fills (veins), concretions or nodules, changes of color, and cementation. The chemistry of these features and their effects on the chemistry and mineralogy of the surrounding bedrock can help constrain the salinity, pH, and redox of the ground and surface fluids that emplaced these materials. Their morphologies and their cross-cutting relationships can constrain the timing and duration of these events. Within Gale crater, Mars, the *Curiosity* rover has observed a large variety of diagenetic features with respect to chemistry, mineralogy, and morphology. The ground and surface fluid chemistry and duration of aqueous alteration both have important implications for the long-term habitability of Gale crater and Mars.

### *1.1 Geological Setting of Gale Crater*

Gale crater is a ~155 km wide crater straddling the Southern Highlands and Northern Lowlands dichotomy in equatorial Mars (Milliken et al., 2010; Fraeman et al., 2016). The NASA *Curiosity* rover landed in Gale crater in 2012 and has since then traversed through what is interpreted as a series of eolian, fluvial deltaic, and lacustrine deposits on its way up to the central sedimentary mound, Aeolis Mons, informally named "Mount Sharp," that potentially surrounds or buries a central uplift (Cabrol et al., 1999; Edgett and Malin, 2001; Milliken et al., 2010; Schwenzer et al., 2012; Grotzinger et al., 2014; 2015; Banham et al., 2018; Stack et al., 2019; Edgar et al., 2020). Gale crater also likely hosted a redox stratified habitable lake in its past (Hurowitz et al., 2017), followed by an extensive, long-lived, and habitable groundwater system (e.g., Frydenvang et al., 2017).

Mount Sharp group deposits (Murray and Carolyn Shoemaker formations; Figure 1) are interpreted as primarily lacustrine. The lake was fed by a fluvial deltaic system and these materials are represented by the Bradbury Group (Grotzinger et al., 2015; Edgar et al 2018; Stack et al., 2019; Bedford et al., 2019). The Murray was first encountered on Mars solar day (sol) 680, and it is primarily composed of laminated mudstone that generally represents suspension fallout in a lacustrine setting, with some sandstone intervals and lake margin facies (Grotzinger et al., 2015; Stack et al., 2019; Rivera-Hernandez et al., 2019; 2020; Edgar et al., 2020; Fedo et al., 2017; 2018; Gwizd et al., 2018; 2019; Hughes et al., 2020; Bennett et al., 2022). Unconformably overlying the Mount Sharp group is the Siccar Point group, comprised of the eolian Stimson formation that is mafic in composition (Banham et al., 2018; Bedford et al., 2020; 2022) (Figure 1). Notably, the Hartmann's Valley through Sutton Island members of the Murray formation show evidence for desiccation and evaporation that are interpreted as fluctuations in lake level, drying on the margins of a lake, or a braided river deltaic system (e.g., Stein et al. 2018; Fedo et al., 2017; 2018). This evidence includes altered clay mineralogy (Bristow et al., 2018), elevated evaporitic elements (Gasda et al., 2017; Achilles, 2020; Thomas et al., 2019; Rapin et al., 2019; Das et al., 2020), desiccation cracks (Stein et al., 2018), and intervals of possibly eolian and lake margin depositional settings (Fedo et al., 2017; 2018; Gwizd et al., 2018; 2019; Edgar et al., 2020). Strata above Sutton Island (Blunts Point, Pettegrove Point, and Jura) likely represent lacustrine settings. The Pettegrove Point and Jura members have been overprinted by a later diagenetic event that may have formed the Vera Rubin ridge topographic feature (Rivera-Hernandez et al., 2020; Edgar et al., 2020; Fraeman et al., 2020a; 2020b; Thompson et al., 2020; Frydenvang et al., 2020; Rampe et al., 2020; Turner et al. 2021).

Figure 1: The general stratigraphic column Gale crater (left) and the detailed stratigraphic column of Glen Torridon (center; provided by the MSL sed/strat working group) with plots at the right showing the presence of diagenetic features vs elevation (meters) split into two sections, or traverses. Traverse 1 covers sol 2300–2823 and Traverse 2 covers 2824–3007. Major localities along each traverse are labeled to the right of each traverse plot. The symbols represent different diagenetic features, categorized based on the strongest chemical enrichment (see legend at right). Special veins include linear features and dark-toned veins (see Section 3.6 for details).

*1.2 Glen Torridon: The Clay-Bearing Unit*

South of Vera Rubin ridge lies the clay-bearing unit, informally named "Glen Torridon" (Bennett et al., 2022; Stack et al., 2022; Hughes et al., 2020). Glen Torridon, and the overlying sulfate-bearing unit, were mapped from orbit, and Glen Torridon shows strong clay mineral spectral signatures (Milliken et al., 2010; Fraeman et al., 2016). Orbital remote sensing data also shows that the overlying sulfate-bearing strata has a strong Mg sulfate mineral spectral signature (Milliken et al., 2010; Fraeman et al., 2016). Exploring this region of Gale crater was one of the primary drivers for choosing Gale crater as a landing site for the *Curiosity* rover; these strata are hypothesized to represent the transition from a wetter early Noachian or early Hesperian Mars to a drier late-Hesperian or early Amazonian Mars (Milliken et al., 2010; Grotzinger et al., 2012; Fraeman et al., 2016; Dromart et al., 2021).

At the boundary between the clay and sulfate-bearing units, we can potentially address the major hypothesis about water and climate change on Mars. The clay-bearing strata of Glen Torridon may represent a last gasp of wet Mars in Gale before deposition of a potentially primary evaporitic sequence of strata in the sulfate bearing unit (e.g., Bibring et al., 20016; Milliken et al., 2010). Alternatively, the sulfate bearing unit may instead represent a primarily mudstone or sandstone deposit in a fluvial lacustrine setting that has experienced a different set of sulfate-related diagenetic processes than what has previously been observed along the rover traverse. As we have only just entered the lower reaches of the sulfate unit as of this writing, we can only speculate on the fine scale strata of the region above our current location based on long distance imagery (e.g., Rapin et al., 2021; Dromart et al., 2021; Caravaca et al., 2021), and observations from orbit (Milliken et al., 2010; Fraeman et al., 2016). Hence, this paper sets a baseline for diagenesis below the sulfate unit before further exploration of higher Mt Sharp strata.

On sol 2300, *Curiosity* entered Glen Torridon from Vera Rubin ridge. The first and lowest member of Glen Torridon is the phyllosilicate-rich Jura member, followed by the Knockfarril Hill member, and then the Glasgow member. The Jura-Knockfarril Hill transition corresponds to the Murray to Carolyn Shoemaker formation transition (Bennett et al., 2022; Caravaca et al., 2022). The Glasgow member is unconformably overlain by the "Greenheugh pediment" eolian Stimson sandstone, which is part of the Siccar Point group that has been previously observed to overlie other sections of the Mount Sharp group (Figure 1). Analyses of drill samples by the CheMin powdered X-ray diffractometer instrument have shown that the Knockfarril Hill unit drill sample Glen Etive is the most clay-rich member observed to date in Gale crater at 34 wt% (Thorpe et al., 2022). Further, a mineralogical change occurred below the Greenheugh pediment unconformity such that the strata at the Hutton drill location, within the Glasgow member, includes opal-CT, cristobalite, magnetite, and little clay, suggesting a change in the redox environment (Thorpe et al., 2022). Dehouck et al. (2022) and this study identified five major chemical rock types in Glen Torridon by ChemCam: coherent, rubbly, Glasgow, Hutton, and Mary Anning and Groken (MA/GR) bedrock (Dehouck et al., 2022) (Table S1).

A significant aspect of the Glen Torridon alteration mineral products, which has not been definitively identified with CheMin in other rocks within Gale, is the presence of siderite carbonate at up to 2.2% of the whole rock in the Kilmarie drill sample (Rampe et al., 2020; Thorpe et al., 2022; Bristow et al., 2021). The relative paucity of carbonate detected to date on the Mars near-surface, including Gale, is a puzzling aspect of the predicted carbon cycle on

ancient $CO_2$-rich Mars (Ehlmann et al., 2014, Bridges et al., 2019). Thus, the detected presence of carbonates from both CheMin and SAM data (Thorpe et al., 2022; Sutter et al., 2017) is a noteworthy addition to our knowledge of carbonate occurrences in martian materials. We discuss its variable presence in terms of likely multiple stages of diagenesis that Glen Torridon sediments experienced.

This paper primarily focuses on the fine-scale chemistry of the diagenetic features sampled by the ChemCam instrument compared to the surrounding bedrock. We extensively used Mastcam and remote micro imager (RMI) imagery, and Mars Hand Lens Imager (MAHLI) close-ups to classify individual ChemCam points into bedrock, nodules, veins, or other diagenetic features. The high resolution RMI, supplemented with MAHLI images when available, allows us to discriminate between bedrock and fine-scale diagenetic features sampled with the small (300–500 μm) spot size of ChemCam.

*1.3 Diagenesis in Gale crater*

Calcium sulfate veins have been observed almost continuously throughout the traverse in the Murray formation (Nachon et al., 2014; 2017; Rapin et al., 2016; Schwenzer et al., 2016; Gasda et al., 2017; L'Haridon et al., 2018; 2020; Kronyak et al., 2019; Das et al., 2020). Sulfate veins are typically hydrated, consistent with bassanite (Rapin et al., 2016; Vaniman et al., 2018). Within strata that indicates climatic drying in the crater, enrichment of B and Li was observed in Ca-sulfate veins (Gasda et al., 2017; Das et al, 2020), Mg and S in bedrock (Rapin et al., 2019), and Na and Cl in bedrock and veins (Thomas et al., 2019; Achilles et al., 2020). Desiccation cracks were also observed in this area (Mangold et al., 2017; Stein et al., 2018). Rarely within the Murray, veins occur with dark-toned FeO-rich clasts that sometimes coincide with elevated Mn, Mg, and P (Kronyak et al., 2019; L'Haridon et al., 2018; 2020; Meslin et al., 2018; Sun et al., 2019; David et al., 2020). Vein morphology is heterogeneous. At outcrop scale, veins can be massive, nodular, bowl-shaped, boxwork, resistant to erosion, and/or sub-horizontal; though most veins are hairline, some thicker veins display textures including toothy, fibrous, or nodular textures (Siebach et al., 2014; Nachon et al., 2014; 2017; Schwenzer et al., 2016; Gasda et al., 2017; Kronyak et al., 2019; Das et al., 2020).

Other types of veins have been observed in the crater, including silica-rich halos, MnO-rich veins, and MgO-rich veins (Leveille et al., 2014; Lanza et al., 2016; Frydenvang et al., 2017; Yen et al., 2017; Czarnecki et al., 2020). Silica-rich halos frequently associated with Ca-sulfate veins occur along fractures in Marias Pass Murray and overlying Siccar Point bedrock (Frydenvang et al., 2017; Yen et al., 2017; Czarnecki et al., 2020). Manganese-rich veins were observed in the Kimberley, a part of Bradbury Group (Lanza et al., 2016). Mn-rich fluids potentially formed cements in Bradbury (Comellas et al., 2021) and nodules in Murray (e.g., Meslin et al., 2018). Dark-toned fins and other veins have been observed occasionally throughout the traverse (Nachon et al., 2017; Kronyak et al., 2019).

Nodular or concretionary textures have been observed along the traverse in specific locations (Siebach et al., 2014; Wiens et al., 2017; L'Haridon et al., 2018; Meslin et al., 2018; Sun et al., 2019; David et al., 2020). Small nodules and hollows were observed in Yellowknife Bay (Siebach et al., 2014), and potentially diagenetic concretionary voids were observed in the Bradbury Formation (Wiens et al., 2017). Raised, resistant, and dendritic nodules were observed

in Pahrump Hills in the Murray formation (Minitti et al., 2019), while Sutton Island and Blunts Point nodules were typically dark-toned, embedded, and rounded (Sun et al., 2019). Angular dark-toned clasts associated with sulfate features were observed in Murray through to the Vera Rubin ridge (L'Haridon et al., 2018; 2020) as well as dark-toned nodules surrounded by gray Fe-poor bedrock (David et al., 2020).

Color changes in the bedrock have been observed that typically correspond to changes in chemistry or mineralogy. On Vera Rubin ridge, a color change that cross cuts bedding is interpreted as a redox or diagenetic front (David et al., 2020; Thompson et al., 2020; Frydenvang et al., 2020; Fraeman et al., 2020a; 2020b; Horgan et al., 2020). The crystalline gray hematite discovered in Vera Rubin ridge drill samples is interpreted to have formed in a long-lived aquifer, providing time to form larger crystals (Rampe et al., 2020; Morris et al., 2020). Darker-toned bedrock has been attributed to precipitation of phases including Mn oxide and Mg sulfate via diagenesis (Gasda et al., 2019; Rapin et al., 2019). Likewise, lighter-toned bedrock is attributed to deposition of silica or Ca-sulfate cements due to elevated silica, or CaO and S in the bedrock, respectively (Frydenvang et al., 2017; Newsom et al., 2017; Nellessen et al., 2019; Czarnecki et al., 2020).

In summary, all of these features, including veins, nodules, and color changes, are associated with diagenesis in Gale crater. These diagenetic features are evidence for an extensive and long-lived groundwater system that expands the window of habitability to the subsurface well after surface water retreated from the surface of Mars, due to the presence of redox-active elements (e.g., Fe, Mn, S), and elements required for life (e.g., S and P). Both early and late diagenetic events may have occurred to account for these observations (e.g., Turner et al., 2021). Observations have been made for both earlier cements (e.g., Newsom et al., 2017; Rapin et al., 2019; Nellessen et al., 2020; Comellas et al., 2021; Smith et al., 2021) and later sulfate filling fractures (e.g., Nachon et al, 2014; 2017; Lanza et al., 2016; Horgan et al., 2020). This hydrologic system was highly variable in its chemistry, which implies that it occurred in multiple events, with likely intervals of evaporation or freezing followed by recharge with new fluids, and remobilization of prior deposits, to form new deposits (e.g., Schwenzer et al., 2016).

## 2. Methods

### *2.1 Instruments*

The ChemCam instrument suite is composed of the RMI and a Laser-Induced Breakdown Spectroscopy (LIBS) instrument (Wiens et al., 2012; Maurice et al., 2012). LIBS is a technique that uses a laser to ablate the surface of a material, atomizing and ionizing the elements therein, which forms a plasma. The excited elements and ions then relax and emit quantized atomic emission, which is collected by the spectrometer. ChemCam is a standoff instrument, which means that it uses a telescope to focus the 1067 nm laser to a 300–500 μm spot size and collect the resultant spectra from up to 7 m away. ChemCam typically fires 30 shots per observation point and collects a raster of at least five observation points (Wiens et al., 2015; Maurice et al., 2016). For each observation point, the last 25 shots are averaged into a single spectrum, while the first 5 points are excluded due to contamination from the surface dust. The RMI is a camera that can resolve the LIBS spot to record before and after images of the target, and provide context of each LIBS target (Le Mouélic et al., 2015).

ChemCam LIBS spectra provide chemical information about the target. The spectra are calibrated and pre-processed using the method described by Wiens et al. (2013). All spectra used in this study are available from the Planetary Data System (https://pds-geosciences.wustl.edu/missions/msl/chemcam.htm). Using the spectra collected by ChemCam on Mars, the onboard calibration targets (Fabre et al., 2011; Vaniman et al., 2012), and a large suite of standards collected on the nearly identical ChemCam engineering unit at Los Alamos National Laboratory, the ChemCam instrument on Mars can quantify the major rock-forming element oxides ($SiO_2$, $TiO_2$, $Al_2O_3$, Total FeO, MgO, CaO, $Na_2O$, and $K_2O$) using multivariate analysis techniques (Clegg et al., 2017). Univariate and multivariate calibration models have been developed for other elements including Li, Rb, Sr, Ba (Ollila et al., 2014; Payré et al., 2017a), and Mn (Gasda et al., 2021), using the same suite of standards, plus standards specific to the particular elements of interest. For some elements, ChemCam has a semi-quantitative calibration (e.g., H (Schröder et al., 2015; Rapin et al., 2017; Thomas et al., 2020)), or if there is no calibration to quantify an element, the element can still be detected in some spectra. For these elements, the relative amount of an element can be determined by comparing relative peak heights or areas in the spectra obtained in Gale crater to each other or laboratory spectra. This method has been used for the elements B (Gasda et al., 2017), S (Rapin et al. 2019; Clegg et al., 2020), Zn (Lasue et al., 2016), Cu (Payré et al., 2019; Goetz et al., 2022), Ni (Meslin 2017; 2019), Cr (Ollila et al., 2017), P (Meslin et al., 2018), and Cl (Thomas et al., 2019). In particular, Li has a calibration range up to 72 ppm (Payré et al., 2017a), but we observe targets in Glen Torridon that have predicted compositions outside of this range. Hence, we have developed an expanded model for Li up to 580 ppm for this work, and the details are included in Supplementary Text S7. LIBS on Mars is not suitable for C line detection, due to $CO_2$ in the atmosphere; hence, we cannot use ChemCam data here to directly characterize C for carbonate mineralogy identified by CheMin XRD (Thorpe et al., 2022; Rampe et al., 2020).

The Mastcam imagers consist of two color cameras of fixed focal lengths at 34 and 100 mm (M34 and M100, respectively). They are co-located near the top of the rover mast and can collect stereo pairs (Malin et al., 2017).

MAHLI is a 2-megapixel color camera mounted on the turret on *Curiosity's* robotic arm that can acquire images at working distances from ~2 cm to infinity (Edgett et al., 2012; 2015; Yingst et al., 2016, Malin et al., 2017). Most images span a range of spatial resolution of ~16–100 µm/pixel. Close approach images, from ~2 cm distance to a target, have a resolution of ~16–22 µm/pixel, and are usually sufficient to resolve very fine to coarse grain sizes, but the proportions of clay versus silt particles cannot be distinguished. In cases of strong contrast between grains (for example, light-toned sulfate and reddish clay particles), silt particles as small as 35±7 µm can be distinguished (Figures 14 and 15 of (Edgett et al., 2017)).

### *2.2 Definitions*

For this manuscript, we use terms that are sometimes used interchangeably in the literature. "Fluids" in this manuscript typically refers to a specific groundwater chemistry or set of groundwater conditions that existed in some time or place. "Early" diagenesis is defined as diagenesis that occurred when Gale lake was active and before sediments were lithified, while "late" diagenesis is defined as diagenesis that occurs after lithification. "Primary" processes also occur while the lake was active (e.g., precipitation of evaporites from a lake) and "secondary"

processes are those that rework primary deposits (e.g. remobilization or re-precipitation). "Nodules" are used here to be a general description of any angular to rounded features in the rock surrounded by bedrock matrix, and a "nodular texture" is used in a general sense to describe the type of rock that has a bulbous surface texture. This does not imply any formation mechanism. "Concretions" here does imply a specific formation via mineral precipitation during early diagenesis (see Discussion). "Cement" is also a broadly used term given the limitations of these datasets (described below). The "cements" could be true cements, filling pores in coarse-grained sediment, or small grains disseminated in pore spaces of the bedrock. "Veins" are used as a shorthand for mineralized fracture fills, and "cross-cutting veins" specifically cross-cut bedrock layers, nodules, and/or other veins.

We describe ChemCam observation points that hit a diagenetic feature as either "not enriched" or "enriched" in a particular oxide as determined by ChemCam. For enrichments, we use a strict criterion based on a statistical comparison of the composition of the individual observation point with the median composition of the local bedrock (Table S1), and their respective RMSEP values corresponding to 1 sigma accuracy of the root mean squared error of the predicted composition value (Clegg et al., 2017; Gasda et al., 2021). If ((observation point oxide value) – $RMSEP_{point}$) ≥ ((bedrock median value) + $RMSEP_{bedrock}$)), then this observation point is enriched; if not, then this point is not enriched. The median bedrock value used is based on the type/location of the target and its corresponding chemical endmember (coherent; rubbly; Groken/Mary Anning; Hutton; Glasgow). We expect large differences in the mineralogy between that of diagenetic materials and the bedrock; thus, a stricter criterion based on RMSEP, rather than instrument precision, is necessary for this study. Within Glen Torridon, we observed the largest variations in composition for the oxides: $Na_2O$, MgO, CaO, MnO, and $FeO_T$, and these oxides were used in the database (Gasda et al., 2022; described in Supplement Text S1) to determine enrichments. The oxide with the "strongest enrichment" of an observation point is the oxide that has the highest degree of enrichment determined by the ratio of the observation point oxide composition (wt.%) and the median bedrock oxide composition value (wt.%) (Table S1).

*2.3 Identifying Features*

We used data from a combination of *Curiosity* instruments: ChemCam spectra, ChemCam RMIs, Mastcam, and MAHLI images, to identify diagenetic features in Gale crater. Initially, we looked at each RMI image colorized with Mastcam M100 images and determined if a diagenetic feature was present in the image. If MAHLI images were also acquired for a target, these images were also used to determine the category of a particular observation point. Almost every ChemCam LIBS target has an associated Mastcam M100 image, but the cross-targets with MAHLI is a limited dataset. All Mount Sharp group targets in Glen Torridon are classified in the supplemental database (described in Supplement Text S1), and provided with metadata (Gasda et al., 2022). ChemCam targets were sorted by feature type, including nodular bedrock, nodules, veins, dark strata, and cemented (Gasda et al., 2022). Each of these categories are further broken down by their chemistry and placed in separate subsheets along with their chemistry (Gasda et al., 2022). Only Mount Sharp group targets are included in the database; dark-toned float rocks, pediment rocks, and regolith targets have been excluded. Out-of-focus points and points in shadow are also excluded.

First targets were sorted by morphology, then individual ChemCam observation points were sorted if they directly hit a type of feature, and then these features were subdivided by their chemistry. If a vein or nodule was visible in the RMI, but was not hit directly by the laser, we categorized that target as having a "diagenetic feature." If nodules were visible in the RMI, but the ChemCam laser did not directly hit nodules, these targets were categorized as "nodule-rich bedrock." These nodule-rich bedrock targets can be compared with potentially unaltered, non-nodular bedrock. If a ChemCam laser spot hit a nodule directly, these individual ChemCam observation points were categorized as "nodule points." If the laser directly hit a fracture-filling vein, these observation points were categorized as "veins." Frequently, vein and nodule observation points partially hit bedrock, and while the chemistry of these targets frequently have a mixed composition, we still consider these vein or nodule targets in this work. Typically, veins are embedded in bedrock or are erosion-resistant fins of material protruding from bedrock. Some features were categorized as "dark-toned veins" or "linear features" when these were features surrounded by sand, where it becomes difficult to determine whether these features are truly veins.

On Mars, we are limited to features that we can observe in MAHLI images, typically at the tens of micrometer scale, and the chemical interrogation spot size for ChemCam, in the 100s of micrometer scale. Murray mudstone and siltstone grainsizes are usually smaller than the resolution of images. Without thin sections, it is difficult to understand whether changes in the bedrock chemistry correspond to a cement or merely changes to the chemistry of the sediment itself. For cements in particular, if we suspect there is a cement based on the chemistry (e.g., elevated Fe or Ca), we looked for changes in rock color, whether a cemented rock has any veins in it, and whether there are dark-toned or light-toned features embedded in the rock. If we can reasonably rule out these features based on images, then these changes in chemistry (elevated MnO, FeO, CaO and S, etc) could be a cement. However, it is noted that cements could be extremely thin veins that are unresolved in RMI and MAHLI images. If we observed elevated CaO and S or other elements in an observation point, but did not hit a visible vein, we categorized the observation point as "Ca-sulfate cement." Ca-sulfate cements typically coincide with light-toned material that is visible in Mastcam and MAHLI images. Note that some targets do not have a corresponding MAHLI image but have elevated CaO in the bedrock, and these targets are cement candidates. In many cases, these targets have corresponding detections of S, which is stronger evidence of a cement. Darker-toned cements are typically elevated in $FeO_T$. Other cements, e.g., F, MgO, and MnO rich bedrock do not always have an associated color change.

The combination of color images, RMI, and chemistry is important for categorizing features. In many cases, there were targets with a nodular texture, but these targets have no corresponding enrichments or depletions of elements, and/or did not have changes in color. In these cases, we excluded these targets in our database of diagenetic targets or placed them into the nodule-rich bedrock target list, depending on their morphology. These targets may merely be erosional features or chemical differences that are not large enough to be resolved by ChemCam (see Supplement Text S1 and S5).

We are not using a truly random sample of diagenetic features in Glen Torridon because we used RMI and MAHLI images for this analysis. Rover stops, where observations were made, are

chosen based on rover traversability between strategic waypoints chosen by scientists on the *Curiosity* rover team. Sample targets are then chosen by scientists on the team. While we attempt to target typical bedrock using low resolution images, the way that rovers drive and humans control how and which targets to sample at higher resolution can still introduce a bias to the results. Thus, statistics presented in our results are merely the percentage of ChemCam targets that have diagenetic features present, and these statistics may not reflect the true distribution of diagenetic features in Glen Torridon.

## 3. Results

### *3.1 Overview of Glen Torridon*

Figures 1 and 2 show the stratigraphic column and traverse map for the Glen Torridon region in Gale crater. In these figures, we show the locations and elevation of diagenetic features, categorized by type and chemistry. The stratigraphic column is split into two sections. The first section is the traverse from sol 2300 to 2823, which begins as *Curiosity* drove into Glen Torridon from Vera Rubin ridge, and ends just before the Mary Anning and Groken (MA/GR) drill hole site. We excluded the pediment and dark-toned float rocks, which are likely pediment material. The second section is the traverse from sol 2824 to 3007, which includes the MA/GR drill site up through the polygonally fractured unit (see PFU_c unit in Hughes et al. (2020)). We split the traverse into these two sections because, although we did not observe large shifts in bedrock chemistry or stratigraphy, we do observe large differences in the diagenetic feature type and chemistry.

We observed veins, cements, nodules, and nodular bedrock, and six major types of chemistry (Figure 1). The median composition of the nodules, nodular bedrock, veins, and dark strata, split into chemical enrichment types, are summarized in Tables 1-3, respectively. Note that while a large majority of CaO-rich features are associated with sulfur in Glen Torridon, phosphorous and fluorine were detected as a major component in many CaO-rich features primarily in the Glasgow member (Table 1; Forni et al., 2020; 2021; Dehouck et al., 2022). $Na_2O$ features are associated with either sulfur or chlorine (Table 1). Rare features observed include nodules with halos, MnO- and $FeO_T$-rich veins, and MgO- or CaO- and F-rich vein-like 'linear feature' targets (Table 3). Only one of the haloed targets had significantly different chemistry from the bedrock. Rare veins were only observed at the top of Western butte and near the Hutton drill sample location.

Table 1: Median chemical composition, absolute deviation, and Root Mean Squared Error of Prediction (RMSEP) of nodule observation points in Glen Torridon.

| Category | | Nodules | | | | | | | | | | | | | | | | |
|---|---|---|---|---|---|---|---|---|---|---|---|---|---|---|---|---|---|---|
| Endmember | | Coherent | | | Rubbly | | | Hutton | | | | Glasgow | | | | | Groken/MA | |
| Strongest Enrichment | | $Na_2O$ | CaO | MnO | MgO | CaO | MnO | MgO | CaO | MnO | $FeO_T$ | $Na_2O$ | MgO | CaO | MnO | $FeO_T$ | CaO | MnO |
| | N[a] | 1 | 7 | 1 | 1 | 2 | 20 | 6 | 5 | 1 | 1 | 3 | 3 | 14 | 7 | 14 | 4 | 83 |
| | Median | 57.20 | 44.00 | 47.60 | 46.50 | 43.25 | 48.10 | 43.00 | 34.10 | 13.90 | 36.10 | 52.70 | 52.60 | 39.75 | 48.50 | 42.30 | 40.65 | 45.70 |
| $SiO_2$ (wt%) | AbsDev[b] | - | 3.51 | - | - | 9.75 | 2.00 | 2.08 | 8.62 | - | - | 0.37 | 2.53 | 7.36 | 2.26 | 2.96 | 10.72 | 3.58 |
| | RMSEP | 5.20 | 5.10 | 4.90 | 5.00 | 5.70 | 5.00 | 5.15 | 6.30 | 6.80 | 6.00 | 5.00 | 5.00 | 5.50 | 5.00 | 5.20 | 5.40 | 5.00 |
| | Median | 0.84 | 0.83 | 1.09 | 0.80 | 0.86 | 0.90 | 0.78 | 0.73 | 0.57 | 0.81 | 0.88 | 0.80 | 0.76 | 0.94 | 0.85 | 0.78 | 0.90 |
| $TiO_2$ (wt%) | AbsDev | - | 0.03 | - | - | 0.16 | 0.05 | 0.03 | 0.07 | - | - | 0.03 | 0.05 | 0.10 | 0.04 | 0.04 | 0.17 | 0.08 |
| | RMSEP | 0.46 | 0.46 | 0.51 | 0.45 | 0.46 | 0.47 | 0.44 | 0.43 | 0.38 | 0.45 | 0.47 | 0.45 | 0.44 | 0.48 | 0.46 | 0.44 | 0.47 |
| | Median | 11.90 | 9.00 | 10.60 | 9.60 | 9.55 | 10.00 | 8.95 | 7.10 | 1.40 | 8.40 | 11.10 | 11.10 | 8.35 | 10.90 | 8.40 | 8.30 | 9.20 |
| $Al_2O_3$ (wt%) | AbsDev | - | 0.57 | - | - | 2.35 | 1.02 | 0.53 | 1.70 | - | - | 0.67 | 1.73 | 1.81 | 0.99 | 0.71 | 2.73 | 1.31 |
| | RMSEP | 3.60 | 3.50 | 3.50 | 3.50 | 3.45 | 3.50 | 3.50 | 3.30 | 2.60 | 3.40 | 3.50 | 3.50 | 3.40 | 3.50 | 3.40 | 3.45 | 3.50 |
| | Median | 12.90 | 19.00 | 19.00 | 20.90 | 22.35 | 21.55 | 20.25 | 27.10 | 37.40 | **35.60** | 21.20 | 13.70 | 20.65 | 18.30 | **28.55** | 15.90 | 18.1 |
| $FeO_T$ (wt%) | AbsDev | - | 2.79 | - | - | 3.05 | 1.87 | 2.28 | 5.76 | - | - | 1.07 | 1.13 | 5.70 | 1.90 | 2.84 | 1.07 | 0.98 |
| | RMSEP | 3.10 | 4.10 | 4.10 | 4.30 | 4.40 | 4.40 | 4.25 | 4.80 | 5.60 | 5.50 | 4.40 | 3.20 | 4.30 | 3.90 | 4.95 | 3.50 | 3.90 |
| | Median | 7.80 | 4.00 | 11.10 | **9.90** | 3.70 | 4.80 | **11.00** | 3.10 | 21.10 | 2.80 | 5.00 | **10.90** | 4.70 | 8.60 | 2.95 | 7.25 | 11.7 |
| MgO (wt%) | AbsDev | - | 1.14 | - | - | 1.10 | 0.87 | 1.02 | 1.62 | - | - | 0.73 | 1.93 | 2.74 | 1.40 | 0.59 | 0.60 | 1.38 |
| | RMSEP | 2.20 | 1.70 | 2.80 | 2.60 | 1.70 | 1.80 | 2.80 | 1.70 | 4.20 | 1.60 | 1.90 | 2.70 | 1.80 | 2.40 | 1.60 | 2.15 | 2.90 |
| | Median | 0.80 | **10.60** | 1.70 | 1.50 | **8.80** | 1.50 | 3.45 | **9.80** | 2.90 | 2.30 | 2.90 | 2.20 | **7.95** | 3.10 | 1.15 | **10.4** | 1.90 |
| CaO (wt%) | AbsDev | - | 2.19 | - | - | 5.30 | 0.48 | 0.42 | 4.10 | - | - | 0.47 | 0.50 | 2.16 | 1.80 | 0.61 | 3.35 | 1.09 |
| | RMSEP | 0.90 | 3.00 | 1.00 | 0.90 | 2.30 | 0.90 | 1.30 | 2.90 | 1.20 | 1.10 | 1.20 | 1.00 | 2.50 | 1.20 | 0.90 | 2.95 | 1.00 |
| | Median | **6.28** | 1.77 | 2.46 | 1.95 | 1.89 | 2.34 | 2.06 | 1.83 | 1.51 | 2.19 | **4.27** | 2.86 | 2.00 | 2.54 | 2.28 | 1.92 | 2.37 |
| $Na_2O$ (wt%) | AbsDev | - | 0.72 | - | - | 0.61 | 0.17 | 0.18 | 0.34 | - | - | 0.10 | 0.43 | 0.42 | 0.22 | 0.35 | 0.54 | 0.20 |
| | RMSEP | 1.06 | 0.65 | 0.61 | 0.63 | 0.62 | 0.61 | 0.62 | 0.63 | 0.65 | 0.62 | 0.74 | 0.62 | 0.62 | 0.61 | 0.62 | 0.62 | 0.61 |
| | Median | 0.88 | 0.79 | 0.69 | 0.62 | 0.91 | 1.06 | 0.62 | 0.46 | 0.05 | 0.40 | 0.92 | 0.82 | 0.50 | 0.87 | 0.94 | 0.36 | 0.50 |
| $K_2O$ (wt%) | AbsDev | - | 0.13 | - | - | 0.50 | 0.16 | 0.17 | 0.21 | - | - | 0.10 | 0.39 | 0.21 | 0.18 | 0.22 | 0.14 | 0.16 |
| | RMSEP | 0.82 | 0.78 | 0.74 | 0.71 | 0.83 | 0.90 | 0.70 | 0.64 | 0.52 | 0.62 | 0.83 | 0.79 | 0.66 | 0.81 | 0.84 | 0.61 | 0.66 |
| | Median | 0.07 | 0.10 | **2.54** | 0.01 | 0.12 | **0.11** | 0.12 | 0.17 | **3.22** | 0.12 | 0.09 | 0.08 | 0.10 | **1.21** | 0.06 | 1.08 | **2.92** |
| MnO (wt%) | AbsDev | - | 0.02 | - | - | 0.04 | 0.01 | 0.02 | 0.04 | - | - | 0.02 | 0.04 | 0.04 | 1.43 | 0.03 | 0.69 | 1.03 |
| | RMSEP | 0.04 | 0.05 | 0.72 | 0.02 | 0.05 | 0.05 | 0.05 | 0.06 | 0.72 | 0.05 | 0.04 | 0.04 | 0.05 | 0.66 | 0.04 | 0.47 | 0.72 |
| | Median | 10 | 11 | 10 | 9 | 13 | 13 | 9 | 10 | <LOQ | <LOQ | <LOQ | 9 | 12 | 12 | 9 | 12 | 9 |
| Li (ppm) | AbsDev | - | 2 | - | - | 0 | 2 | 1 | 3 | - | - | - | 1 | 5 | 3 | 3 | 4 | 3 |
| | RMSEP | 5 | 5 | 5 | 5 | 5 | 5 | 5 | 5 | - | - | - | 5 | 5 | 5 | 5 | 5 | 5 |
| | Median | 49 | 72 | 45 | n.d.[e] | 78 | 84 | 65 | 30 | n.d. | n.d. | 76 | 92 | 64 | 73 | 71 | 35 | <LOQ |
| Rb (ppm) | AbsDev | - | 43 | - | - | 43 | 21 | 18 | 28 | - | - | 23 | 12 | 22 | 24 | 34 | 27 | - |
| | RMSEP | 28 | 30 | 28 | - | 31 | 31 | 29 | 27 | - | - | 30 | 31 | 29 | 30 | 30 | 27 | - |
| | Median | <LOQ[d] | <LOQ | 129 | <LOQ | <LOQ | <LOQ | <LOQ | <LOQ | <LOQ | <LOQ | <LOQ | <LOQ | <LOQ | <LOQ | <LOQ | <LOQ | <LOQ |
| Sr (ppm) | AbsDev | - | - | - | - | - | - | - | - | - | - | - | - | - | - | - | - | - |
| | RMSEP | - | - | 113 | - | - | - | - | - | - | - | - | - | - | - | - | - | - |
| Total Oxides (wt%) | | 104.95 | 91.86 | 99.24 | 93.73 | 93.32 | 92.70 | 92.29 | 86.22 | 83.56 | 90.91 | 103.33 | 97.92 | 86.76 | 97.50 | 89.76 | 88.56 | 95.66 |
| Other Elements Detected[c] | | H;Cr;S | H;Cr;S | H;Cr;P | H;Cr;P | H;Cr;S | H;Cr | H;S(2)[f];Cr | H;Cr;F(1) | H;Ba;S | H;Cr | H;Cr; P(1);Cl(2) | H;Cr | H;Cr(19);S(2); P(6);F(4) | H;Cr; P(2);F(1) | H;Cr | H;Cr;S;P | H;Cr; P(56);S(12) |

a) N = number of ChemCam observation points
b) AbsDev = Absolute deviation of the median; left blank when N = 1
c) A limited number of elements and categories were analyzed
d) <LOQ = element was detected, but at a level less that the limit of quantification for this element or oxide
e) n.d. = not detected in samples
f) If <N points have the element detected, formatted as X(N), where X is the element and N is the number of observation points where this element was detected

Table 2: Median chemical composition, absolute deviation, and Root Mean Squared Error of Prediction (RMSEP) of nodular bedrock observation points in Glen Torridon.

| | Category | Nodular Bedrock | | | | | | | | | | | | | | | | |
|---|---|---|---|---|---|---|---|---|---|---|---|---|---|---|---|---|---|---|
| | Endmember | Coherent | | | Rubbly | | | Hutton | | | | Glasgow | | | | | Groken/MA | |
| | Strongest Enrichment | $Na_2O$ | CaO | MnO | $Na_2O$ | CaO | MnO | $Na_2O$ | MgO | CaO | MnO | $Na_2O$ | MgO | CaO | MnO | $FeO_T$ | CaO | MnO |
| | N[a] | 1 | 22 | 10 | 1 | 8 | 53 | 1 | 4 | 3 | 2 | 4 | 4 | 102 | 4 | 2 | 53 | 61 |
| $SiO_2$ (wt%) | Median | 54.20 | 47.30 | 52.10 | 55.90 | 51.40 | 54.1 | 47.20 | 45.90 | 43.00 | 50.30 | 49.80 | 52.60 | 48.75 | 51.35 | 42.55 | 43.40 | 50.70 |
| | AbsDev[b] | - | 3.44 | 1.32 | - | 4.12 | 1.85 | - | 3.30 | 1.70 | 0.40 | 2.93 | 0.83 | 3.97 | 2.33 | 2.05 | 7.75 | 1.77 |
| | RMSEP | 5.10 | 5.00 | 5.00 | 5.20 | 5.00 | 5.1 | 5.00 | 5.05 | 5.10 | 5.00 | 4.95 | 5.00 | 5.00 | 5.00 | 5.20 | 5.10 | 5.00 |
| $TiO_2$ (wt%) | Median | 0.90 | 0.84 | 0.96 | 0.85 | 0.92 | 0.97 | 0.79 | 0.74 | 0.74 | 0.84 | 0.90 | 0.88 | 0.88 | 0.87 | 0.85 | 0.81 | 0.89 |
| | AbsDev | - | 0.07 | 0.13 | - | 0.11 | 0.06 | - | 0.06 | 0.02 | 0.08 | 0.04 | 0.04 | 0.08 | 0.04 | 0 | 0.12 | 0.06 |
| | RMSEP | 0.47 | 0.46 | 0.49 | 0.46 | 0.48 | 0.49 | 0.45 | 0.43 | 0.43 | 0.45 | 0.47 | 0.47 | 0.47 | 0.46 | 0.46 | 0.45 | 0.47 |
| $Al_2O_3$ (wt%) | Median | 11.30 | 9.40 | 11.50 | 10.8 | 10.70 | 11.7 | 9.90 | 9.60 | 9.10 | 14.05 | 10.85 | 11.8 | 10.35 | 12.30 | 7.85 | 8.70 | 10.40 |
| | AbsDev | 0 | 1.20 | 0.77 | - | 2.92 | 0.7 | - | 1.25 | 0.40 | 0.65 | 0.15 | 0.45 | 1.36 | 0.75 | 0.95 | 1.80 | 0.71 |
| | RMSEP | 3.50 | 3.50 | 3.55 | 3.50 | 3.55 | 3.6 | 3.50 | 3.50 | 3.50 | 3.60 | 3.50 | 3.60 | 3.50 | 3.60 | 3.40 | 3.50 | 3.50 |
| $FeO_T$ (wt%) | Median | 20.10 | 17.20 | 19.55 | 20.50 | 16.85 | 18.6 | 14.40 | 17.25 | 19.20 | 13.25 | 18.95 | 16.7 | 15.65 | 14.10 | **26.55** | 16.40 | 17.40 |
| | AbsDev | - | 1.68 | 0.89 | - | 1.75 | 1.39 | - | 2.05 | 1.33 | 1.95 | 1.55 | 1.68 | 2.02 | 1.88 | 0.05 | 2.37 | 0.67 |
| | RMSEP | 4.20 | 3.75 | 4.15 | 4.30 | 3.65 | 4 | 3.30 | 3.75 | 4.10 | 3.15 | 4.05 | 3.70 | 3.50 | 3.25 | 4.80 | 3.60 | 3.80 |
| MgO (wt%) | Median | 3.50 | 5.30 | 6.05 | 3.20 | 3.35 | 5.7 | 3.40 | **10.30** | 4.30 | 7.95 | 4.25 | **9.35** | 4.25 | 7.40 | 3.15 | 7.40 | 10.70 |
| | AbsDev | - | 0.88 | 1.32 | - | 0.41 | 0.73 | - | 1.08 | 0.20 | 0.45 | 0.90 | 0.48 | 0.99 | 2.48 | 0.35 | 2.02 | 1.01 |
| | RMSEP | 1.70 | 1.90 | 2.00 | 1.70 | 1.70 | 1.9 | 1.70 | 2.65 | 1.08 | 2.25 | 1.75 | 2.45 | 1.80 | 2.20 | 1.65 | 2.20 | 2.70 |
| CaO (wt%) | Median | 0.70 | **9.45** | 3.10 | 1.30 | **5.95** | 1.8 | 2.80 | 3.65 | **13.00** | 5.65 | 1.75 | 2.95 | **8.35** | 6.15 | 1.25 | **10.60** | 1.80 |
| | AbsDev | - | 3.42 | 1.25 | - | 2.39 | 0.49 | - | 1.27 | 1.27 | 0.35 | 0.60 | 0.85 | 3.35 | 1.50 | 0.15 | 5.64 | 0.69 |
| | RMSEP | 0.80 | 2.80 | 1.20 | 0.90 | 1.95 | 1 | 1.10 | 1.30 | 3.20 | 1.90 | 1.00 | 1.15 | 2.60 | 2.00 | 0.90 | 3.00 | 1.00 |
| $Na_2O$ (wt%) | Median | **4.37** | 1.82 | 2.51 | **4.19** | 2.30 | 2.64 | **11.89** | 2.30 | 2.14 | 3.72 | **5.14** | 2.60 | 2.22 | 2.66 | 2.09 | 1.75 | 2.41 |
| | AbsDev | - | 0.35 | 0.19 | - | 0.45 | 0.15 | - | 0.26 | 0.17 | 0.12 | 1.06 | 0.10 | 0.42 | 0.17 | 0.17 | 0.44 | 0.15 |
| | RMSEP | 0.76 | 0.63 | 0.61 | 0.72 | 0.63 | 0.61 | 1.66 | 0.62 | 0.62 | 0.67 | 0.88 | 0.61 | 0.62 | 0.61 | 0.63 | 0.63 | 0.61 |
| $K_2O$ (wt%) | Median | 1.38 | 0.80 | 1.13 | 1.25 | 1.35 | 1.38 | 0.27 | 1.16 | 0.77 | 0.62 | 0.59 | 0.97 | 0.82 | 0.87 | 1.01 | 0.39 | 0.70 |
| | AbsDev | - | 0.24 | 0.22 | - | 0.38 | 0.18 | - | 0.44 | 0.07 | 0.24 | 0.09 | 0.26 | 0.24 | 0.13 | 0.11 | 0.14 | 0.13 |
| | RMSEP | 1.02 | 0.78 | 0.92 | 0.97 | 1.00 | 1.02 | 0.58 | 0.92 | 0.77 | 0.72 | 0.70 | 0.85 | 0.79 | 0.82 | 0.87 | 0.62 | 0.74 |
| MnO (wt%) | Median | 0.05 | 0.10 | **0.34** | <LOQ | 0.06 | **0.09** | 0.04 | 0.16 | 0.14 | **0.26** | 0.06 | 0.15 | 0.08 | **0.18** | 0.10 | 0.30 | **0.88** |
| | AbsDev | - | 0.02 | 0.68 | - | 0.02 | 0.01 | - | 0.04 | 0.01 | 0.02 | 0.03 | 0.02 | 0.03 | 0.02 | 0.05 | 0.11 | 0.58 |
| | RMSEP | 0.03 | 0.04 | 0.11 | - | 0.03 | 0.04 | 0.03 | 0.06 | 0.05 | 0.08 | 0.04 | 0.06 | 0.04 | 0.06 | 0.04 | 0.10 | 0.33 |
| Li (ppm) | Median | 15 | 15 | 14 | 12 | 17 | 15 | <LOQ | 25 | 18 | 31 | 9 | 7 | 13 | 6 | 8 | 14 | 11 |
| | AbsDev | - | 3 | 2 | 0 | 2 | 2 | - | 17 | 2 | 9 | 1 | 4 | 4 | 2 | 4 | 3 | 2 |
| | RMSEP | 5 | 5 | 5 | 5 | 5 | 5 | - | 6 | 5 | 6 | 5 | 5 | 5 | 5 | 5 | 5 | 5 |
| Rb (ppm) | Median | 58 | 77 | 57 | 49 | 85 | 88 | n.d.[f] | 84 | 70 | 51 | 57 | 97 | 71 | 95 | 43 | <LOQ | 45 |
| | AbsDev | - | 37 | 15 | 0 | 6 | 24 | - | 23 | 25 | 51 | 17 | 22 | 23 | 16 | 43 | - | 28 |
| | RMSEP | 29 | 30 | 29 | 28 | 31 | 31 | - | 31 | 30 | 16 | 29 | 32 | 30 | 31 | 16 | - | 28 |
| Sr (ppm) | Median | <LOQ[e] | <LOQ | 146 | <LOQ | <LOQ | 149 | <LOQ | 88 | 112 | 139 | <LOQ | <LOQ | 123 | 124 | <LOQ | <LOQ | <LOQ |
| | AbsDev | - | - | 37 | - | - | 50 | - | 22 | 22 | 14 | - | - | 47 | 60 | - | - | - |
| | RMSEP | - | - | 116 | - | - | 117 | - | 96 | 109 | 115 | - | - | 112 | 105 | - | - | - |
| Total Oxides (wt%) | | 100.87 | 94.03 | 99.75 | 102.18 | 95.18 | 99.62 | 102.58 | 93.36 | 94.53 | 100.36 | 97.43 | 100.60 | 93.57 | 98.54 | 87.49 | 91.50 | 98.29 |
| Other Elements Detected[c] | | H;Cr;P | H;Cr;S(17)[d] | H;Cr; S(1) | H;Cr;Cl | H;Cr;S | H;Cr;S(5) | H;Cr;Cl | H;Cr;S(1) | H;Cr; S;F(1) | H;Cr | H;Cr; Cl(4);P(2) | H;Cr | H;Cr; S(96) | H;Cr;S(3) | H;Cr | H;Cr; S(53);P(4) | H;Cr; S(5);P(9) |

a) N = number of ChemCam observation points
b) AbsDev = Absolute deviation of the median; left blank when N = 1
c) A limited number of elements and categories were analyzed
d) If <N points have the element detected, formatted as X(N), where X is the element and N is the number of observation points where this element was detected
e) <LOQ = element was detected, but at a level less that the limit of quantification for this element or oxide
f) n.d. = not detected in samples

Table 3: Median chemical composition, absolute deviation, and Root Mean Squared Error of Prediction (RMSEP) of veins, linear features, and dark strata observation points in Glen Torridon.

| | Category | Veins/Linear Features | | | | Dark Strata | |
|---|---|---|---|---|---|---|---|
| | Endmember | | | | | Groken/MA | |
| | Strongest Enrichment | CaO[d] | FeO/MnO | MgO/F | CaO/F | MnO | $FeO_T$ |
| | N[a] | 31 | 30 | 26 | 9 | 4 | 5 |
| $SiO_2$ (wt%) | Median | - | -[f] | 46.75 | 1.10 | 44.95 | 40.3 |
| | AbsDev[b] | - | - | 1.82 | 1.01 | 2.1 | 1.01 |
| | RMSEP | - | - | 5.00 | 6.70 | 5 | 5.4 |
| $TiO_2$ (wt%) | Median | - | 0.66 | 0.62 | 0.32 | 0.89 | 0.9 |
| | AbsDev | - | 0.06 | 0.03 | 0.05 | 0.03 | 0.03 |
| | RMSEP | - | 0.41 | 0.40 | 0.29 | 0.47 | 0.47 |
| $Al_2O_3$ (wt%) | Median | - | 2.10 | 10.20 | 1.60 | 9.2 | 7.5 |
| | AbsDev | - | 0.62 | 1.38 | 0.32 | 0.73 | 0.45 |
| | RMSEP | - | 2.70 | 3.50 | 2.60 | 3.5 | 3.4 |
| $FeO_T$ (wt%) | Median | - | **50.75** | 8.65 | 11.20 | 20.45 | **27.6** |
| | AbsDev | - | 2.03 | 2.17 | 1.64 | 0.75 | 1.17 |
| | RMSEP | - | 6.60[g] | 2.50 | 2.80 | 4.3 | 4.9 |
| MgO (wt%) | Median | - | 4.45 | **19.2** | 3.60 | 10.1 | 4.6 |
| | AbsDev | - | 1.43 | 2.94 | 0.50 | 1.09 | 0.47 |
| | RMSEP | - | 1.80 | 3.85 | 1.70 | 2.6 | 1.8 |
| CaO (wt%) | Median | 36.20 | 0.70 | 5.85 | **26.9** | 1.7 | 1.3 |
| | AbsDev | 2.65 | 0.15 | 2.98 | 1.41 | 0.05 | 0.13 |
| | RMSEP | 6.80 | 0.80 | 1.95 | 5.30 | 1 | 0.9 |
| $Na_2O$ (wt%) | Median | - | 1.60 | 0.67 | 0.35 | 2.52 | 1.77 |
| | AbsDev | - | 0.19 | 0.18 | 0.19 | 0.12 | 0.1 |
| | RMSEP | - | 0.64 | 0.46 | 0.35 | 0.61 | 0.64 |
| $K_2O$ (wt%) | Median | - | 0.03 | 3.57 | 0 | 0.42 | 0.33 |
| | AbsDev | - | 0.03 | 1.50 | 0 | 0.09 | 0.05 |
| | RMSEP | - | 0.51 | 1.18 | 0.50 | 0.63 | 0.6 |
| MnO (wt%) | Median | - | **8.60** | 0.15 | 0.34 | **2.77** | 0.11 |
| | AbsDev | - | 2.72 | 0.02 | 0.16 | 1.03 | 0.01 |
| | RMSEP | - | 1.06 | 0.06 | 0.11 | 0.72 | 0.05 |
| Li (ppm) | Median | - | <LOQ[h] | 70 | <LOQ | 9 | 6 |
| | AbsDev | - | - | 44 | - | 1 | 2 |
| | RMSEP | - | - | 7 | - | 5 | 5 |
| Rb (ppm) | Median | - | n.d.[i] | 230 | <LOQ | n.d. | <LOQ |
| | AbsDev | - | - | 157 | - | - | - |
| | RMSEP | - | - | 49 | - | - | - |
| Sr (ppm) | Median | - | n.d. | <LOQ | 216 | <LOQ | <LOQ |
| | AbsDev | - | - | - | 46 | - | - |
| | RMSEP | - | - | - | 130 | - | - |
| Total Oxides (wt%) | | 36.20 | 70.49 | 96.33 | 45.76 | 95.52 | 86.18 |
| Other Elements Detected[e] | | H;S;B(6); Cl(1) | H;Ni;Cl(10); | H;F;Cl(11);Cr | H;F(9);S;Cl(1);Ba(1);Zn(1) | H;Cr;P(2);S(1) | H;Cr;Cu[j] |

a) N = number of ChemCam observation points
b) AbsDev = Absolute deviation of the median; left blank when N = 1
c) A limited number of elements and categories were analyzed
d) Assumed endmember composition calculated from observation points with <0.5 wt% $SiO_2$
e) All Ca-sulfate veins in Glen Torridon have a total of 15 B detections; Formatted as X(N), where X is the element and N is the number of observation points where this element was detected
f) $SiO_2$ values unreliable
g) $FeO_T$ accuracy likely underestimated
h) <LOQ = element was detected, but at a level less that the limit of quantification for this element or oxide
i) n.d. = not detected in samples
j) Goetz et al., 2022

Generally, the stratigraphic columns show that a major shift occurs in the diagenetic chemistry of features from west to east in Glen Torridon that correspond to the two different sections of the traverse. In the first section, Ca-sulfate cemented material is more common, Ca-sulfate and $Na_2O$ nodules and associated bedrock are more common, and there is generally a larger range of nodule chemistry over a large portion of the traverse. An increase of Ca-sulfate and $Na_2O$-rich features occurs at the base of the buttes, coinciding with intervals of sandstone in the bedrock, and continues through to the base of the Greenheugh pediment. The nodular features mostly occur in the lower portion of the Glasgow member. In the second section of the traverse, $Na_2O$-rich material is completely absent, and MnO-rich features become more common. A majority of the MnO-rich features occur at the MA/GR drill sites (see Section 3.7), as the rover spent a long

time at this location, and *Curiosity* also observed a number of MnO-rich features over the traverse up section (an area informally referred to as "The Benches") from this location, and in the PFU. At the approach to the PFU from the west, an increase in nodules was observed, along with some nodules with diagenetic halos. $FeO_T$ nodules were also observed. Within the PFU and the drive away from it to the east, mostly MnO-rich features were observed.

Our observations show that nodules are confined to the KHm and Glasgow member of Glen Torridon. Sulfate-rich features are observed consistently throughout the traverse. Both the sulfates and nodules occur in the upper portions of Glen Torridon except during the ~18 m of elevation between Harlaw Rise and the Central and Western buttes. These gaps are partly due to traverses through pebble-dominated locations (the traverse through the location informally named "Visionarium;" see Bennett et al., 2022). The Glen Etive drill site and the periodic bedrock ridges around the Visionarium (Bennett et al., 2022; Stack et al., 2022) also notably lacked both nodular and sulfate-rich features. Ca-sulfate veins were observed in the RMI of almost all bedrock targets, but veins were never observed in pebbles.

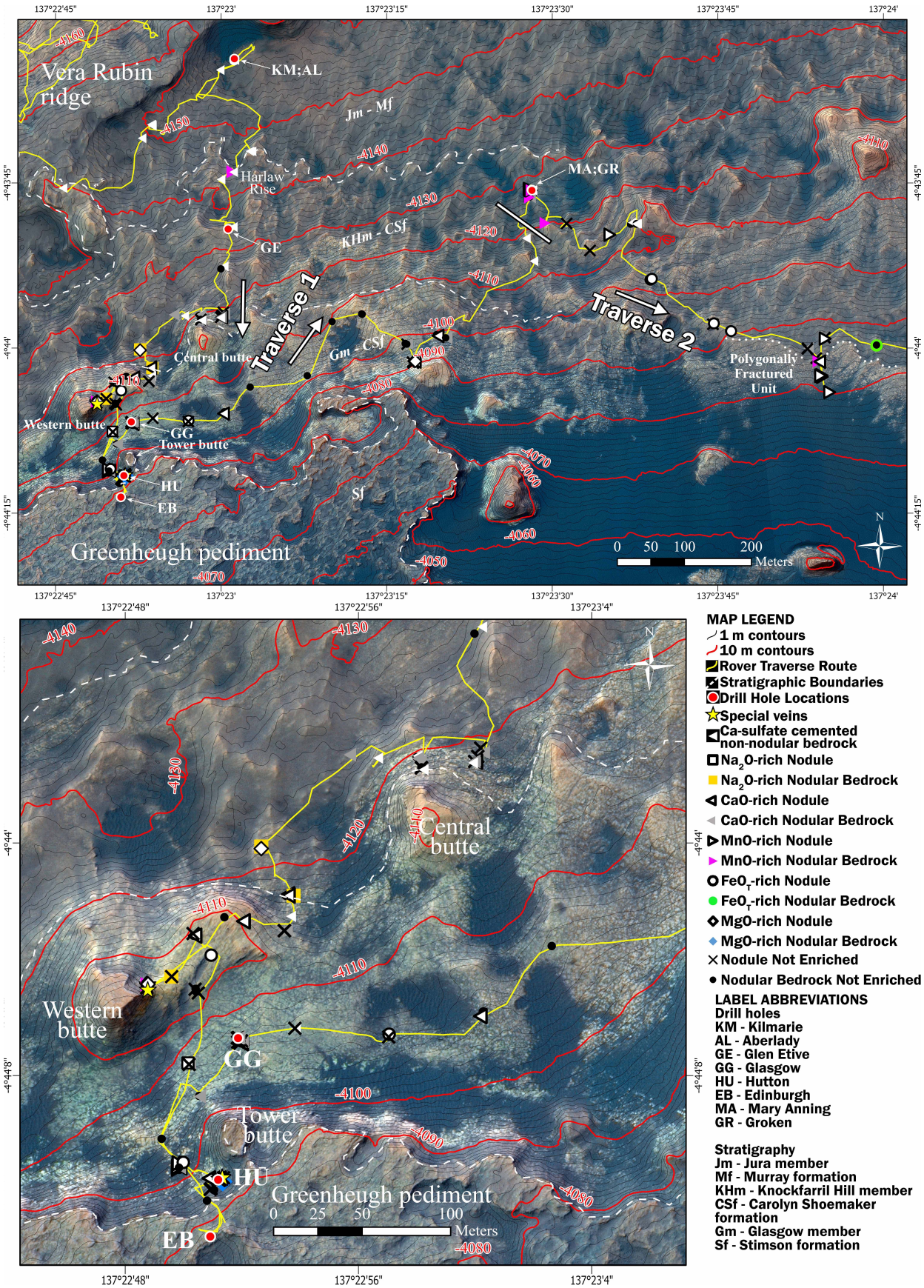
Vera Rubin ridge
KM;AL
Jm - Mf
Hárlaw Rise
MA;GR
GE
KHm - CSf
Traverse 1
Traverse 2
Central butte
Gm - CSf
Polygonally Fractured Unit
Western butte
GG
Tower butte
HU
EB
Sf
Greenheugh pediment
0 50 100 200 Meters
N
Central butte
Western butte
GG
Tower butte
HU
EB
Greenheugh pediment
0 25 50 100 Meters
MAP LEGEND
1 m contours
10 m contours
Rover Traverse Route
Stratigraphic Boundaries
Drill Hole Locations
Special veins
Ca-sulfate cemented non-nodular bedrock
Na2O-rich Nodule
Na2O-rich Nodular Bedrock
CaO-rich Nodule
CaO-rich Nodular Bedrock
MnO-rich Nodule
MnO-rich Nodular Bedrock
FeOT-rich Nodule
FeOT-rich Nodular Bedrock
MgO-rich Nodule
MgO-rich Nodular Bedrock
Nodule Not Enriched
Nodular Bedrock Not Enriched
LABEL ABBREVIATIONS
Drill holes
KM - Kilmarie
AL - Aberlady
GE - Glen Etive
GG - Glasgow
HU - Hutton
EB - Edinburgh
MA - Mary Anning
GR - Groken
Stratigraphy
Jm - Jura member
Mf - Murray formation
KHm - Knockfarril Hill member
CSf - Carolyn Shoemaker formation
Gm - Glasgow member
Sf - Stimson formation

491

Figure 2: A full map (top) of Glen Torridon, and map enlarging the traverse near the buttes Glasgow and Hutton drill hole locations (bottom), showing the traverse and locations where nodules and potential cements were observed, categorized by feature type and strongest enrichment (see legend). Special veins include linear features and dark-toned veins (see Section 3.6 for details). The Traverses shown in Figure 1 are noted on the full map with the white diagonal line to the west of MA/GR indicating where Traverse 1 ended and Traverse 2 begins. The base map was created from HiRISE topography and the topography was created from HiRISE stereo base pairs (Calef and Parker, 2016).

*3.2 Jura member*

The Jura member lacks many of the diagenetic features found in the rest of Glen Torridon. Most bedrock in the Jura host cross-cutting Ca-sulfate veins, similar to the rest of the Murray formation explored thus far in Gale crater. A representative area for these types of veins is the Aberlady/Kilmarie drill site (Fig S1). In six instances within the Jura member, possible Ca-sulfate cement is inferred from chemical observations.

*3.3 Knockfarril Hill member*

The Knockfarril Hill member (KHm) is similar to the Jura member and has limited diversity of diagenetic materials. Most of the KHm is dominated by the typical cross-cutting veins observed in most of Mount Sharp group deposits. However, near the boundaries of KHm, with Jura below and Glasgow above, *Curiosity* observed an increase in nodules, veins, potential cements, and other diagenetic features.

When *Curiosity* visited the KHm at Harlaw Rise, a sandstone deposit (Bennett et al., 2022), ChemCam observed its first dark-toned nodules in Glen Torridon. The Badcall target (Fig S2 and S3) displayed bedding with rounded, in some cases almost spherical, 2–3 mm sized dark-toned 'tear drop' features that extend above the surface of the bedrock. This type of feature suggests that the dark-toned nodules are likely more resistant to wind erosion than the surrounding bedrock. Although the laser did not sample the dark-toned materials in Badcall directly, the nodular bedrock targets at this location were enriched in CaO and MnO (Table 2; coherent). Sulfur is detected in observation points 3–4 of the Badcall target, among the 10 raster points measured with ChemCam LIBS, indicating potential sulfate cement in these points, which do not directly hit veins that cross-cut this outcrop. However, the depth profiles for these are observation points are inconclusive for this target, but potentially show evidence of a cement (Fig S44). Observation point 5 had a detection of phosphorus, but this point is also mixed with a Ca-sulfate vein. The mixed chemistries at this location is likely a consequence of sampling a mixture of bedrock, small nodules, Ca-sulfate veins, and potential cements, rather than hitting one feature directly.

*3.4 Central Butte and Western Butte*

About halfway up the Central and Western buttes, *Curiosity* observed the transition between the KHm and the Glasgow member, which is marked by the last occurrence of cross-stratified sandstone and a dominance of laminated sediments (Figure 1; Bennett et al., 2022; Bryk et al., 2020). At these locations, we observed an increase in raised nodular features and sulfate-rich features, including potential sulfate cements, veins, and light-toned banding between layers. Typically, these raised nodular features are rich in Ca-sulfate, but in a few instances, ChemCam

detected $Na_2O$ and MgO sulfate (Table 1 and 2, coherent, rubbly, and Glasgow). For example, the Hamnavoe target on lower Western Butte had two occurrences of enrichments in MgO, CaO, and $Na_2O$ in angular embedded features (Fig S4), with detectable S peaks in the spectra, and the Na-rich points did not have significant CaO (See Supplement Text S8). The rover observed that many of these targets also had raised, 1–2 mm sized dark-toned nodules, but we were unable to determine the chemistry of these dark-toned features with ChemCam due to their small size, which made them challenging to target with ChemCam.

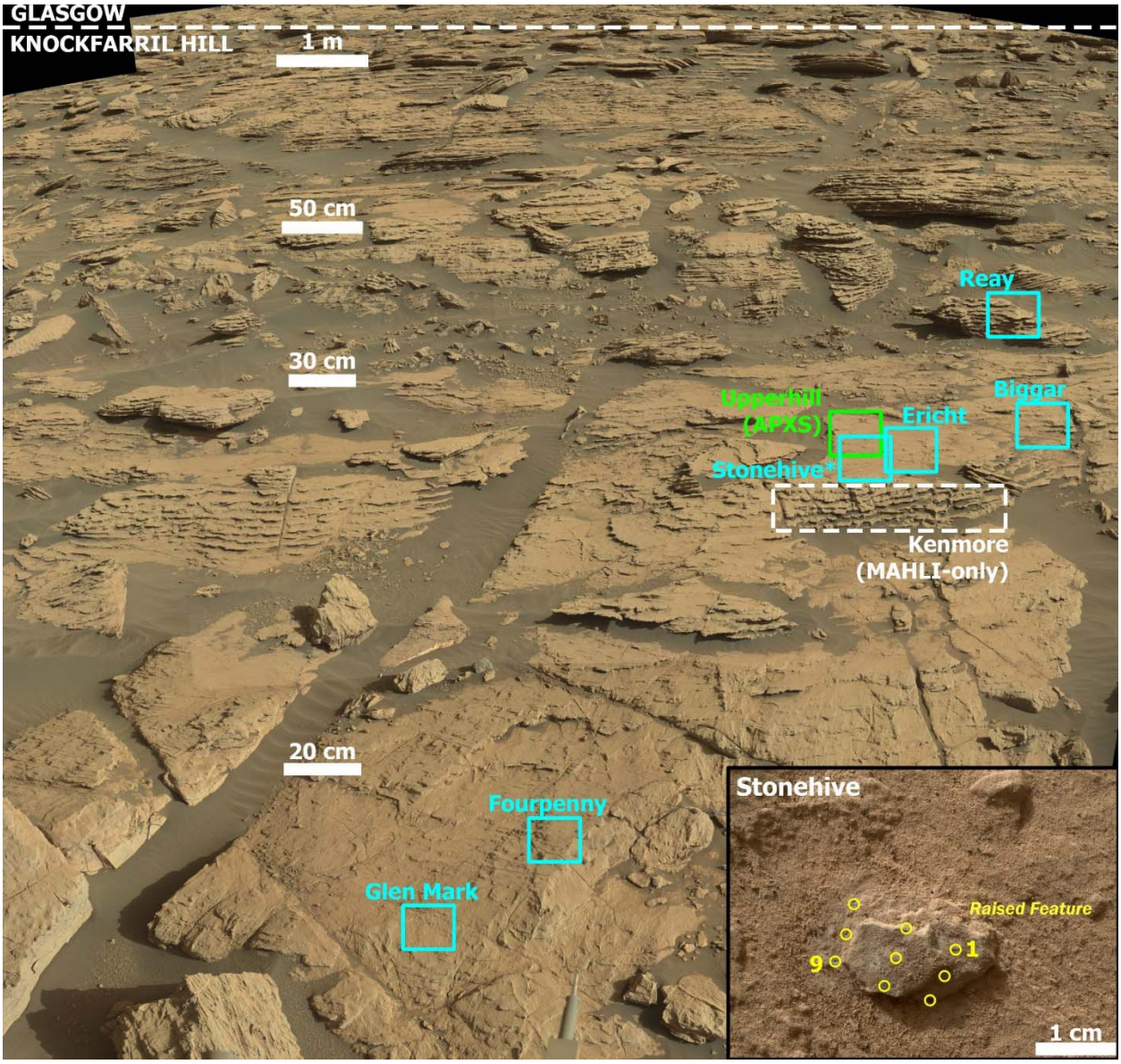


Figure 3: A Mastcam mosaic of the outcrop on Central Butte from sol 2570 showing the locations of targets analyzed from sols 2570–2575. The stratigraphic transition between Knockfarril Hill and Glasgow members is labeled approximately with the dashed white line. Locations of targets are outlines with boxes (ChemCam targets are cyan, Alpha Particle X-ray Spectrometer targets are green, and MAHLI-only targets are white). The Stonehive MAHLI-ChemCam cross target is shown in the bottom right inset with LIBS observation points

annotated. See Supplement Text S8 for a listing of Mastcam and MAHLI dataproducts in this Figure. Base image credit: NASA/JPL-Caltech/MSSS.

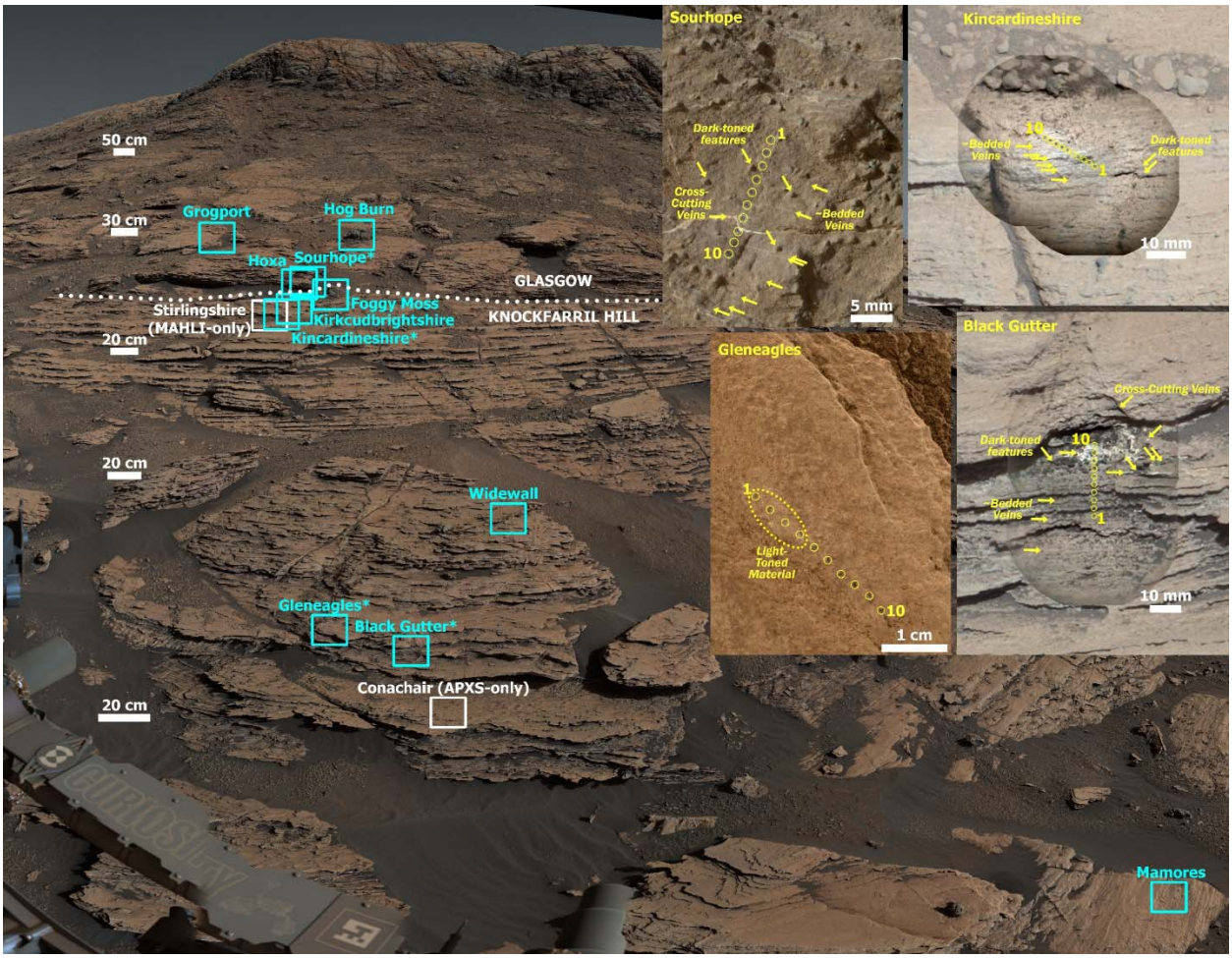


Figure 4: A Mastcam mosaic of the outcrop on Central Butte from sol 2579 showing the location of targets analyzed from sols 2579–2586. The stratigraphic transition between Knockfarril Hill and Glasgow members is labeled approximately with the dotted white line. Locations of targets are outlines with boxes (ChemCam targets are cyan and MAHLI-only targets are white). The top right inset has annotated ChemCam targets (clockwise order, starting top left): Sourhope MAHLI-ChemCam cross target, Kincardineshire ChemCam overlaid on its Mastcam image, Black Gutter ChemCam overlaid on its Mastcam image, and Gleneagles MAHLI-ChemCam cross target. See Supplement Text S8 for a listing of Mastcam and MAHLI dataproducts in this Figure. Base image credit: NASA/JPL-Caltech/MSSS.

Targets analyzed on sols 2570–2575 can be seen on the outcrop on Central Butte (Figure 3; Table 1-2, coherent). From this location, north of the Central butte, the rover is looking up at the transition from the KHm to the Glasgow stratigraphic member. Here, several sulfate-rich features were observed, including three targets with Ca-sulfate rich points: Glen Mark (Fig S5), Fourpenny (Fig S6), and Reay (Fig S7). Stonehive (bottom right Fig 3) is a large (~2 cm sized) Ca sulfate-rich raised feature. Many of the targets displayed the presence of raised and sometimes dark-toned nodules in the bedrock.

At a second Central butte outcrop (Figure 4), the rover sampled a set of targets from just below and above the stratigraphic transition, where many sulfate-rich features were observed (Table 1-2, coherent and Glasgow). Gleneagles (Figure 4 bottom left inset image) is likely a Ca-sulfate cemented target, and the annotated MAHLI image shows that the first four ChemCam observation points in this target have light-toned material embedded in the rock, where ChemCam detects elevated CaO and detects S in observation points 3–4. In outcrop view, the Gleneagles target is part of a resistant feature/layer. Many similar features are observed throughout this outcrop (Figures 3 and 4). Black Gutter is another such target; the first seven observation points hit a series of resistant features that are Ca-sulfate-rich, with observation point 4 hitting a resistant layer that is potentially Ca-sulfate cemented. A mixture of dark-toned nodules and bedrock are observed between the resistant features in Black Gutter. The last three observation points in Black Gutter hit a vein hosting embedded bedrock and dark-toned nodules. Just below Black Gutter, the MAHLI-only Conachair DRT (Dust Removal Tool) target sits on another resistant set of strata on this outcrop. Upon scratching the surface, the DRT revealed many light-toned features (Fig S8). Just below the Glasgow member, the Kincardineshire target exhibits very thin veins that approximately follow bedding or potentially layers of Ca-sulfate, as well as dark-toned features. Just above the contact of KHm and Glasgow, the Sourhope target provides the best example of thin Ca-sulfate veins approximately following bedding and cross-cutting veins. Elevated CaO and S were detected by ChemCam in observation point 9, which sampled one of the light-toned veins/layers. Resistant and raised dark-toned nodules that are 1–3 mm in size were also observed in Sourhope. Note that up to this point of the traverse, we had not sampled any of the raised and resistant dark-toned features with ChemCam. The depth trends for these targets are not conclusive but likely indicate cements are present (Figs S44-S45 and S49). Ca-sulfate cements are likely present given the combination of the observations, including elevated CaO and S detection in a part of the raster that lacks veins, with the fact that these targets are part of a resistant layers within the outcrop, and that light-toned material is observed in MAHLI images.

During the traverse towards Central butte and the traverse between Central and Western buttes, the rover encountered nodular bedrock (Table 1-2, rubbly and coherent). In contrast to prior observations of nodular bedrock up to this point, these targets (e.g., Everbay; Fig S9) had embedded, rather than raised, dark-toned features. The target Everbay also displayed embedded small light-toned features in the MAHLI DRT image (Fig S9). The light-toned features may contain Ca-sulfate, but they were not sampled with the ChemCam laser. In some instances, dark-toned features are arrayed around the light-toned features (Fig S9). The dark-toned features are elongated, and only revealed when the surface is cleared of dust by either the ChemCam laser ablation or the DRT. ChemCam hit one of these dark-toned embedded features in another target ~1m from Everbay (Fidra, Fig S10) and detected elevated MgO compared to rubbly bedrock (Table 1).

*3.5 Glasgow Member*

The Glasgow member is split into two distinct parts based on the bedrock chemical and mineralogical composition. The Glasgow member primarily includes strata surrounding the base of Western and Tower buttes, and skirting the pediment; Glasgow has a composition similar to the KHm and the Jura rubbly endmember composition (Dehouck et al., 2022) (Table S1). The

Glasgow member bedrock at the top of Western butte and on the slopes of Tower butte near the Hutton drill hole > -4100 m is characterized by a lighter-toned bedrock, elevated CaO, $Na_2O$, and MnO, and reduced $SiO_2$ and $K_2O$ (Dehouck et al., 2022) (Table S1). The lower members of Glen Torridon are phyllosilicate-bearing for the most part, where the Glen Etive (KHm) drill hole has the highest abundance of phyllosilicates found in Gale crater (34 wt%), and the Glasgow member drill sample contains 23 wt% phyllosilicates (Thorpe et al., 2022). In contrast, the Hutton drill hole detected significant opal CT and cristobalite, and very little phyllosilicate was detected (Thorpe et al., 2022). Even though in the second section of traverse, the rover climbs above the Hutton elevation, we did not re-encounter this type of bedrock. The bedrock composition observed near Hutton seems to be confined to that location and elevation interval. Hence, we will define "Hutton" as the strata in Traverse 1 between approx. > -4100 m and the pediment unconformity (Figure 1) near the Hutton drill hole (Figure 2), and at the top of Western butte. The rest of the Glasgow stratigraphy, excluding Hutton, will be simply referred to as the Glasgow member.

The strata between ~ -4110 and -4100 m in Glasgow are of particular interest, as we observed a large variety of nodule chemistries (Figure 1 Traverse 1; Table 1-2). The first instance where ChemCam directly hit a dark-toned raised feature anywhere in Glen Torridon was the target Balgy (Fig S11), where elevated $FeO_T$ was observed. Over this ~10 m interval, we observed nodules of every chemical type described in this paper. In addition, these strata had more instances of potentially cemented bedrock (Figs S48-S55). At the Glasgow drill location specifically, with one exception, ChemCam did not detect any significant difference between the nodules, the nodular bedrock, and nodule-free bedrock. We observed a variety of morphologies of nodular features, including small embedded dark-toned features, in the Glasgow drill target (Fig S12), raised and resistant dark-toned features in Troon (Fig S13), Large Island (Fig S14), and Loch Olabhat (Fig S15), where observation point 3 hit the only $FeO_T$-rich feature at this drill location. The difference between these three targets' expressions of the nodules seems related to differences in relative resistance to erosion.

At one particular rover location, just below the Hutton interval (~ -4100 m), ChemCam observed every chemical type of nodule in a single outcrop (Figure 5). Although the bedrock composition at this location has some characteristics of Hutton (lighter-toned bedrock), it is downslope from Hutton, and the abundance of nodules suggests this bedrock is more similar to Glasgow bedrock. Hence, we used Glasgow as the reference composition for major enrichments for targets in Figure 5. Nodule chemistries sampled in Figure 5 include the targets Bonxie ($FeO_T$), Beinn an Dudhaich (CaO, $Na_2O$, and $FeO_T$), Ben Wyvis (MgO and CaO ±F and P), and Peach (MnO) (Table 1, Glasgow). The bedrock shown in Figure 5 is nodular with dark-toned resistant features, some of which form the tear drops on the face of the outcrop nearest the rover. The outcrop is cross-cut with boxwork veins. Some of the veins have multiple, sometimes darker-toned, layers while others also have embedded dark-toned nodules. Observation point 3 of the Beinn an Dudhaich 2 target hit a resistant vein with an embedded dark-toned nodule with very high concentrations of $FeO_T$ (ChemCam prediction ~48.9 wt% $FeO_T$). These patches of dark-toned material are observed in other locations in veins (e.g., on Bearsden, Fig S16), and it is likely that all of these patches have high $FeO_T$ content. Ben Wyvis is a particularly interesting target as the CaO-rich nodule, or potentially CaO-rich cement points, have very weak P lines and intense CaF molecular emission, suggesting the features are due to apatite (Dehouck et al. 2022; Forni et al.,

2021). The two vein targets Bearsden (Fig S16) and Beinn Mohr (Fig S17) contain boron, and they are two of the few targets in Glen Torridon where B has been observed. The dark-toned layers within veins were not analyzed by ChemCam.

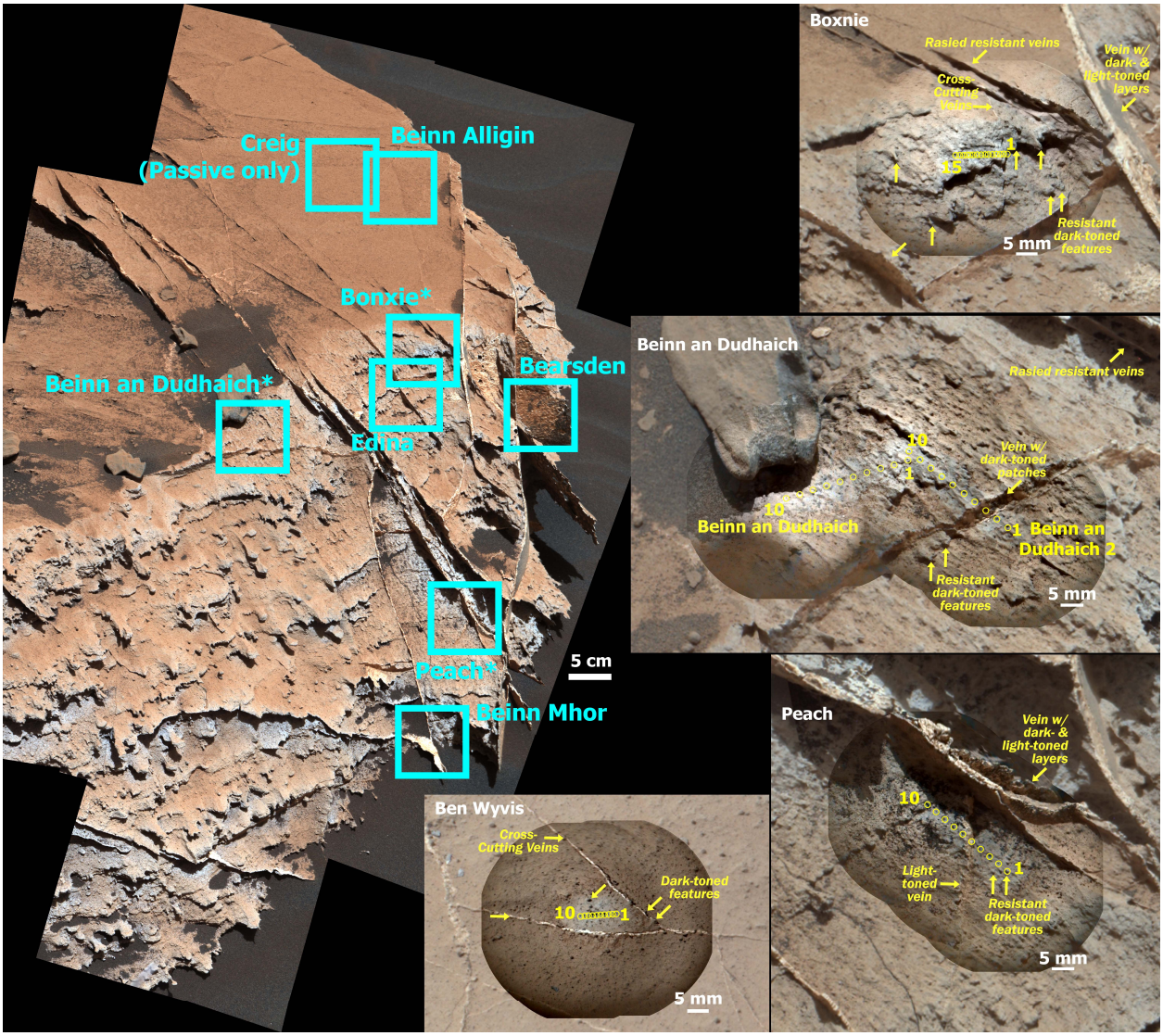


Figure 5: A Mastcam mosaic from sol 2734 showing the location of targets analyzed from sols 2735–2741. Locations of targets are outlines with boxes (ChemCam targets are cyan and MAHLI-only targets are white). Insets at right are annotated ChemCam targets overlain on their respective Mastcam images: Boxnie, Beinn an Dudhaich, Beinn an Dudhaich 2, Peach, and Ben Wyvis. The Ben Wyvis target is from a patch of bedrock to the right of the rover at this location and is not shown on the main Mastcam image. See Supplement Text S8 for a listing of Mastcam and MAHLI dataproducts in this Figure. Base image credit: NASA/JPL-Caltech/MSSS.

*3.6 Top of Western Butte, Tower Butte, and Hutton drill hole location*

In terms of bedrock chemistry and mineralogy, the Hutton location within the Glasgow member is best represented at the top of Western butte and the upper slopes of Tower butte, where the Hutton drill sample was collected (Fig S18). These locations have similar diagenetic features but

exhibit some key differences (Table 1-2, Hutton). The top of Western butte has a larger number of nodules with a significant chemical enrichment compared to the Hutton drill location. For example, on Western butte, Strathy Point is an MgO-rich cm-sized resistant nodule (Fig S19), and White Rashes has small embedded $FeO_T$-rich nodules surrounded by light-toned diagenetic halos (Fig S20). Despite the change in color, ChemCam did not observe significant enrichments in $SiO_2$ in White Rashes or in any other target along the traverse in Glen Torridon. The Hutton drill location typically has embedded small nodules (Fig S18) and some cm-sized resistant features (e.g., Troup Head, Fig S21), but when analyzed by ChemCam, these materials did not have significant chemical enrichments in any element compared to Hutton bedrock composition.

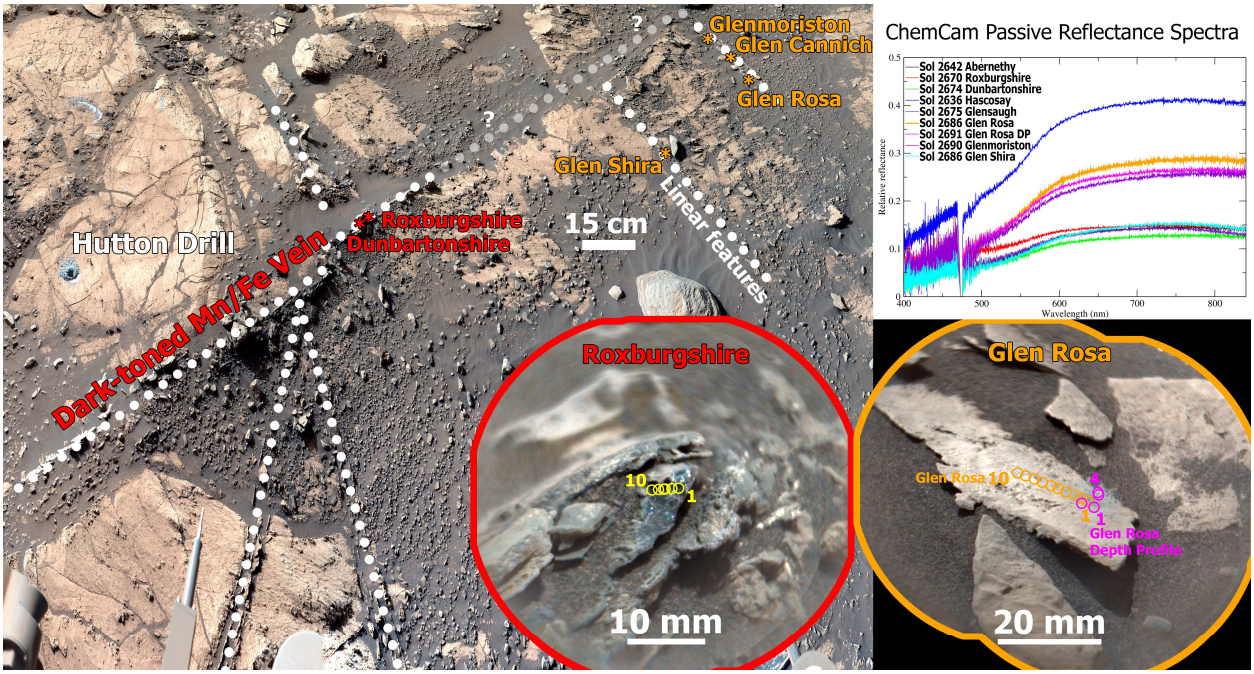


Figure 6: A Mastcam mosaic of the Hutton drill area from sol 2664. Only the dark-toned veins, linear features, and the Hutton drill hole from sols 2670–2691 are labeled for clarity. Vein or vein-like features are observed and outlined with white dotted lines. The dotted grey line labeled "?" may be where veins or fractures are hidden by sand cover. Passive reflectance spectra for features observed with ChemCam are shown in the top right (from this location and on Western butte). Bottom Insets are annotated ChemCam targets overlain on their respective Mastcam images: Roxburgshire, Glen Rosa, Glen Rosa DP (depth profile). See Supplement Text S8 for a listing of Mastcam and MAHLI dataproducts in this Figure. Base image credit: NASA/JPL-Caltech/MSSS.

The tops of Western and Tower buttes have chemically unique veins and vein-like linear features that have not been observed elsewhere in Gale crater (Table 3, veins and linear features). Both types are visible at the Hutton drill location (Figure 6, dotted white lines), and are observed within 1 m of each other at both Hutton and the top of Western butte. All these features' passive reflectance spectra are shown in the top right (from this location and on Western Butte). It is not clear whether the lighter-toned linear features and dark-toned veins intersect due to sand cover ("?" labeled dotted line in Figure 6, Mastcam top right corner).

The dark-toned veins at Hutton contain very high $FeO_T$ (ChemCam prediction ~47–55.5 wt% $FeO_T$), MnO (up to ~22 wt%; the highest amount of MnO in Gale crater detected by ChemCam), a very large missing component in the major oxide total, and they are relatively dark in albedo and spectrally flat/featureless (Figure 6; Table 3). A similar target analyzed at the top of Western butte, Abernethy (Fig S22), is a ~4 cm wide dark-toned vein with a similarly very high $FeO_T$ and MnO composition. All three of these dark-toned vein targets—Dunbartonshire, Roxburgshire, and Abernethy—have similar MgO and $Na_2O$ contents, and the spectra show Ni, Cl, and H peaks (Table 3). Lines for Ca, Na, Li, and K, are present in the spectra. The spectra show very weak lines for Si, Ti, Al, and thus $SiO_2$ is not listed in Table 3, as its composition predicted by our model is unreliable. The $FeO_T$ composition also exceeds our calibration model range for $FeO_T$, and this composition is unreliable. A calibration method developed for high $FeO_T$ by David et al. (2020) predicts ~25 wt% $FeO_T$ for these veins. Notably, no Cr was detected, although Cr is common in Gale crater sediments (Ollila et al., 2017) and is detected in nearly every type of nodular or nodule target (Table 1-3). Carbon lines are always present in the ChemCam spectra due to the martian atmosphere, and the C lines in these targets are relatively typical for Gale, so we cannot use them to determine the presence or absence of carbonate minerals. If we consider only the elements detected in the spectra, using the ChemCam prediction model (Clegg et al., 2017), these targets have oxide totals ~75 wt%, and using the David et al. (2020) model, the oxide total is ~45 wt%. These values suggest that there is likely at least one phase present that is not well represented in any current ChemCam model and/or a significant amount of an unidentified or unquantified element in these targets (e.g., Cl is present in some observation points, and H, Ni have relatively intense peaks compared to other Gale crater targets). Note that strong Fe lines can obscure weak S lines in the LIBS spectrum, so potentially S is present in these targets as well, but undetected in our spectra. Therefore, the chemical composition in the database and Table 3 (Gasda et al., 2022), which uses the Clegg et al. (2017) model, likely does not represent the true composition of the veins (uncertainties listed are likely underestimated). The passive reflectance spectra are featureless and suggest these dark-toned veins either do not contain significant ferric iron or contain gray hematite (Fraeman et al., 2020b); Mn oxides tend to be featureless in this range of passive reflectance spectroscopy (e.g., Fox et al., 2015; Lanza et al., 2016).

Two types of 'linear features' were identified that contain significant F: MgO/F linear features, and a unique CaO/F vein. Relative to other Mount Sharp group targets, MgO/F linear features contain typical amounts of $SiO_2$ and $Al_2O_3$, high MgO, ~2–3 wt% F (Forni et al., 2021), high $K_2O$, low $FeO_T$, and typical levels of Sr and hydration (Table 3). Trace elements detected were at much higher levels compared to other veins in Gale crater; these materials have some of the highest abundance of Li in any target found in Gale crater. The MgO/F linear features are lighter in albedo than FeO/MnO veins; the features are grayish beneath the dust as revealed by the laser cleaning, but also spectrally flat/featureless like the FeO/MnO veins. The unique Hascosay CaO/F vein target observed on Western butte (Fig S23) has the brightest albedo amongst these targets (Figure 6). Hascosay has a similar F (Forni et al., 2021) and $FeO_T$ composition as the MgO/F linear features near Hutton, but also contains relatively high CaO, S, relatively higher MnO, and lower MgO (Table 3). Hascosay hosts a nodule with ~3 wt% MnO with a weak Ba peak (~180 ppm). Hascosay is bordered to the right by a typical Ca-sulfate vein (sampled in the ChemCam target Northon). The bright albedo of Hascosay (Figure 6), is also consistent with the likely Ca-sulfate component in Hascosay.

Depth profiles may be useful to determine the phases present in the MgO/F and CaO/F targets. The Glen Rosa depth profile observation (Figure 6) consists of a 2x2 raster with 150 shots each. In observation point 3, CaO increases with depth, while the intensity of the CaF molecular emission signal, Li, and $K_2O$ all decrease. There is a strong positive correlation between Li, $K_2O$, and MgO in Glen Rosa along with a strong negative correlation between CaO and $K_2O$. This implies that F in Glen Rosa is likely related to the MgO, Li, and $K_2O$ rich phase (Forni et al., 2021). In other MgO/F linear features, which consist of the typical 30 shots per observation point, there is a correlation between the CaF molecular emission and CaO, and thus fluorite may be present in those targets (Forni et al., 2021). In the CaO/F Hascosay target point 6 (also a typical 30 shot observation), CaO increases along with the intensity of the CaF molecular emission signal, which may indicate fluorite (Forni et al., 2021). However, the Hascosay target has high S, and so likely most of the CaO is present as sulfate in this material, in addition to fluorite (Forni et al., 2021).

Dark-toned veins were imaged in the long distance RMI mosaic Haymarket on sol 2772 of the Tower butte pediment unconformity looking up from the Glasgow drill location (Fig S24). The dark-toned veins can be seen cross-cutting through the outcrop in Fig S24 and Fig S25 and the veins continue up to the unconformity, but then stop and do not appear to continue into the pediment (Fig S25, right inset). While on the pediment, veins were not observed (Bedford et al., 2022). The rover did not observe more dark-toned veins or linear features at other locations after driving away from Tower butte and while similar dark-toned features were observed on Vera Rubin ridge, they did not have a similar Mn chemistry (David et al., 2020).

*3.7 Mary Anning and Groken Drill location*

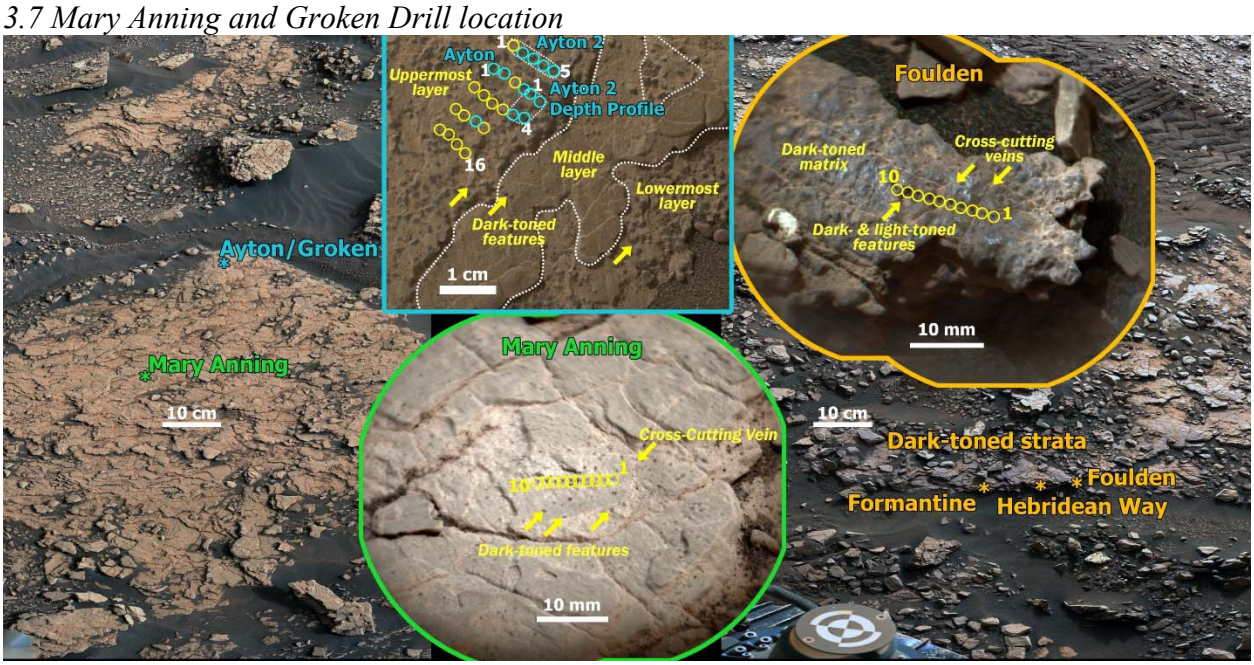


Figure 7: A Mastcam mosaic of the MA/GR drill area from sol 2829. Only the drill locations (Mastcam at left) and dark-toned strata (Mastcam at right) from sols 2831–2873 are labeled for clarity. Middle top inset: ChemCam targets Ayton, Ayton 2, and Ayton 2 DP (depth profile) are annotated on a MAHLI image. Cyan points in the Ayton rasters are where Mn-rich nodules were

hit. Other insets are annotated ChemCam targets overlain on their respective Mastcam images: Mary Anning and Foulden. See Supplement Text S8 for a listing of Mastcam and MAHLI dataproducts in this Figure. Base image credit: NASA/JPL-Caltech/MSSS

ChemCam discovered unusually elevated MnO abundances in the bedrock and in diagenetic materials, which is unique in Glen Torridon, at the Mary Anning and Groken drill location (Figure 1 Traverse 2; Figure 7; Table 1). This drill location is within the cross-stratified sandstone sediment in KHm (Figure 1). The Ayton targets, also where the Groken drill sample was collected, have angular nodules, 2–3 mm in size, that are confined to specific layers (labeled the 'uppermost' and 'lowermost' layers). These nodules are relatively rich in MnO (up to ~6 wt% amongst all nodules sampled at MA/GR) compared to the surrounding bedrock composition, and a majority of the nodules also had observable phosphorous peaks in the ChemCam spectra. Other than higher MnO and P, the nodules in the Ayton targets have a chemistry similar to the bedrock at this location, with a slight depletion in $SiO_2$ and other major elements, as expected, to account for the increase in MnO and P. In between the nodules in the nodule-rich layers, CaO and S were observed by ChemCam. These layers notably lack visible cross-cutting veins, indicating the possible presence of a Ca-sulfate cement in the rock between the nodules (Figs S56-S59). The wider Mastcam view of the Groken drill area shows that sulfate veins that may be parallel to bedding are present in other layers below the Ayton nodule-rich layers. Cross-cutting sulfate veins are also visible in the Mary Anning target. The "middle layer" also hosts dark-toned nodules (Figure 7), but these are <1 mm in size; these nodules are similar to those observed at the Mary Anning drill location and throughout the bedrock targets at this location (e.g., at a slightly higher elevation, the Breamish target, Fig S26). Although no nodules were analyzed with ChemCam within the Mary Anning target, the Mary Anning composition is representative of bedrock at this rover location and is relatively enriched in MnO and MgO compared to the rest of Glen Torridon (Table S1).

A few meters to the right of MA/GR, dark-toned strata are observed (Figure 7; Table 3). This material is $FeO_T$-rich relative to typical bedrock at this location, and MnO-poor, but contains MnO-rich nodules and cross-cutting calcium sulfate veins. The $FeO_T$-rich portions of the dark strata also contain elevated Cu (Goetz et al., 2022), but P was not detected. The specific morphology and chemistry of the dark-toned strata has not been previously observed in Gale crater. For this reason, we placed these targets into their own category. The dark-toned strata targets appear to be relatively erosionally-resistant layers of $FeO_T$-rich dark-toned nodules and a $FeO_T$-rich dark-toned cementing matrix that does not contain CaO or S.

*3.8 The Benches*

Above and southeast of the MA/GR drill sample location, the rover drove through a series of benches. Nodular bedrock was rare in this region. Generally, rare MnO-rich nodules were observed in the lower Benches within KHm, and $FeO_T$-rich nodules were observed in the upper Benches in the Glasgow member. For example, the Smugglers Cave (non-enriched nodular bedrock; Fig S27) and Breck (MnO nodule; Fig S28) nodules were observed approximately halfway through the Benches traverse. Smugglers Cave has 1-mm sized dark-toned embedded angular features with a patch of Ca-sulfate that roughly follows the bedding planes. Breck has similar dark-toned embedded (possibly slightly raised) ~1 mm sized nodules (Fig S28). It is unclear where the transition back to the Glasgow member occurred during this traverse, but

chemically there is a gradual transition in the MgO composition over the Benches traverses from KHm to Glasgow (Dehouck et al., 2022). Over this transition, the rover does not observe any major diagenetic features. However, the gaps in data over the part of the traverse from -4110 m – -4092 m elevation are due to the rover driving long distances, resulting in large changes in elevation between rover stops.

*3.9 Eastern Glasgow and the Polygonally Fractured Unit*

The polygonally fractured unit (PFU) was approached from the west on sol 2958, and the rover drove across this geomorphologic sub-unit on sols 2972–2999. The PFU is a portion of the Glasgow unit mapped from orbit as having a different surface texture from typical Glasgow (Hughes et al., 2020). The rover continued to drive along the edges of the PFU through sol 3007. $FeO_T$-rich nodules were observed only on the western approach to the PFU, and MnO-rich nodules were observed only on the PFU and the eastern edges until sol 3007. For example, the Ben Hee target has $FeO_T$-rich raised sub-angular 2–3 mm sized dark-toned nodules (Fig S29). Three examples of MnO-rich targets in the PFU were the Buness target, where darker, flat, interconnected/wormy, 1 mm sized, and slightly raised nodules were observed (Fig S30), and the St Andrews Square (Fig S31) and the St Vigeans (Fig S32) targets, where 1 mm sized, rounded, dark-toned, and embedded nodules were observed. Watch Stone is an example of a nodular target not on the PFU with rounded to sub angular 1–2 mm dark-toned embedded MnO-rich nodules (Fig S33). Halos that surround dark-toned features (with no major chemical enrichments) were observed in three targets (sols 2969–2972) as the rover approached the PFU and first drove onto the sub-unit. For example, the Windlestraw Law target was observed in the PFU and has 1 mm sized dark-toned embedded nodules with light-toned halos in a darker-toned bedrock (Fig S34). The Tomb of the Eagles target has dark-toned angular 1–2 mm sized embedded nodules and light-toned pits with dark-toned edges that appear to be depressions or voids in the MAHLI images (Fig S35).

*3.10 Overall Chemistry*

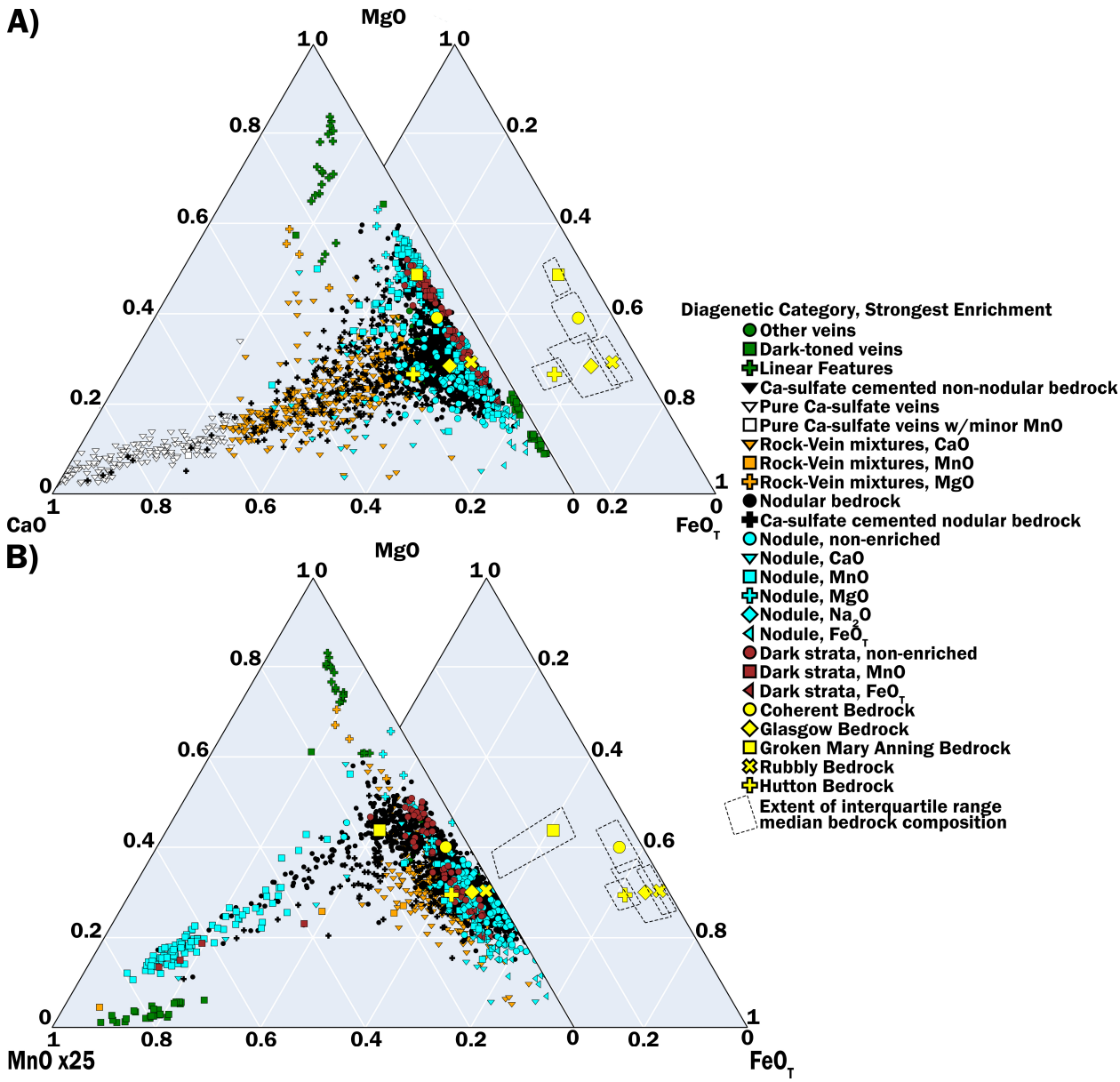


Figure 8: Two ternary diagrams that summarize the chemistry of the diagenetic features detected in Glen Torridon, with additional ternary diagrams in the Supplement Text S3 showing the diagenetic features in each chemical endmember plotted separately (Figs S36–S40) along with interactive versions of the ternary diagrams in the supplement. Figure 8A is the Mg-Fe-Ca molar oxide plot, and Figure 8B is the Mg-Fe-Mn molar oxide plot. Figure 8B increases the MnO wt% value by 25x before converting to molar oxide, for clarity. Both ternary diagrams plot the diagenetic features and the median composition of the bedrock chemical endmembers with the interquartile ranges of the bedrock compositions plotted just to the right of each diagram. Colors of symbols represent the type of nodule (see legend at right). Symbol shapes represent the strongest chemical enrichment of the diagenetic feature (see legend at right). Pure Ca-sulfate veins are not plotted on the Mg-Fe-Mn ternary plot.

Two ternary diagrams show chemical relationships between four chemical endmembers: MgO, $FeO_T$, MnO, and CaO (Figure 8). Figure 8A shows a strong $FeO_T$-MgO trend in the nodule (blue

symbols) compositions. The dark strata (dark red symbols) overlap this trend. While there is some overlap of the nodules with the nodular bedrock composition (black symbols), the nodule trend extends beyond the nodular bedrock composition. The spread of the nodule trend towards the CaO apex is due to Ca-sulfate mixing in the bedrock. Such mixing may be due to the presence of cements (black plus and upside-down triangle symbols), ChemCam points that simultaneously hit a vein and bedrock (mixed compositions are labeled with orange symbols), or ChemCam points that land mostly on a vein (white symbols). In addition, the $FeO_T$-rich nodules in Figure 8A and the $FeO_T$-MnO-rich dark-toned veins plot near each other, while the MgO-rich linear features plot nearer to the MgO apex than do the MgO-rich nodules. The $FeO_T$-rich dark-toned veins may fall off the MgO-$FeO_T$ trend due to issues predicting the composition of these features (See Section 3.6).

Figure 8B also illustrates the $FeO_T$-MgO trend in the nodules, but here replaces the CaO apex with MnO. In Figure 8B, the blue squares due to the MnO-rich nodules at the MA/GR drill sample location form a strong trend towards MnO. As stated in a previous section, the bedrock at this location has an overall higher MgO and MnO composition, shown by the position of the yellow square on Figure 8B, and the nodules extend away from this point. This shows that there is no correlation between MgO and $FeO_T$/MnO in these nodules. In addition, we see that the dark strata overlap the $FeO_T$-MgO trend on Figure 8B, and three MnO-rich nodules that were detected in these targets plot with the MnO-rich nodules near the Groken drill sample location. The dark strata have significantly lower MnO compared to other Groken area targets and follow a trend to higher $FeO_T$.

The same ternary diagrams are shown in Figs S36–S40 and described in Supplement Text S3, but each type of bedrock and its respective diagenetic features are split into separate ternary diagrams, so that one may directly compare diagenetic features and the local bedrock chemical endmember. In Figures S36–38 for coherent, rubbly, and Glasgow endmembers, the nodule-rich bedrock is clustered around their respective endmember bedrock compositions, with the exception of Figure S37 (rubbly), where the rubbly nodules may be slightly enriched in MnO compared to the bedrock. Figure S39 shows a clear $FeO_T$-MgO trend in the nodules and Hutton bedrock, which can be traced up to the MgO-rich linear features. In Figure S40, the dark strata are MnO-poor and $FeO_T$-rich compared to the local MA/GR bedrock and have a clear trend between MgO and $FeO_T$.

## 4. Discussion

During the traverse through Glen Torridon, the *Curiosity* rover observed a large variety of diagenetic features. Most of these features likely formed during early diagenesis, before lithifcation of the sediments, including likely cements and nodules. In some cases, there is evidence of cross cutting relationships where sulfate veins cut nodules or other sulfate features clearly show how diagenesis evolved with time in these sediments. Sulfate-rich features were observed mostly at the base of the buttes up to the pediment unconformity on the western side of Glen Torridon. The onset of nodular bedrock coincided with the transition into the Carolyn Shoemaker formation and cross-stratified sandstone intervals in the bedrock (Figure 1). Nodular bedrock was confined to specific locations that tend to be cross-stratified sandstone deposits within the KHm, notably at Harlaw, the MA/GR drill location, and at the KHm-Glasgow transition on the western side of the traverse (Figure 1). Nodular bedrock is mostly observed in

the Glasgow member both on and around the buttes (Figure 1 and 2). Both larger raised nodules and smaller embedded nodules were observed, and the chemistry ranges from $FeO_T$, MgO, or MnO-rich, or have no significant enrichment. There seems to be no relationship between the morphology of nodule, its size, its resistance to erosion, and its chemistry.

In the following sections, we attempt to tie together all the observations in Glen Torridon. We begin with the hypothesis that multiple chemical endmember fluids mixed at different times to produce the observations. We discuss the different important settings within Glen Torridon where these different endmembers dominated. For example, the sulfate rich endmember is a major component of Central and Western butte. The Mn-rich nodules and Fe-rich dark strata at Groken are examples of the redox processes occurring in Glen Torridon. The Hutton strata is where we observed enigmatic Fe, Mn, and Ni-rich dark-toned veins and Ca or Mg-rich linear features with high F. Following the discussion of the settings, we explore potential sources of fluids to account for different chemical endmembers in Glen Torridon, and importantly, whether F, or any other elements, are a clear signal of potential high-temperature hydrothermal alteration within the crater. We will also discuss how other elements associated with high F could be concentrated or would be affected by high-temperature hydrothermalism, if the higher temperatures are tied to post-impact processes in the crater, and the astrobiological implications of these scenarios.

### *4.1 Chemical Relationships*

There are strong chemical relationships between the nodules and nodular bedrock observed throughout Glen Torridon (Figure 8). This implies that many features could be related to the same diagenetic events. For example, the nodules and nodular bedrock in KHm and Glasgow form a strong trend, which is overlain with the dark strata trend. The linear features and the dark-toned veins may be following this trend as well, with the caveat that their chemistries predicted by the ChemCam model are less certain. The MnO-rich nodules form a different trend, but they could be related to the relatively higher concentrations of MnO in the dark-toned veins. Our hypothesis—to be addressed in detail in the following discussion sections—is that all diagenetic features observed in Glen Torridon are formed over multiple generations from the mixing of at least four chemical endmembers: MgO-rich, $FeO_T$-rich, MnO-rich, and Ca-sulfate rich. Fluorine, phosphorus, and copper-rich fluids that occur with MgO, FeO, and MnO, may have been brought in with these endmember compositions based on observations discussed herein.

### *4.2 Sulfate at the Buttes*

Central butte, and to some extent Western butte, have occurrences of Ca, Na, and Mg sulfate nodules, resistant strata, potential cements, and both veins that appear to follow bedding, as well as cross-cutting veins (as shown in Section 3.4, Figures 3 and 4; Figs S4–S9; Supplemental Text S8). The veins that follow bedding, including in the Sourhope target (Fig 4), may be primary deposition (early diagenesis) or later diagenetic formation of veins following the weaknesses between bedding planes. The potential cements range from some targets that have a lighter-toned matrix surrounding clasts of bedrock and dark-toned nodules (Black Gutter, Fig 4) to other targets that have light-toned grains mixed with typical reddish grains (Gleneagles, Fig 4).

The relationship between the sulfate-rich bedrock and the Ca, Mg, and Na sulfate materials at Central and Western buttes is reminiscent of many evaporitic settings on Earth. If the sulfates are

truly bedded, they would be similar to other marine evaporitic or perennial lake deposits, for example, within the Todilto Formation in New Mexico, the Permian basin in SE New Mexico, and Western Texas (e.g., Kirkland et al., 1995), and cores from Death Valley basins, where alternating layers of clay or limestone with primary evaporites occur (e.g., Lowenstein et al., 1999; Eugster and Hardie, 1978). Ca-sulfate nodules occur frequently in evaporitic settings, including the Todilto Fm (e.g., Kirkland et al., 1995).

However, the stratigraphic setting of Glen Torridon (i.e., that of a lake) does not seem to support a large scale evaporite deposit (Bennett et al., 2022; Thorpe et al., 2022; McAdam et al., 2022). Previous observations of increased sulfates (Rapin et al., 2019) and other soluble elements (B and Cl) (Gasda et al., 2017; Thomas et al., 2019; Achilles et al., 2020; Das et al., 2020) as well as changes to clay mineralogy (Bristow et al., 2018) in Hartmann's Valley through Sutton Island were previously interpreted as a drier interval in Gale crater. The resumption of finely layered lakebed sediments in Blunts Point was interpreted as a resumption of a wetter environment for deposition (Fedo et al., 2017; 2018; Gwizd et al., 2018; 2019; Edgar et al., 2020). Hence, it is not unusual for Gale to have experienced periodic drying of the lake, due to some climatic change, followed by resumption of wetter conditions in the crater. Likely, this interval of increased sulfates at the buttes is similar to these previous instances of increased aridity, but the proximity of these deposits to the overlying sulfate unit also may imply that these aridity intervals in martian history were becoming more frequent at the time that these sediments were deposited.

A sabkha setting is more consistent with the observations at the buttes and is our preferred interpretation. Sulfate and halite nodules and disseminated grains of sulfates and halite occur in these settings (e.g., West et al., 1979; Warren, 2016). In this scenario, on-shore sand dunes in an arid environment are situated next to a large body of saline water. Brines from the water table below the dunes move through the sand dunes via capillary action to deposit small grains of sulfate or halite in between sand grains through evaporation when this brine approaches the surface (e.g., West et al., 1979; Warren, 2016). Movement of water over long time periods cause some of the smaller grains to rework into sulfate nodules through repeated wetting and drying (e.g., West et al., 1979; Warren, 2016). Typically, the formation of the disseminated grains of sulfate and the sulfate nodules will displace the sand grains and layers (e.g., West et al., 1979; Warren, 2016). Due to the erosion of this ancient martian sandstone deposit (Figures 3 and 4), it is extremely difficult to determine if any displacement can be observed in the buttes. The Black Gutter target may be the best example of possible Ca sulfate bands and preservation of potential displacement around clasts of bedrock (Fig 4). Gleneagles and other potentially cemented targets display a light-toned matrix mixed with sand grains, and this material may be a cement, or grains of sulfate, which is similar in appearance to the sulfate grains that form between sand grains observed in lower sections of sabkhas (e.g., West et al., 1979). Within the same outcrop, the relatively large Ca-sulfate nodule observed at the Stonehive target (Fig 3) also appears to be consistent with the nodules observed in sabkhas (e.g., West et al., 1979; Shearman, 1981).

Another potential mechanism for sulfate nodule formation is late secondary diagenesis after burial from existing evaporite deposits (Warren, 2016). However, we do not favor this interpretation, because there are major differences between the observations made at Central and Western buttes, and those made in the environments on Earth where burial diagenesis alters existing sulfate deposits. The compaction and dewatering of clays and of gypsum to form

anhydrite causes a much wider-scale reworking of the sulfate deposits (Gindre-Chanu et al., 2015; Warren, 2016). This typically results in massive layers of sulfate nodules, usually as anhydrite (Warren, 2016). We have not observed these layers, and so burial diagenesis is inconsistent with the observations at the buttes. Burial diagenesis would likely destroy the fine-grained sulfates mixed within the sediments (e.g. Gleneagles, Figure 4). The dissolution of early sulfates and conversion of gypsum to anhydrite lead to collapse structures (e.g., Schreiber and El Tabakh, 2000; Gindre-Chanu et al., 2015). Neither the collapse structures nor the morphology of nodules is consistent with evaporite deposits that have been altered by burial diagenesis.

There were at least two episodes of sulfate formation with Ca, Na, and Mg in an early diagenetic pulse that formed the nodules and cements, and perhaps some of the veins that occur along bedding planes. This early diagenetic phase likely occurred while the lake was still present, if this location represents an ancient sabkha environment. Potentially a second or concurrent early generation of unknown composition (though likely related to the overlying Glasgow member nodules) overprinted the sulfates with dark-toned nodules. A third generation of Ca-sulfate events occurred later, after the bedrock had been lithified and fractured, producing the cross-cutting Ca-sulfate veins.

*4.3 Mary Anning and Groken MnO nodular bedrock*

The enrichment in MnO in the cross-stratified sandstone bedrock (Figure 1) of the MA/GR drill sample locations may be indicative of a Mn cement (see Section 3.7, Figure 7 and S40). The median MnO composition of MA/GR bedrock is 0.25 wt%, which is five times greater than typical bedrock in Glen Torridon, and two times greater than Hutton (Table S1). In addition, the median bedrock composition has 10 wt% MgO, which is the highest amount of MgO of any bedrock in Glen Torridon (Table S1). We observed $FeO_T$-rich dark-toned strata to one side of the MA/GR drill sample locations. The $FeO_T$-rich dark-toned strata are enriched in Cu compared to the surrounding area (Goetz et al., 2022). We also observed a spatial separation of Mn and Fe in the PFU nodular bedrock, where $FeO_T$-rich nodules only occur on the western side of the approach to the PFU, and MnO-rich nodules only occur on the PFU and the drive away from it. The chemical composition of the PFU and the Benches MnO-rich nodules may be related to those at MA/GR (see Supplement Text S3). Lastly, our analysis of P and Cu in the bedrock and nodules shows that P is frequently observed in nodules but not in the surrounding bedrock, whereas Cu is only detected in dark-toned strata, but not in the MnO nodules and bedrock (Goetz et al., 2022). Hence, the enrichment of Mg, Fe, Mn, Cu, and P suggests that either a single fluid chemically evolved over time or at least two fluids with these elements altered bedrock at this location, the Benches, and PFU. The strong spatial separation of Fe and Mn between Ayton and the dark strata, and in overlying strata along the second traverse (Figure 1), suggest redox played an important role in the deposition of these materials, in an early stage of the diagenetic process that produced nodules.

CheMin detected many of the typical minerals of Glen Torridon within both MA and GR drill samples, including plagioclase, calcium sulfates, pyroxenes, and phyllosilicates, as well as a mysterious 9.2 Å peak (Thorpe et al., 2022). This 9.2 Å peak was originally speculated to be either a rare form of Mn phosphate from the whiteite/jahnsite group, a talc-serpentine group mineral, or a Fe-rich oxide phase (Thorpe et al., 2022; Treiman et al., 2021). This phase is also observed at Kilmarie drill hole in the Jura member (Thorpe et al., 2022; Bristow et al., 2021),

where ChemCam did not observe significant MnO in the bedrock nor any nodules. Hence, the 9.2 Å peak is interpreted as a mixed layer phyllosilicate and modeled as either a talc-serpentine or even minnesotaite-greenalite phases by the CheMin team (Thorpe et al., 2022; Bristow et al., 2021). The whiteite/jahnsite and Fe-rich oxide phases were ruled out (Thorpe et al., 2022; Bristow et al., 2021). The layers that contain the Mn-rich dark-toned features are a few mm thick and just on the surface of the rock, so either a) the drill penetrated through these layers and sampled relatively nodule-free rock below the surface, b) the nodule's area on the surface do not represent a significant portion of the subsurface volume of material sampled by the drill, or c) the nodules were sampled by the drill, but the nodules are an amorphous or microcrystalline phase, which is consistent with the preliminary interpretations by the CheMin team (Thorpe et al., 2022).

Given the chemistry, mineralogy, and geologic context, we favor an interpretation of the nodules as amorphous concretions. On Earth, such concretions are observed to contain mostly crystalline silicates and a $FeO_T$ and MnO-rich amorphous fraction. Repeated wetting and drying resulting in redox cycling of sediments rich in Fe and Mn oxides near the surface (either subaqueously or subaerially, in deep sea or in shallow freshwater lakes) is one mechanism to produce concretions (e.g., Schwertmann and Fanning, 1976; Liu et al., 2002; Muller et al., 2002; Symanski et al., 2014; Hayles et al., 2021). The FeO and MnO cements in concretions are typically very poorly crystallized and difficult to characterize (Zhang and Karathanasis, 1997; Cornu et al., 2005). Concretions are typically larger fractions of cementing material (Fe and Mn oxides) compared to the typical bedrock material (phyllosilicates, volcaniclastics, and other phases) (Symanski et al., 2014). Some terrestrial studies have detected goethite, ferrihydrite, and lepidocrocite for the Fe phase, and manganite and todorikite for the Mn phase, among others (Schwertmann and Fanning, 1976; Zhang and Karathanasis, 1997; Liu et al., 2002; Cornu et al., 2005; Symanski et al., 2014). Commonly on Earth, concretions will form in discrete layers, and these layers are typically nearer to the surface where the fluid can interact with the relatively more oxidizing atmosphere (Schwertmann and Fanning, 1976; Muller et al., 2002; Cornu et al, 2005). This process is not necessarily related to the atmosphere on Mars as it is on Earth; it is merely that the location where redox reactions occur (i.e., the 'redox boundary') is over a thin horizon in the sediment, as postulated by Muller et al. (2002). This concept of mixing lacustrine and groundwater fluids beneath the lake is also suggested by Thorpe et al. (2022) as an avenue to explain the other mineralogical observations in Glen Torridon. If either of these fluids is sufficiently more oxidizing than the other fluid, then upon mixing, a redox boundary could form which would promote the formation of the cements and thin layers containing concretions at MA/GR.

The chemistry of the MA/GR nodules supports the hypothesis that these materials are amorphous concretions, and some Fe and Mn oxide concretions will accumulate phosphorous, where P typically correlates strongly with iron (Schwertmann and Fanning, 1976; Hawke et al., 1989; Yao and Millero, 1996; Muller et al., 2002) and Cu with manganese (Bradl, 2004; Goetz et al., 2022). However, it is puzzling that the opposite occurs here: there are no P detections in the Fe-rich dark strata, and there are no Cu detections in the Mn-rich Ayton targets, as detected by ChemCam (Goetz et al., 2022). The dark strata do host some Mn-rich nodules that correlate well with P detections. Phosphorus should more readily adsorb to Fe oxide than Mn oxide, while Cu should more readily adsorb to Mn oxide rather than Fe oxide (Hawke et al., 1989; Yao and Millero, 1996; Bradl, 2004). Either a redox or a pH reaction could have occurred to separate Fe

and Mn in solution due to differences in their redox potential and kinetics of oxide precipitation, such that a Fe- and Cu-rich but Mn- and P-poor fluid formed. Yao and Millero (1996) show that affinity for phosphate adsorption is greater in Fe-oxides as compared to Mn oxides in alkaline conditions. However, phosphate adsorption onto Fe oxide is still significant at acidic conditions (Yao and Millero, 1996), and thus acid-base reactions are unlikely to explain the observations we have at MA/GR. We hypothesize that this chemical separation is more likely related to an earlier redox separation which produced Fe-Cu-rich fluid and a different Mn-P-rich fluid. Once these fluids become separated, the stability of crystalline phosphate phases increase. Since CheMin did not detect any crystalline phosphates, the phase diagrams (See Supplement Text S6.1) suggest that fluids were more alkaline and slightly oxidizing to promote the formation of Fe and Mn oxides rather than phosphates. Mn oxides could have adsorbed some phosphate from solution (e.g., Yao and Millero, 1996). The presence of Cu can further constrain the formation conditions to near neutral (Goetz et al., 2022) because adsorption of Cu to sediments occurs most efficiently at pH 6–7 (Bradl, 2004). In summary, we suggest that at least two separate fluids interacted with bedrock at MA/GR to form the Mn- and P- rich nodules in the Ayton targets, and the Fe- and Cu-rich dark strata.

The unusual Fe-Mn-P-Cu chemistries observed in this location are also associated with Ca sulfate enrichment, as observed in the layers in the Ayton targets. These are different from veins observed elsewhere in Glen Torridon, because they contain a silicate portion, implying that the sulfate is more likely a cement. Unlike other sulfate layers observed at Central butte, the Ayton layer lacks other evaporitic materials, and the veins that follow the bedding at Central butte formed discrete and very thin layers of sulfate instead of a cement. We do not see veins following bedding at Ayton specifically, but their visibility may be due to the geometry or orientation of the layers at this location; the veins are easy to see in outcrop view in the buttes (Fig 4). The relative lack of fracture veins within these layers do imply that the Ayton nodule-rich layers remained relatively porous, or changed in porosity, and that the later-stage sulfates were able to fill these pores without forming fractures.

Depending on the timing and conditions of the addition of late-stage sulfate, freezing temperatures may have played a role in the addition of sulfate to these layers because salts that form in freezing conditions can increase the porosity of the bedrock based on a number of factors (Rossi-Manaresi and Tucci, 1991; Steiger, 2005a; 2005b; Rijniers, 2005). Frozen subsoil activities are known be limited to a few $cm^3$ (Harris et al., 2008) based on soil chemistry and pre-existing porosity, which may explain the limited nature of this activity near Groken. In addition, the Ayton concretions grew between layers of relatively more cemented bedrock, expanding these layers along this plane of weakness, which may have led to preferential fluid movement between these layers, rather than forming in nearby Mary Anning bedrock. Growth pressure in a large pore increases with decreasing size of the pore entrance (Steiger, 2005b; Rijniers et al., 2005). Stable frozen areas can lead to increased pore sizes (Wu et al., 2017). Increased pore pressure in frozen areas in a sediment also causes displacement of particles, resulting in increased porosity, creating space for water, salt transportation, and crystal growth (Wu et al., 2017). Aggregating water and salt in these positions may further change the pore structures (Wan et al., 2017; Lai et al., 2017). While this type of sulfate occurrence is not commonly observed in Gale crater, this is a plausible mechanism to explain the addition of sulfate surrounding the concretions at MA/GR.

*4.4 Carbonate Mineralization in Glen Torridon sediments*

A significant aspect of the Glen Torridon alteration mineralogy, which has not been identified in other rocks within Gale, is the presence of siderite carbonate. CheMin report siderite abundances between 0 and 2.2 % of whole rock in Glen Torridon, with positive detections in 5 drill holes (Rampe et al. 2020; Thorpe et al. 2022; Bristow et al., 2021). Kilmarie—a drill hole in the Jura member—has the highest abundance of the 12 Glen Torridon drill holes. These drill holes also have some of the highest clay content of any of the drill samples in Gale crater, pointing to higher degrees of aqueous alteration (Rampe et al. 2020; Thorpe et al. 2022; Bristow et al., 2021; Dehouck et al., 2022). Hence, if there is a link to the carbonate mineralization, it is masked because of the patchy alteration, as shown by variable carbonate abundances. Carbonate may well have been a relatively early diagenetic stage followed by variable dissolution and replacement by clays and oxides. However, constraining the paragenesis of this carbonate is challenging.

Instability is a notable feature of Fe-carbonate (siderite) occurrences under Earth-surface (oxidizing) conditions. It is readily oxidized and replaced by Fe oxides and hydroxides (Kholodov and Butuzova, 2008) by water hydrolysis reaction dominant at neutral to alkaline pH. The latter pH conditions are thought to be dominant in Gale sediments (e.g. Bridges et al. 2015). Thus, it is likely that the siderite abundances currently preserved and detected by the *Curiosity* rover are lower than the original abundances of carbonate. A hypothetical sequence could be envisioned, such that an early phase of diagenesis produces ferroan carbonate cements due to the effects of water-rock reactions between an atmospheric $CO_2$-charged groundwater and the Glen Torridon sediments (e.g., iron and manganese from mafic components combined with bicarbonate present due to carbonic acid species at elevated pH). Later stages of diagenesis associated with the main clay and oxide secondary mineral assemblages would have partially dissolved and replaced this carbonate leaving the current patchy distribution and abundance. The carbonate mineralization also offers a route for scavenging and concentrating Mn from surrounding Gale sediments and basement. $HCO_3^-$ ion can complex $Mn^{2+}$ at pH >6.3 (Mania et al., 1989) and is another indication that groundwater in Glen Torridon was neutral to alkaline, and reducing. Perhaps if the Mn was originally present as a minor or trace component in siderite, it could be released through later stages of diagenesis to produce mineral assemblages, such as those observed at MA/GR, or nodules in Glasgow.

*4.5 Hutton, Dark-Toned Veins, and Linear Features*

The mineralogy and chemistry of the Hutton strata, as well as the presence of Fe and Mn-rich dark-toned veins, and Mg and F rich linear features, make Hutton a unique location in Gale crater (See Section 3.6, Figure 6, Figure S39). The strata of Hutton are lighter-toned compared to the rest of Glen Torridon (Bennett et al., 2022; Bryk et al., 2020). The bedrock at Hutton is rich in cristobalite, opal CT, and magnetite (Thorpe et al., 2022). The chemistry of the bedrock is also different from the rest of Glen Torridon, as it has elevated CaO and $Na_2O$, and lower $SiO_2$ (Dehouck et al., 2022).

The relatively Fe- and Mn-rich dark-toned veins appear to contain a missing chemical component of ~25–55% (See Section 3.6). The veins are likely composed of phases that are relatively reduced (magnetite-rich) compared to typical hematite-rich Mount Sharp group

bedrock. That the nearby Hutton drill sample contains magnetite is evidence the fluids were likely reducing and do not contain gray hematite (See Supplement Text S6.2). This missing component likely includes Ni, Cl, and H (as water or OH groups) (See Section 3.6), all of which are challenging to quantify in ChemCam LIBS data. Typically, Fe and Mn rich veins form on Earth due to hydrothermal alteration of large ore bodies (Nadoll et al., 2014; Madondo et al; 2020; Burish et al; 2021), alteration of existing magnetite-rich igneous intrusions (Ovalle et al., 2018), or via hydrothermal alteration of pegmatite and ophiolites, associated with serpentinization (Gahlan et al., 2006; Hodel et al., 2017). However, each of these three options is difficult to explain in Gale crater. While there is no clear evidence of abundant serpentine within the crater, potential serpentine group minerals were observed in some Glen Torridon drill samples (Thorpe et al., 2022). It is possible that hydrothermal alteration related to the initial impact that formed Gale crater brought these materials into the crater via fractures, in which case serpentinite is not necessarily sourced from Glen Torridon bedrock (See section 4.7 and 4.8). If the Fe in the veins is in a magnetite phase—most consistent with the available evidence—then geochemical modeling suggests they formed in very alkaline and reducing fluids at temperatures >50C (See Supplement See Supplement Text S5.2). Under these conditions, magnetite overlaps with an amorphous Mn hydroxide phase, which would account for the very high Mn and H content of the veins. Although these veins contain no detectable chromium, making the dark-toned veins distinctly different from Cr-rich serpentinization products on Earth (e.g., Hodel et al., 2017), the chemistry of the Fe- and Mn-rich veins on the Earth that form in these systems is highly dependent on the original source rock composition (Nadoll et al., 2014).

The linear features and other F- and P-bearing materials have a very different chemistry compared to the dark-toned veins, but also have an extreme composition, and the linear features lie very close to the dark-toned veins (Fig 6, Fig S39). The linear features are F-rich, but no P is detected, which excludes apatite as a possibility (Forni et al., 2021). Some F- and P-bearing diagenetic material exists at slightly lower elevations in Glasgow, demonstrating that the F and P fluids did interact lower in the section, possibly forming apatite (Forni et al., 2021). One hypothesis is that the linear features are composed of mica, which can concentrate F, or potentially fluorite (Forni et al., 2021). Fluorine generally requires some hydrothermal alteration to become concentrated (Pirajno, 2018) and is generally not concentrated in the terrestrial surface or groundwaters (Worden, 2018). Some evaporitic settings can concentrate F in surface water due to evaporitic concentration, but these settings still have a magmatic/geothermal source component where the highest concentrations of F are found in water at depth and in the higher temperature fluids (e.g., Jones et al., 1977). Hence, the F-rich linear features, similar to the dark veins, may also be related to hydrothermal alteration that occurred after the initial impact, or from alteration of phosphates as suggested by Forni et al. (2015) and Nachon et al. (2017), rather than related to silicic magmatism within the crater (e.g., Sallet, 2000). If fluorapatite were the source of F and P in the fluids, temperatures would need to exceed 250C to destroy the apatite, depending on burial depths (e.g., Stofferregen and Alpers, 1987). The F-bearing fluid would also need to remain sufficiently warm to transport the F rich fluid until the F-rich phase precipitated from solution. Fluorite precipitation depends on variables including the presence and concentration of chloride salts in solution, pH, and pressure, and typically forms as the fluid cools at temperatures, starting below 250C, with a minimum solubility of fluorite at ~60C, and solubility increases slightly as temperature goes to 0C (Richardson and Holland, 1979). Similarly, diagenetic apatite tends to form at temperatures higher than 90C (e.g., Porten et al.,

2015). Acidic alteration may also dissolve apatite (e.g., Dorozhkin, 1997a; 1997b), but acidic alteration seems unlikely given the other observations at Hutton and Glen Torridon that suggest alteration fluids were mainly alkaline (Thorpe et al., 2022) (See Supplement Text S5.2). Therefore, we can estimate that the fluorite-rich linear features and nearby F and P rich materials in the Glasgow member likely formed at higher temperatures of at least 90C, which is consistent with the >50C formation temperature estimated for dark-toned veins in Hutton.

*4.6 The Relationship Between Hutton, Veins, and the Pediment Unconformity*

An examination of the relationship of Hutton and the pediment unconformity may shed light on whether Hutton is diagenetically altered (e.g., Dehouck et al., 2022), as well as the nature of the dark-toned veins and linear features. Hutton seems to be confined to the top layers near the unconformity on Tower butte, with some instances of similar bedrock at the top of Western butte. After the rover left Hutton, *Curiosity* drove east and uphill to an elevation that is higher than Hutton, and did not re-encounter this material, or any dark-toned veins, or any Mg-rich linear features. Hence, it seems that Hutton and the associated materials are spatially limited to this part of Glen Torridon.

While the rover observed the pediment unconformity at many locations along the pediment margins, many images of the Murray beneath the unconformity are difficult to interpret because they are either in shadow or covered in sand/scree material. Only in the mosaic in Fig S24 and S25 do we see an outcrop of Tower butte with no sand, less shadowing, and what we interpret as dark-toned veins cross-cutting the outcrop. On the right side of the mosaic, what appears to be a thick fracture-fill feature intersects the unconformity but does not travel into the pediment. This might be evidence for truncation of the vein at the unconformity.

Whether the dark-toned veins are truly truncated at the unconformity has major implications for timing of the veins and Hutton diagenesis, and by extension, the likely formation mechanism of the veins. If the veins are truncated, it implies that the veins are older than the erosional surface, and that these veins could have formed syndepositionally with Glasgow (i.e., as early as when the lake was active). This interpretation of a truncation of the veins is consistent with Bryk et al. (2020). Within Glen Torridon, we do not see clear evidence of fracturing of the sandstone above the Murray, where enrichments of S and $SiO_2$ were observed in light-toned features, as we did observe at Marias Pass (sols ~1000–1100) (e.g., Frydenvang et al., 2017; Czarnecki et al., 2020; Bedford et al., 2022). If the pediment sandstone was more porous (less lithified) at the time of fracturing in the Murray (or perhaps there could have been less overpressure to drive fracturing), fractures may not have formed during alteration of Siccar Point and Mount Sharp group rocks (Bedford et al., 2022). If that is the case, then the dark-toned veins may be relatively younger, similar to the cross-cutting sulfate veins. Although there is only one potential example of truncation, we favor a hypothesis where the veins are truncated at the unconformity. Future observations of the pediment unconformity could establish whether Hutton-like chemistry and mineralogy with dark-toned veins exists in other locales and could better constrain the relative timing of diagenetic features.

*4.7 Sources of Fluids*

Multiple sources of fluids and multiple mechanisms could have formed the Glasgow member nodules. These sources include locally derived fluids (fluids transporting elements over mm to m

scale), fluids derived from elsewhere in Glen Torridon or Gale (fluids transporting elements on the 10s of m to km scale laterally or vertically), and from outside the crater (transport on the 100s of km scale). We will also examine whether fluids were derived from burial diagenesis and hydrothermal alteration. For this, we keep in mind that Gale crater is a stable depression that is filled after its formation without additional subsidence, which sets it apart from some tectonically driven processes we are familiar with from Earth.

It is possible that the nodules in Glen Torridon were derived locally, i.e., via alteration, remobilization, and reworking of earlier sediments and cements. Weathering of basaltic materials can be highly inhomogeneous, and is dependent on the permeability of the material, which has – among other locations – been shown at Abert Lake in Canada, where volcanic ash layers were more prone to alteration than the less permeable rocks. In addition, alteration products were shown to be highly dependent on localized chemistry, forming different smectites within olivine or feldspar (Banfield et al., 1991). Similar localized alteration products have also been found in veins within martian meteorites (Changela and Bridges, 2011). Reworking could occur, for example, in cements rich in elements such as Mg, Fe, Mn, or within easily weathered phases containing these elements. Repeated wet and dry cycles could have reworked these components into concretions. However, it is not obvious from the nodular bedrock chemistry if these cements or phases existed in Glen Torridon other than at specific locations (the buttes and MA/GR). In many cases, we cannot detect with ChemCam any differences between the composition of the nodules, nodular bedrock, and typical bedrock composition (Figures 8 and S36–S40), with the exception of MnO in the rubbly bedrock.

The rubbly bedrock may have been altered by a slightly acidic fluid to derive groundwater rich in Mg, Mn, and Cu. It is suggested by Dehouck et al (2022) that the rubbly bedrock is more altered than the coherent bedrock. Moreover, the rubbly bedrock is depleted in Mn and Cu compared to the coherent bedrock (Goetz et al., 2022) (Table S1; Figure S37). The few nodules in the rubbly bedrock are enriched in MnO compared to the surrounding bedrock (Figure S37). Given that the rubbly bedrock is quite extensive in lower Glen Torridon (Dehouck et al., 2022; Goetz et al., 2022), it may be the source of Mn and Cu rich fluids if slightly acidic (pH ~5) or reducing alteration occurred, suggested by Goetz et al. (2022). However, the rubbly bedrock is not depleted in Fe compared to the rest of the crater; in fact, $FeO_T$ remains stable within ChemCam accuracy throughout the Murray formation bedrock, despite changes in mineralogy (e.g., Frydenvang et al., 2020; Dehouck et al., 2022). The only enrichments and depletions of $FeO_T$ in bedrock occur at small scales (e.g., L'Haridon et al., 2020; David et al., 2020). Hence, the source of Fe-rich fluids must be from elsewhere.

The Hutton bedrock may be another location that was altered by fluids, but that alteration is unlikely to have produced groundwaters rich in Mn and Fe that would subsequently form nodules in Glasgow and MA/GR. The chemical and mineralogical composition of Hutton is different (e.g., Dehouck et al., 2022; Thorpe et al., 2022), while the stratigraphy is largely unchanged (Bryk et al., 2020; Bennett et al., 2022), suggesting a diagenetic event altered this bedrock. It is possible this alteration is tied to the presence of the pediment or the pediment erosional surface (Dehouck et al., 2022). These hypothetical fluids then would have migrated downhill to the lower Glasgow member to deposit the nodules (e.g., to the location of Figure 5 nodules and veins) and deposit nodules at MA/GR (e.g., Tonui et al., 2003) in KHm sandstones

bounded by a clay-rich aquiclude (i.e., the Jura member) below. However, the Hutton bedrock has similar Fe contents as the other endmembers in Glen Torridon, and Mn is enriched in Hutton, so it unlikely that Hutton is the source rock for Fe and Mn-rich fluids.

While there are several lateral and small-scale options for fluid movement, another source of fluids could be large-scale upward movement from burial diagenesis. On Earth, burial diagenesis, compaction, and dewatering of much deeper layers occur at elevated (>60C) temperatures (Thorpe et al., 2022). The geothermal gradient of Earth is on average higher than that of Mars, favoring more intense burial heating and associated processes on Earth, but there could have been a locally enhanced geothermal gradient from remnant heat from the impact that made Gale crater. However, we do not observe widespread higher temperature phases in Glen Torridon (Thorpe et al., 2022); thus Thorpe et al. (2022) suggest that burial diagenesis at <80C may explain the mineralogical observations in GT. In addition, one hypothesis for how Vera Rubin ridge formed invokes warmer temperature fluids (e.g., Rampe et al., 2020). In addition to this hypothesis, thermochemical modelling has shown that diagenesis in the Murray formation, at and below Vera Rubin ridge, occurred at 50–100 °C with fluid pH range of 7.9–9.3 (Turner et al., 2021). However, the lower temperatures suggested by Thorpe et al. (2022) and Turner et al. (2021) may not be enough to account for elevated fluorine observed in Hutton and in some Glasgow nodules. In addition, burial diagenesis of the materials in Glen Torridon may be inconsistent with the observation of fine-scale sulfates in the sediments (see Section 4.2). Thus, while some features, such as the location within an impact crater, some observations at Glen Torridon, and generally the thickness of the sediment pile expected beneath the rover (Grotzinger et al. 2015) favor upwards movement of higher temperature fluids, many other observations point towards much lower temperatures and diagenetic processes that could be of more local nature.

The final source of fluids considered here would be from outside the crater. The sources of water could be from very deep aquifers migrating up through fractures either below the crater or from outside the crater (e.g., nearby volcanoes). The hypothesis that fluids from outside the crater have altered bedrock has been suggested for the origin of the Vera Rubin ridge by Fraeman et al. (2020a). It is less likely that regional Southern Highlands groundwater, connate fluids, or fluids from higher on Mt Sharp (meteorically derived) could be the main source of these reactions, as the temperatures of this ground water are likely not consistent with the higher temperatures suggested for Glen Torridon or Vera Rubin ridge (cf Fraeman et al., 2020a).

In summary, it is unlikely that all the fluids hypothesized came from the same source region. Rather, it is likely that multiple generations of fluids occurred (see Sections 4.2 and 4.3). While some deposits likely occurred at different times (e.g., dark strata and the Ayton nodules, Figure 5), in other cases, these fluids likely mixed to produce our observations (e.g., Fe and Mn-rich veins). Of these options, the fluids derived from rubbly bedrock may have been the source of Mn, Mg, and Cu rich fluids. We may be able to rule out Hutton alteration and burial diagenesis of local Glen Torridon bedrock as the source of Fe, Mn, Ni, F, P, and Li in fluids. For the latter, exhumation from greater depth would also be required, which is highly unlikely within an impact crater and in the absence of tectonic movements. For these elements, especially F, likely a higher temperature hydrothermal alteration event is required to concentrate them. If higher temperature fluids existed in Gale crater to produce the observed F, the question is how do those conditions

affect the elements associated with F (e.g., Mg, Ca), and what other observations could be explained with higher temperature fluids (e.g., Fe, Mn, and Ni rich veins).

*4.8 Mechanism for High-Temperature Hydrothermal Alteration in Gale Crater*

Gale crater is a large, complex impact crater, for which models predict a ~15 km high central uplift (potentially collapsed into a peak ring) and about 3600 $km^3$ of impact melt, half of which would have fallen back into the crater and created a melt sheet of up to 1 km thick in the crater moat (Schwenzer et al., 2012). Craters of that size, in water-bearing targets, have been shown to develop hydrothermal systems that can last tens of thousands of years (Abramov and King, 2005) or perhaps longer (Osinski et al., 2013), even if the surface temperature were below the freezing point (Barnhart et al., 2010; Ivanov and Pierazzo, 2011). The resulting hydrothermal alteration related to the initial impact has been proposed and described by many previous authors (Newsom, 1980; McCarville and Crossey, 1996; Newsom et al., 2001; 2010; Hagerty and Newsom, 2003; Osinski et al., 2005; 2013; Piranjo, 2009; Grieve et al., 2010; Schwenzer et al., 2012; 2016; Schwenzer and Kring, 2013; Turner et al., 2016; Franz et al., 2017; Kring et al., 2020; 2021; Ramkisson et al., 2021). The most recent study by Kring et al. (2020) describes a model for hydrothermal alteration where ground water gains access to hot basement rock beneath the terrestrial Chicxulub crater. In this model, the initial impact excavates ~km of material and creates deep fractures in the subsurface. The uplift of the peak ring of Chicxulub would bring hot basement rock to the surface. Then groundwater circulates to ~6 km depth in this model, with a radial distance of 10s of km, and observations of the borehole at the peak ring outer edge showed extensive veins and hydrothermal products (Kring et al., 2020). This may be analogous to Gale crater; although Gale is a smaller impact than Chicxulub, Gale has a central uplift, and this central uplift would have uplifted deeper and hotter basement rocks to the surface.

The general uplift of the basement floor, including the topographic uplift, is key to this model, because unlike the melt sheet, the target rocks take a longer time to cool to the ambient temperature at their new, much shallower elevation. The Kring et al., (2020) model and observations show that the Chicxulub peak ring cools at a slow rate, and likely subsurface temperatures within the peak ring remained >250C for at least 2 Myr after the impact. The long life of the alteration is consistent with other studies of post-impact hydrothermal activity (e.g., McCarville and Crossey, 1996; Williams et al., 2013). This is important for Gale crater because the impact exposes a large volume of deep crustal material to hot fluid alteration (estimate for Chicxulub is a ~$1x10^5$ $km^3$ of altered subsurface material (Kring et al., 2020)). Elements including P and F can be extracted from minerals including apatite and phlogopite, while Mg, Fe, and Mn can be extracted from olivine in basement ultramafic peridotite during this process (Schwenzer and Kring, 2013). Others have predicted that Gale would have had hot springs near the base of the central uplift and around the crater rim (e.g., Schwenzer et al., 2016). These vents would precipitate silica-rich materials (Newsom, 1980), and depending on water-rock ratios at the given location, produce alteration minerals, including smectites, serpentines, hematite, and silica (e.g., Schwenzer and Kring 2013; Osinski et al., 2013; Naumov, 2005). Phases hypothesized for the dark-toned vein and linear features observations in Glen Torridon—magnetite, manganese oxides, fluorite—have also been reported in the primary hydrothermal deposits related to terrestrial impact craters, including the Chicxulub and Houghton impact craters (Osiniski et al., 2005; 2013; Kring et al., 2020). The long period of alteration that occurs post-impact also suggests that the springs may have been active as the Gale lake initially formed,

because the activity in the central uplift would persist long after the melt sheet cooled, as suggested by the models of Abramov and Kring (2005), as well as observations at Chixculub (Kring et al., 2020) and a variety of other terrestrial impact craters (Osinksi et al. 2013).

The existence of an early extensive hydrothermal system in Gale would provide a powerful mechanism for transporting mobile elements within the basement in the rocks below the transient cavity, in the central uplift, and in the impact melt sheet, and potentially even into the earliest sediments deposited shortly after the melt sheet cooled and the lake formed. Indications of a high-temperature component, possibly recycled from such an early system, have been found in observations of the sulfur isotopes in Gale (Franz et al., 2017). Elements mobilized by high temperatures could have formed the observed nodules overprinting the lake sediments, followed by cements that lithified sediments, which then fractured, forming an early generation of veins. The observed diagenetic episodes may have involved multiple fluids with different origins, as well as water-rock reactions acting on selected parts of the stratigraphy in dependence of fracturing and permeability. In fact, most of the sedimentary sequence observed by the rover consists of lakebed sediments that show clear indication for diagenetic overprint by nodules (e.g., Sun et al., 2018; Meslin et al., 2018) and veins, including Mg-rich veins in Yellowknife Bay (Leveille et al., 2014) and Mn-rich veins in the Kimberley region (Lanza et al., 2016). These various diagenetic features observed throughout the traverse may be connected to the fluids we hypothesize for Glen Torridon, if the groundwater circulated in Gale crater on a broad scale. The locations of enrichments could be highly non-uniform (spatially and temporally) in pH and chemistry, due to variations in permeability, akin to what is observed in Yellowstone springs (Rowe et al., 1973; Gonsior et al., 2018). This early episode would not have been the end of fluid events in Gale that could have remobilized earlier formed deposits of mobile elements. Later generations of veins could have mobilized evaporites from later stages of the lake to form sulfate veins that cross cut nodular features.

*4.9 Implications*

The great diversity of diagenetic chemistry in Glen Torridon suggests multiple fluid generations interacted with the bedrock to produce the features observed. Our hypothesis is that elements such as F, Mn, Ni, and others were enriched very early, related to the initial impact. Hydrothermal alteration of the melt sheet was likely vigorous while the melt sheet cooled; later and relatively cooler hydrothermal alteration likely persisted in the deep subsurface and central uplift of the crater well after the melt sheet cooled and as the lake first formed. It is unknown if the hydrothermal alteration could persist well into the history of the lake and feed these elements from springs higher on Mt Sharp into the active lake, but the alteration of Hutton and chemically unique alteration veins may be evidence for persistent hydrothermal alteration in Gale crater. In addition, more study is needed to understand if there is a relationship between the ancient hydrothermal alteration of Hutton and the more recent truncation surface and subsequent deposition of Siccar Point. These dark-toned veins, if early, could have transported the high Fe and Mn fluids into upper Glen Torridon, producing nodules in Glasgow, and could be the source for the warmer, highly alkaline, and reducing fluid that altered Glen Torridon bedrock.

The diagenetic features, including cements, nodules, and some veins likely formed while the lake was present. Our favored hypothesis is that the buttes location represents a sabkha environment (sand dunes on a shore of a saline lake), which promoted the sulfates to form in the buttes. The

buttes and surrounding strata are all overprinted in dark-toned nodules as well, and perhaps as the lake floor level rose (i.e., after the time of the sabkha environment) nodules formed either beneath a shallow lake or even subaerially due to early diagenetic processes. Much later, lithification of the sediments occurred, likely at low temperatures as evidenced by the preservation of the fragile sulfate textures in the bedrock. Hydrofracturing of the lithified sediments then occurred, and fluids remobilized some of the sulfates into veins.

The chemical enrichments of the nodular bedrock are highly variable, both spatially and stratigraphically (Figures 1 and 2), suggesting multiple fluids events, in which fluids at times mixed (e.g., the presence of fluorite and apatite in Glasgow, Mn oxide concretions associated with P) or were separated by redox processes (strata hosting Fe oxides with no P with nodules of Mn oxides with P, and Fe oxides concretions spatially separated from Mn oxide concretions). Despite the high chemical variability, chemical trends suggest the enrichments are related to the same set of fluids (Figure 8).

Although Gale lake was perhaps relatively more saline at the time of sulfate deposition in the buttes, these features are not observed at higher stratigraphic levels in Glen Torridon. Hence, the presence of the sulfates near the buttes is likely only a brief interval of aridity in Gale crater followed by wetter conditions. Periods of briefly higher salinity have been suggested for lower portions of the Murray formation followed by wetter conditions at higher stratigraphic levels (e.g., Rapin et al., 2019; Das et al., 2020). As the *Curiosity* rover drives further up the flanks of Mt Sharp, we may observe more sulfate rich diagenesis and intervals of salinity (Rapin et al., 2021). The presence of the sulfates at this location in Glen Torridon, just below the transition into the sulfate unit, may represent the first of many episodes of dry conditions, potentially near the top of the Gale lacustrine bedrock sequence, eventually leading to drier conditions prevailing on the surface of Mars.

Hydrothermal alteration of the deep subsurface has important implications for habitability and prebiotic chemistry in Gale crater. Hydrothermal alteration after the initial impact and subsequent deep fluid circulation beneath the crater may have spurred serpentinization, which produces hydrogen gas and reducing fluids (Holm and Andersson, 1998; Sleep et al., 2004; Schulte et al., 2006). When the reducing fluids and gases interact with carbon monoxide and carbon dioxide on the surface of metal sulfides, native metals, or magnetite at vents, reactions occur to produce methane, Fischer Tropsch type reactions (Holm and Andersson, 1998), and may further react to produce the chemical building blocks of life (Huber and Wächtershäuser, 1998; Schulte et al., 2006; Martin and Russel, 2007). Furthermore, hydrothermal vents provide a source of energy for nascent microbial life, if any (Sleep et al., 2004; Schulte et al., 2006). Additionally, multiple stages of fluid alteration, mixing, redox reactions leading to element separation and precipitation, implies a habitable system persisted in the subsurface at the time of deposition of sediments in Glen Torridon (e.g., Cokell, 2014; Ramkisson et al., 2021). Although there is no evidence of life on Mars, many microbes facilitate redox reactions for S, Fe, and Mn oxides on Earth (Tebo et al., 2004; Macey et al., 2020). The presence of these materials and environments on Mars opens up new possibilities for habitability and prebiotic chemistry at Gale and likely beyond.

## 5. Conclusions

A wealth of observational data suggest that diagenesis has been a major process shaping the sediments in Glen Torridon. Some of these observations and the hypotheses put forth in this paper lack constraints on their formation conditions. For example, improvements to the major element oxide composition models and detection limits for transition metals in ChemCam spectra are needed to better understand the composition, and thus the formation conditions, of the veins. Additionally, modeling of Gale crater and post-impact hydrothermal activity in light of these new observations are needed to better constrain the source and formation conditions of the Fe, Mn, F, Mg, and Li in the dark veins and linear features. The role and timing of siderite mineralization is a unique aspect of the Glen Torridon sediments and suggests an early carbonate-rich secondary mineral assemblage derived from atmospheric $CO_2$-charged groundwaters. This assemblage was subsequently partially replaced during the dominant near-neutral diagenetic stages associated with clays and Fe oxides. Further observations by *Curiosity* of the pediment unconformity at different locations further upsection are needed to determine if Hutton strata are confined to a single location, if more Fe, Mn, or F-rich materials are again observed, and if these veins are truncated by the pediment erosional surface. These observations will help constrain the provenance of the dark-toned veins and relative timing of their formation.

Glen Torridon is one of the most chemically diverse locations in Gale crater in terms of diagenesis. There is a wide degree of spatial and stratigraphic variability in the chemistry and a large variety of morphological features are observed (rounded to angular, dark- and light-toned nodules, fracture-filling materials, cements). These chemical differences in the bedrock are likely indicative of widespread early diagenesis with multiple episodes of fluids, sometimes interacting or undergoing redox reactions. Some of the features may indicate a short episode of higher salinity in the lake, and these were then overprinted by diagenetic nodules that formed later in stratigraphic levels above the saline interval. Other observations point to the possibility of early enrichment via hydrothermal alteration. Much later, after burial and lithification of the bedrock, some remobilization occurred during subsequent alteration events that formed calcium sulfate veins. The diagenetic features in Glen Torridon, plus evidence of extensive alteration after the disappearance of the lake in Gale, points to a chemically diverse and long-lived surface and groundwater system in Gale crater.

**Acknowledgements**

The authors thank JPL for building and operating the *Curiosity* rover, as well as the NASA Mars Exploration Program and CNES for their support. The authors thank the Glen Torridon special issue authors for a great discussion of the results and especially Kristen Bennett, Alexander Bryk, William Dietrich, and Valerie Fox, for organizing the special issue. P. Gasda thanks Sean Czarnecki, Woodward Fischer, and Olivier Forni for their helpful discussions of the work and Scott VanBommel for helping prepare the supplemental database for archiving on the PDS. P. Gasda thanks Kristen Bennett, Travis Gabriel, and two anonymous reviewers for their helpful comments on the manuscript. J. Comellas thanks Valerie Payré for assistance with the lithium dataset. E. Dehouck, W. Rapin, P.-Y. Meslin, G. David, G. Caravaca, S. Le Mouélic, A. Cousin, S. Maurice, and O. Gasnault acknowledge funding from CNES (grant code 180027). S. Schwenzer acknowledges funding from UKSA (grant code ST/S001522/1), and Research England Expanding Excellence in England (E3) fund (grant code 124.18). J. Frydenvang acknowledges the support from the Carlsberg Foundation. The authors have no real or perceived financial or other conflicts of interest regarding the publication of this paper. Mastcam mosaics

were processed by the Mastcam team at Malin Space Science Systems. Any use of trade, firm, or product names is for descriptive purposes only and does not imply endorsement by the U.S. Government.

**Open Research**

All ChemCam spectra (Wiens, 2021a; 2021b), RMIs (Wiens, 2021c; 2021d), Mastcam images (Malin et al., 2021a; 2021b), and MAHLI images (Edgett et al., 2021a; 2021b) used in this work are available from the Planetary Data System (PDS) Geoscience Node (https://pds-geosciences.wustl.edu/missions/msl/chemcam.htm). A dataset with the ChemCam target level classification of the diagenetic features, observation level chemical data for each diagenetic feature, and local root mean squared error of the Li prediction, is also archived in Gasda et al. (2022) and available in the PDS geoscience node under Derived Products from Individual Investigators: https://pds-geosciences.wustl.edu/missions/msl/index.htm and in the ChemCam Archive: https://pds-geosciences.wustl.edu/missions/msl/chemcam.htm. These datasets are described in Supplement Text S1 and S7."

## References


Abramov, O., & Kring, D. A. (2005). Impact-induced hydrothermal activity on early Mars. *Journal of Geophysical Research*, *110*(E12), E12S09. https://doi.org/10.1029/2005JE002453

Achilles, C. N., Rampe, E. B., Downs, R. T., Bristow, T. F., Ming, D. W., Morris, R. V., et al. (2020). Evidence for Multiple Diagenetic Episodes in Ancient Fluvial-Lacustrine Sedimentary Rocks in Gale Crater, Mars. *Journal of Geophysical Research: Planets*, *125*(8). https://doi.org/10.1029/2019JE006295

Banfield, J. F., Jones, B. F., & Veblen, D. R. (1991). An aem-tem study of weathering and diagenesis, Abert Lake, Oregon: I. Weathering reactions in the volcanics. *Geochimica et Cosmochimica Acta*, *55*(10), 2781–2793. https://doi.org/10.1016/0016-7037(91)90444-A

Banham, S. G., Gupta, S., Rubin, D. M., Watkins, J. A., Sumner, D. Y., Edgett, K. S., et al. (2018). Ancient Martian aeolian processes and palaeomorphology reconstructed from the Stimson formation on the lower slope of Aeolis Mons, Gale crater, Mars. *Sedimentology*, *65*(4), 993–1042. https://doi.org/10.1111/sed.12469

Barnhart, C. J., Nimmo, F., & Travis, B. J. (2010). Martian post-impact hydrothermal systems incorporating freezing. *Icarus*, *208*(1), 101–117. https://doi.org/10.1016/j.icarus.2010.01.013

Bedford, C. C., Bridges, J. C., Schwenzer, S. P., Wiens, R. C., Rampe, E. B., Frydenvang, J., & Gasda, P. J. (2019). Alteration trends and geochemical source region characteristics preserved in the fluviolacustrine sedimentary record of Gale crater, Mars. *Geochimica et Cosmochimica Acta*, *246*, 234–266. https://doi.org/10.1016/j.gca.2018.11.031

Bedford, C. C., Schwenzer, S. P., Bridges, J. C., Banham, S., Wiens, R. C., Gasnault, O., et al. (2020). Geochemical variation in the Stimson formation of Gale crater: Provenance, mineral sorting, and a comparison with modern Martian dunes. *Icarus*, *341*, 113622. https://doi.org/10.1016/j.icarus.2020.113622

Bedford, C. C., et al., (2022) An insight into ancient aeolian processes and post-Noachian aqueous alteration in Gale crater, Mars, using ChemCam geochemical data from the Greenheugh capping unit. *Journal of Geophysical research: Planets* (GT Special Issue Paper), in review.

Bennett, K., et al., (2022) An Overview of the Curiosity rover's Campaign in Glen Torridon, Gale Crater, Mars, *Journal of Geophysical research: Planets* (GT Special Issue Paper), in review.

Bibring, J.-P., Langevin, Y., Mustard, J. F., Poulet, F., Arvidson, R., Gendrin, A., et al. (2006). Global Mineralogical and Aqueous Mars History Derived from OMEGA/Mars Express Data. Science, 312(5772), 400–404. https://doi.org/10.1126/science.1122659

Bradl, H. B. (2004). Adsorption of heavy metal ions on soils and soils constituents. *Journal of Colloid and Interface Science*, *277*(1), 1–18. https://doi.org/10.1016/j.jcis.2004.04.005

Bridges, J. C., Schwenzer, S. P., Leveille, R., Westall, F., Wiens, R. C., Mangold, N., et al. (2015). Diagenesis and clay mineral formation at Gale Crater, Mars. *Journal of Geophysical Research: Planets*, *120*(1), 1–19. https://doi.org/10.1002/2014JE004757

Bridges, J.C., Hicks, L.J. and Treiman, A.H. (2019) Carbonates on Mars. In: Volatiles in the Martian Crust (Filiberto, J. and Schwenzer, S.P. eds.). Elsevier. 89–118.

Bristow, T. F., Rampe, E. B., Achilles, C. N., Blake, D. F., Chipera, S. J., Craig, P., et al. (2018). Clay mineral diversity and abundance in sedimentary rocks of Gale crater, Mars. *Science Advances*, *4*(6), eaar3330. https://doi.org/10.1126/sciadv.aar3330

Bristow, T. F., Grotzinger, J. P., Rampe, E. B., Cuadros, J., Chipera, S. J., Downs, G. W., et al. (2021). Brine-driven destruction of clay minerals in Gale crater, Mars. *Science*, *373*(6551), 198–204. https://doi.org/10.1126/science.abg5449

Bryk, A. B., W. E. Dietrich, V. K. Fox, K. A. Bennett, S. G. Banham, M. P. Lamb, J. P. Grotzinger, A. R. Vasavada, K. M. Stack et al. (2020) The Stratigraphy of Central and Western Butte and the Greenheugh Pediment Contact, presented at the 51st Lunar and Planetary Conference, The Woodlands TX, Abstract 2612 https://www.hou.usra.edu/meetings/lpsc2020/pdf/2612.pdf

Burisch, M., Frenzel, M., Seibel, H., Gruber, A., Oelze, M., Pfänder, J. A., et al. (2021). Li-Co–Ni-Mn-(REE) veins of the Western Erzgebirge, Germany—a potential source of battery raw materials. *Mineralium Deposita*, *56*(6), 1223–1238. https://doi.org/10.1007/s00126-021-01061-4

Cabrol, N. A., Grin, E. A., Newsom, H. E., Landheim, R., & McKay, C. P. (1999). Hydrogeologic Evolution of Gale Crater and Its Relevance to the Exobiological Exploration of Mars. Icarus, 139(2), 235–245. https://doi.org/10.1006/icar.1999.6099

Calef III, F. J., & Parker, T. (2016). MSL Gale Merged Orthophoto Mosaic. PDS Annex, U.S. Geological Survey. http://bit.ly/MSL_Basemap

Caravaca, G., Le Mouélic, S., Rapin, W., Dromart, G., Gasnault, O., Fau, A., et al. (2021). Long-Distance 3D Reconstructions Using Photogrammetry with Curiosity's ChemCam Remote Micro-Imager in Gale Crater (Mars). *Remote Sensing*, *13*(20), 4068. https://doi.org/10.3390/rs13204068

Caravaca, G., et al., (2022), From lake to river: Documenting an environmental transition across the Jura/Knockfarril Hill members boundary in the Glen Torridon region of Gale crater (Mars). *Journal of Geophysical research: Planets* (GT Special Issue Paper), in review.

Changela, H. G., & Bridges, J. C. (2010). Alteration assemblages in the nakhlites: Variation with depth on Mars: Alteration assemblages in the nakhlites. *Meteoritics & Planetary Science*, *45*(12), 1847–1867. https://doi.org/10.1111/j.1945-5100.2010.01123.x

Clegg, S. M., Wiens, R. C., Anderson, R., Forni, O., Frydenvang, J., Lasue, J., et al. (2017). Recalibration of the Mars Science Laboratory ChemCam instrument with an expanded geochemical database. Spectrochimica Acta Part B: Atomic Spectroscopy, 129, 64–85. https://doi.org/10.1016/j.sab.2016.12.003

Clegg et al. (2020) Quantitative Sulfur Chemistry Observed on Diverse Samples from Sols 1800-2300. In the 51st Lunar and Planetary Science Conference, Abstract# 2561.

Cockell, C. S. (2014). Trajectories of Martian Habitability. *Astrobiology*, *14*(2), 182–203. https://doi.org/10.1089/ast.2013.1106

Comellas et al. (2021) Geologic Interpretations of Elevated-Mn ChemCam Targets in the Bradbury Rise, Gale Crater, Mars. In the 52th Lunar and Planetary Science Conference, Abstract #2176.

Cornu, S., Deschatrettes, V., Salvador-Blanes, S., Clozel, B., Hardy, M., Branchut, S., & Le Forestier, L. (2005). Trace element accumulation in Mn—Fe—oxide nodules of a planosolic horizon. *Geoderma*, *125*(1–2), 11–24. https://doi.org/10.1016/j.geoderma.2004.06.009

Czarnecki, S., Hardgrove, C., Gasda, P. J., Gabriel, T. S. J., Starr, M., Rice, M. S., et al. (2020). Identification and Description of a Silicic Volcaniclastic Layer in Gale Crater, Mars, Using Active Neutron Interrogation. *Journal of Geophysical Research: Planets*, *125*(3). https://doi.org/10.1029/2019JE006180

Das, D., Gasda, P. J., Wiens, R. C., Berlo, K., Leveille, R. J., Frydenvang, J., et al. (2020). Boron and Lithium in Calcium Sulfate Veins: Tracking Precipitation of Diagenetic Materials in Vera Rubin Ridge, Gale Crater. *Journal of Geophysical Research: Planets*, *125*(8). https://doi.org/10.1029/2019JE006301

David, G., Cousin, A., Forni, O., Meslin, P. -Y., Dehouck, E., Mangold, N., et al. (2020). Analyses of High-Iron Sedimentary Bedrock and Diagenetic Features Observed With ChemCam at Vera Rubin Ridge, Gale Crater, Mars: Calibration and Characterization. *Journal of Geophysical Research: Planets*, *125*(10). https://doi.org/10.1029/2019JE006314

Dehouck, E. et al., (2022), In situ geochemical characterization of the clay-bearing Glen Torridon region of Gale crater, Mars, using the ChemCam instrument, *Journal of Geophysical research: Planets* (GT Special Issue Paper), in review.

Dorozhkin, S. V. (1997a). Acdic dissolution mechanism of natural fluorapatite I. Milli-and microlevels of investigations. *Journal of Crystal Growth*, *182*, 125–132.

Dorozhkin, S. V. (1997b). Acidic dissolution mechanism of natural fluorapatite. II. Nanolevel of investigations. *Journal of Crystal Growth*, *182*(1–2), 133–140. https://doi.org/10.1016/S0022-0248(97)00331-X

Dromart, G., Le Deit, L., Rapin, W., Gasnault, O., Le Mouélic, S., Quantin-Nataf, C., et al. (2021). Deposition and erosion of a Light-Toned Yardang-forming unit of Mt Sharp, Gale crater, Mars. *Earth and Planetary Science Letters*, *554*, 116681. https://doi.org/10.1016/j.epsl.2020.116681

Edgar, L. A., Gupta, S., Rubin, D. M., Lewis, K. W., Kocurek, G. A., Anderson, R. B., et al. (2018). Shaler: *in situ* analysis of a fluvial sedimentary deposit on Mars. *Sedimentology*, *65*(1), 96–122. https://doi.org/10.1111/sed.12370

Edgar, L. A., Fedo, C. M., Gupta, S., Banham, S. G., Fraeman, A. A., Grotzinger, J. P., et al. (2020). A Lacustrine Paleoenvironment Recorded at Vera Rubin Ridge, Gale Crater: Overview of the Sedimentology and Stratigraphy Observed by the Mars Science Laboratory Curiosity Rover. *Journal of Geophysical Research: Planets*, *125*(3). https://doi.org/10.1029/2019JE006307

Edgett, K. S., & Malin, M. C. (2001). Rock stratigraphy in Gale crater, Mars. 32nd Lunar and Planetary Scince Conference, Abstract 1005.

Edgett, K. S., Yingst, R. A., Ravine, M. A., Caplinger, M. A., Maki, J. N., Ghaemi, F. T., et al. (2012). Curiosity's Mars Hand Lens Imager (MAHLI) Investigation. *Space Science Reviews*, *170*(1–4), 259–317. https://doi.org/10.1007/s11214-012-9910-4

Edgett, K. S., Caplinger, M. A., Maki, J. N., Ravine, M. A., F. Tony Ghaemi, McNair, S., et al. (2015). Curiosity's robotic arm-mounted Mars Hand Lens Imager (MAHLI): Characterization and calibration status. https://doi.org/10.13140/RG.2.1.3798.5447

Edgett, K.S. et al. (2017), Curiosity rover Mars Hand Lens Imager (MAHLI) views of the sediments and sedimentary rocks of Gale crater, Mars: Microscopy and Microanalysis, v. 23, p. 2142-2143, doi:10.1017/S1431927617011370.

Kenneth S. Edgett. (2021a). MSL MARS HAND LENS IMAGER 4 RDR IMAGE V1.0 [Data set]. NASA Planetary Data System. https://doi.org/10.17189/1520292

Kenneth S. Edgett. (2021b). MSL MARS HAND LENS IMAGER 4 RDR ZSTACK V1.0 [Data set]. NASA Planetary Data System. https://doi.org/10.17189/1520169

Ehlmann, B.L. and Edwards, C.S. (2014) Mineralogy of the Martian surface. An. Rev. Earth Planet. Sci. 42, 291-315.

Eugster, H. P., & Hardie, L. A. (1978). Saline Lakes. In A. Lerman (Ed.), Lakes: Chemistry, Geology, Physics (pp. 237–293). New York, NY: Springer New York. https://doi.org/10.1007/978-1-4757-1152-3_8

Fabre, C., Maurice, S., Cousin, A., Wiens, R. C., Forni, O., Sautter, V., & Guillaume, D. (2011). Onboard calibration igneous targets for the Mars Science Laboratory Curiosity rover and the Chemistry Camera laser induced breakdown spectroscopy instrument. *Spectrochimica Acta Part B: Atomic Spectroscopy*, *66*(3–4), 280–289. https://doi.org/10.1016/j.sab.2011.03.012

Fedo, C., et al. (2017). Facies Analysis and Basin Architecture of the Upper Part of the Murray Formation, Gale Crater, Mars. In the 48th Lunar and Planetary Science Conference, Abstract #1689.

Fedo, C., et al. (2018). Sedimentology and Stratigraphy of the Murray Formation, Gale Crater, Mars. In the 49th Lunar and Planetary Science Conference, Abstract #2078.

Forni, O., Gaft, M., Toplis, M. J., Clegg, S. M., Maurice, S., Wiens, R. C., et al. (2015). First detection of fluorine on Mars: Implications for Gale Crater's geochemistry. *Geophysical Research Letters*, *42*(4), 1020–1028. https://doi.org/10.1002/2014GL062742

Forni, O., Meslin, P.-Y., Drouet, C., Cousin, A., David, G. (2020) Apatites in Gale crater. Presented at the 51st Lunar and Planetary Science Conference, The Woodlands, TX, Abstract 2192.

Forni, O. Dehouck, E., Cousin, A., Bedford, C. C., David, G. (2021) Elevated Fluorine Abundances below the Siccar Point Unconformity: Implications for Fluid Circulation in Gale Crater, Presented at the 52nd Lunar and Planetary Science Conference, The Woodlands, TX, Abstract 1503.

Fox, V.K., Arvidson, R.E., Jolliff, B.L., Carpenter, P.K., Catalano, J.G., Hinkle, M.A.G., and Morris, R.V. (2015) Characterization of synthetic and natural manganese oxides as martian analogues, presented at the 46th Lunar and Planetary Science Conference, The Woodlands, TX, Abstract 2132.

Fraeman, A. A., Ehlmann, B. L., Arvidson, R. E., Edwards, C. S., Grotzinger, J. P., Milliken, R. E., et al. (2016). The stratigraphy and evolution of lower Mount Sharp from spectral, morphological, and thermophysical orbital data sets: Stratigraphy and Evolution of Mount Sharp. *Journal of Geophysical Research: Planets*, *121*(9), 1713–1736. https://doi.org/10.1002/2016JE005095

Fraeman, A. A., Edgar, L. A., Rampe, E. B., Thompson, L. M., Frydenvang, J., Fedo, C. M., et al. (2020a). Evidence for a Diagenetic Origin of Vera Rubin Ridge, Gale Crater, Mars: Summary and Synthesis of Curiosity 's Exploration Campaign. *Journal of Geophysical Research: Planets*, *125*(12). https://doi.org/10.1029/2020JE006527

Fraeman, A. A., Johnson, J. R., Arvidson, R. E., Rice, M. S., Wellington, D. F., Morris, R. V., et al. (2020b). Synergistic Ground and Orbital Observations of Iron Oxides on Mt. Sharp and Vera Rubin Ridge. *Journal of Geophysical Research: Planets*, *125*(9). https://doi.org/10.1029/2019JE006294

Franz, H. B., McAdam, A. C., Ming, D. W., Freissinet, C., Mahaffy, P. R., Eldridge, D. L., et al. (2017). Large sulfur isotope fractionations in Martian sediments at Gale crater. *Nature Geoscience*, *10*(9), 658–662. https://doi.org/10.1038/ngeo3002

Frydenvang, J., Gasda, P. J., Hurowitz, J. A., Grotzinger, J. P., Wiens, R. C., Newsom, H. E., et al. (2017). Diagenetic silica enrichment and late-stage groundwater activity in Gale crater, Mars: Silica enriching diagenesis, Gale, Mars. *Geophysical Research Letters*. https://doi.org/10.1002/2017GL073323

Frydenvang, J., Mangold, N., Wiens, R. C., Fraeman, A. A., Edgar, L. A., Fedo, C., et al. (2020). The chemostratigraphy of the Murray formation and role of diagenesis at Vera Rubin ridge in Gale crater, Mars, as observed by the ChemCam instrument. *Journal of Geophysical Research: Planets*. https://doi.org/10.1029/2019JE006320

Gahlan, H. A., Arai, S., Ahmed, A. H., Ishida, Y., Abdel-Aziz, Y. M., & Rahimi, A. (2006). Origin of magnetite veins in serpentinite from the Late Proterozoic Bou-Azzer ophiolite, Anti-Atlas, Morocco: An implication for mobility of iron during serpentinization. *Journal of African Earth Sciences*, *46*(4), 318–330. https://doi.org/10.1016/j.jafrearsci.2006.06.003

Gasda, P. J., Haldeman, E. B., Wiens, R. C., Rapin, W., Bristow, T. F., Bridges, J. C., et al. (2017). In situ detection of boron by ChemCam on Mars. *Geophysical Research Letters*, *44*(17), 8739–8748. https://doi.org/10.1002/2017GL074480

Gasda et al. (2019) High-Mn Sandstone as Evidence for Oxidized Conditions in Gale Crater Lake. In the 50th Lunar and Planetary Science Conference, Abstract# 1620.

Gasda, P. J., Anderson, R. B., Cousin, A., Forni, O., Clegg, S. M., Ollila, A., et al. (2021). Quantification of manganese for ChemCam Mars and laboratory spectra using a multivariate model. *Spectrochimica Acta Part B: Atomic Spectroscopy*, *181*, 106223. https://doi.org/10.1016/j.sab.2021.106223

Gasda, P. J., et al., (2022) Database of Diagenetic Features in the Clay-Rich Unit of Gale Crater, Mars [Data set]. NASA Planetary Data System. DOI: 10.17189/dw9v-xe39

Gindre-Chanu, L., Warren, J. K., Puigdefabregas, C., Sharp, I. R., Peacock, D. C. P., Swart, R., et al. (2015). Diagenetic evolution of Aptian evaporites in the Namibe Basin (south-west Angola). *Sedimentology*, *62*(1), 204–233. https://doi.org/10.1111/sed.12146

Goetz et al., (2022) Tracking of Copper by the ChemCam Instrument in Gale Crater, Mars: Elevated Abundances in Glen Torridon, *Journal of Geophysical research: Planets* (GT Special Issue Paper), in review.

Grotzinger, J. P., Crisp, J., Vasavada, A. R., Anderson, R. C., Baker, C. J., Barry, R., et al. (2012). Mars Science Laboratory Mission and Science Investigation. Space Science Reviews, 170(1–4), 5–56. https://doi.org/10.1007/s11214-012-9892-2

Grotzinger, J. P., Sumner, D. Y., Kah, L. C., Stack, K., Gupta, S., Edgar, L., et al. (2014). A Habitable Fluvio-Lacustrine Environment at Yellowknife Bay, Gale Crater, Mars. *Science*, *343*(6169), 1242777–1242777. https://doi.org/10.1126/science.1242777

Grotzinger, J. P., Gupta, S., Malin, M. C., Rubin, D. M., Schieber, J., Siebach, K., et al. (2015). Deposition, exhumation, and paleoclimate of an ancient lake deposit, Gale crater, Mars. *Science*, *350*(6257), aac7575–aac7575. https://doi.org/10.1126/science.aac7575

Gonsior, M., Hertkorn, N., Hinman, N., Dvorski, S. E.-M., Harir, M., Cooper, W. J., & Schmitt-Kopplin, P. (2018). Yellowstone Hot Springs are Organic Chemodiversity Hot Spots. *Scientific Reports*, *8*(1), 14155. https://doi.org/10.1038/s41598-018-32593-x

Grieve, R. A. F., Ames, D. E., Morgan, J. V., & Artemieva, N. (2010). The evolution of the Onaping Formation at the Sudbury impact structure: The evolution of the Onaping Formation. *Meteoritics & Planetary Science*, *45*(5), 759–782. https://doi.org/10.1111/j.1945-5100.2010.01057.x

Gwizd, S., Fedo, C., Grotzinger, J., Edgett, K., Rivera-Hernández, F., & Stein, N. (2018). Depositional History of the Hartmann's Valley Member, Murray Formation, Gale crater, Mars. In the 49th Lunar and Planetary Science Conference, Abstract #2150.

Gwizd, S., Fedo, C., Grotzinger, J., Edgett, K., Gupta, S., Stack, K. M., et al. (2019). Toward a greater understanding of cross-stratified facies in the Hartmann's Valley member of the

Murray formation, Gale crater, Mars. In the Ninth International Conference on Mars, Abstract #6183.

Hagerty, J. J., & Newsom, H. E. (2003). Hydrothermal alteration at the Lonar Lake impact structure, India: Implications for impact cratering on Mars. *Meteoritics & Planetary Science*, *38*(3), 365–381.

Harris, C., Kern-Luetschg, M., Smith, F., & Isaksen, K. (2008). Solifluction processes in an area of seasonal ground freezing, Dovrefjell, Norway: Solifluction Processes, Dovrefjell, Norway. *Permafrost and Periglacial Processes*, *19*(1), 31–47. https://doi.org/10.1002/ppp.609

Hawke, D., Carpenter, P. D., & Hunter, K. A. (1989). Competitive Adsorption of Phosphate on Goethite in Marine Electrolytes. *Environ. Sci. Technol.*, *23*, 187–191.

Hayles, S., Al, T., Cornett, J., Harrison, A., & Zhao, J. (2021). Growth rates for freshwater ferromanganese concretions indicate regional climate change in eastern Canada at the Northgrippian-Meghalayan boundary. *The Holocene*, *31*(8), 1250–1263. https://doi.org/10.1177/09596836211011652

Hodel, F., Macouin, M., Triantafyllou, A., Carlut, J., Berger, J., Rousse, S., et al. (2017). Unusual massive magnetite veins and highly altered Cr-spinels as relics of a Cl-rich acidic hydrothermal event in Neoproterozoic serpentinites (Bou Azzer ophiolite, Anti-Atlas, Morocco). *Precambrian Research*, *300*, 151–167. https://doi.org/10.1016/j.precamres.2017.08.005

Holm, N. G., & Andersson, E. M. (1998). Hydrothermal systems. In A. Brack (Ed.), The Molecular Origins of Life (1st ed., pp. 86–99). Cambridge University Press. https://doi.org/10.1017/CBO9780511626180.006

Horgan, B. H. N., Johnson, J. R., Fraeman, A. A., Rice, M. S., Seeger, C., Bell, J. F., et al. (2020). Diagenesis of Vera Rubin Ridge, Gale Crater, Mars, From Mastcam Multispectral Images. *Journal of Geophysical Research: Planets*, *125*(11). https://doi.org/10.1029/2019JE006322

Hurowitz, J. A. et al. (2017). Redox stratification of an ancient lake in Gale crater, Mars. *Science*, *356*(6341), eaah6849. https://doi.org/10.1126/science.aah6849

Huber, C., and Wächtershäuser, G. (1998). Peptides by Activation of Amino Acids with CO on (Ni,Fe)S Surfaces: Implications for the Origin of Life. *Science*, *281*(5377), 670–672. https://doi.org/10.1126/science.281.5377.670

Hughes, M. (2020). Geomorphic map of Glen Torridon in Gale crater, Mars [Data set]. Washington University in St. Louis. https://doi.org/10.7936/0CYW-3N10

Ivanov, B. A., & Pierazzo, E. (2011). Impact cratering in H2O-bearing targets on Mars: Thermal field under craters as starting conditions for hydrothermal activity: Thermal field under Martian impact craters. *Meteoritics & Planetary Science*, *46*(4), 601–619. https://doi.org/10.1111/j.1945-5100.2011.01177.x

Jones, B. F., Eugster, H. P., & Rettig, S. L. (1977). Hydrochemistry of the Lake Magadi basin, Kenya. *Geochimica et Cosmochimica Acta*, *41*(1), 53–72. https://doi.org/10.1016/0016-7037(77)90186-7

Kirkland, D. W., Denison, R. E., Evans, R. (1995) Middle Jurassic Todilto Formation of northern New Mexico and southwestern Colorado: marine or nonmarine? New Mexico Bureau of Geology and Mineral Resources Bulletin 147.

Kholodov, V.N. and Butuzova, G.Y. (2008) Siderite formation and evolution of sedimentary iron ore deposition in the Earth's history. Geo. Ore Dep. 50, 299–319.

Kring, D. A., Tikoo, S. M., Schmieder, M., Riller, U., Rebolledo-Vieyra, M., Simpson, S. L., et al. (2020). Probing the hydrothermal system of the Chicxulub impact crater. *Science Advances*, *6*(22), eaaz3053. https://doi.org/10.1126/sciadv.aaz3053

Kring, D. A., Whitehouse, M. J., & Schmieder, M. (2021). Microbial Sulfur Isotope Fractionation in the Chicxulub Hydrothermal System. *Astrobiology*, *21*(1), 103–114. https://doi.org/10.1089/ast.2020.2286

Kronyak, R. E., Kah, L. C., Edgett, K. S., VanBommel, S. J., Thompson, L. M., Wiens, R. C., et al. (2019). Mineral-Filled Fractures as Indicators of Multigenerational Fluid Flow in the Pahrump Hills Member of the Murray Formation, Gale Crater, Mars. *Earth and Space Science*, *6*(2), 238–265. https://doi.org/10.1029/2018EA000482

Lai, Y., Wu, D., & Zhang, M. (2017). Crystallization deformation of a saline soil during freezing and thawing processes. *Applied Thermal Engineering*, *120*, 463–473. https://doi.org/10.1016/j.applthermaleng.2017.04.011

Lanza, N. L., Wiens, R. C., Arvidson, R. E., Clark, B. C., Fischer, W. W., Gellert, R., et al. (2016). Oxidation of manganese in an ancient aquifer, Kimberley formation, Gale crater, Mars: Manganese Fracture Fills in Gale Crater. *Geophysical Research Letters*, *43*(14), 7398–7407. https://doi.org/10.1002/2016GL069109

Lasue, J., Clegg, S. M., Forni, O., Cousin, A., Wiens, R. C., Lanza, N., et al. (2016). Observation of > 5 wt % zinc at the Kimberley outcrop, Gale crater, Mars. *Journal of Geophysical Research: Planets*, *121*(3), 338–352. https://doi.org/10.1002/2015JE004946

Le Mouélic, S., Gasnault, O., Herkenhoff, K. E., Bridges, N. T., Langevin, Y., Mangold, N., et al. (2015). The ChemCam Remote Micro-Imager at Gale crater: Review of the first year of operations on Mars. *Icarus*, *249*, 93–107. https://doi.org/10.1016/j.icarus.2014.05.030

Léveillé, R. J., Bridges, J., Wiens, R. C., Mangold, N., Cousin, A., Lanza, N., et al. (2014). Chemistry of fracture-filling raised ridges in Yellowknife Bay, Gale Crater: Window into past aqueous activity and habitability on Mars: Chemistry of raised ridges, Gale Crater. *Journal of Geophysical Research: Planets*, *119*(11), 2398–2415. https://doi.org/10.1002/2014JE004620

L'Haridon, J., Mangold, N., Meslin, P.-Y., Johnson, J. R., Rapin, W., Forni, O., et al. (2018). Chemical variability in mineralized veins observed by ChemCam on the lower slopes of Mount Sharp in Gale crater, Mars. *Icarus*, *311*, 69–86. https://doi.org/10.1016/j.icarus.2018.01.028

L'Haridon, J., Mangold, N., Fraeman, A. A., Johnson, J. R., Cousin, A., Rapin, W., et al. (2020). Iron Mobility During Diagenesis at Vera Rubin Ridge, Gale Crater, Mars. *Journal of Geophysical Research: Planets*, *125*(11). https://doi.org/10.1029/2019JE006299

Liu, F., Colombo, C., Adamo, P., He, J. Z., & Violante, A. (2002). Trace Elements in Manganese-Iron Nodules from a Chinese Alfisol. *Soil Science Society of America Journal*, *66*(2), 661–670. https://doi.org/10.2136/sssaj2002.6610

Lowenstein, T. K., Li, J., Brown, C., Roberts, S. M., Ku, T.-L., Luo, S., & Yang, W. (1999). 200 k.y. paleoclimate record from Death Valley salt core. *Geology*, *27*(1), 3. https://doi.org/10.1130/0091-7613(1999)027<0003:KYPRFD>2.3.CO;2

Macey, M. C., Fox-Powell, M., Ramkissoon, N. K., Stephens, B. P., Barton, T., Schwenzer, S. P., et al. (2020). The identification of sulfide oxidation as a potential metabolism driving primary production on late Noachian Mars. *Scientific Reports*, *10*(1), 10941. https://doi.org/10.1038/s41598-020-67815-8

Madondo, J., Canet, C., González-Partida, E., Rodríguez-Díaz, A. A., Núñez-Useche, F., Alfonso, P., et al. (2020). Geochemical constraints on the genesis of the 'Montaña de Manganeso' vein-type Mn deposit, Mexican Plateau. *Ore Geology Reviews*, *125*, 103680. https://doi.org/10.1016/j.oregeorev.2020.103680

Malin, M. C., Ravine, M. A., Caplinger, M. A., Tony Ghaemi, F., Schaffner, J. A., Maki, J. N., et al. (2017). The Mars Science Laboratory (MSL) Mast cameras and Descent imager: Investigation and instrument descriptions: MSL Mastcam/MARDI Descriptions. *Earth and Space Science*, *4*(8), 506–539. https://doi.org/10.1002/2016EA000252

Michael C. Malin. (2021a). MSL MARS MAST CAMERA 4 RDR IMAGE V1.0 [Data set]. NASA Planetary Data System. https://doi.org/10.17189/1520328

Michael C. Malin. (2021b). MSL MARS MAST CAMERA 2 EDR IMAGE V1.0 [Data set]. NASA Planetary Data System. https://doi.org/10.17189/1520190

Mangold, N. et al., (2017), ChemCam analysis of aqueous processes on polygonal cracks at Gale Crater, Mars: 48th Lunar and Planetary Science Conference, The Woodlands, Texas, 19–23 March 2018, abs. 1908.

Mania, J., Chauve, P., Remy, F. and Verjus P. (1989) Evolution of Iron and Manganese Concentrations in Presence of Carbonates and Clays in the Alluvial Groundwaters of the Ognon (Franche-Comt, France) *Geoderma*, i, 219–227

Martin, W., & Russell, M. J. (2007). On the origin of biochemistry at an alkaline hydrothermal vent. *Philosophical Transactions of the Royal Society B: Biological Sciences*, *362*(1486), 1887–1926. https://doi.org/10.1098/rstb.2006.1881

Maurice, S., Wiens, R. C., Saccoccio, M., Barraclough, B., Gasnault, O., Forni, O., et al. (2012). The ChemCam Instrument Suite on the Mars Science Laboratory (MSL) Rover: Science Objectives and Mast Unit Description. *Space Science Reviews*, *170*(1–4), 95–166. https://doi.org/10.1007/s11214-012-9912-2

Maurice, S., Clegg, S. M., Wiens, R. C., Gasnault, O., Rapin, W., Forni, O., et al. (2016). ChemCam activities and discoveries during the nominal mission of the Mars Science Laboratory in Gale crater, Mars. *Journal of Analytical Atomic Spectrometry*, *31*(4), 863–889. https://doi.org/10.1039/C5JA00417A

McCarville, P., and Crossey, L. J., 1996, Post-impact hydrothermal alteration of the Manson impact structure, in Koeberl, C., and Anderson, R. R., eds., The Manson Impact Structure, Iowa: Anatomy of an Impact Crater: Boulder, Colorado, Geological Society of America Special Paper 302.

Meslin et al., (2017) Egg Rock Encounter: Analysis of an Iron-Nickel Meteorite Found in Gale Crater by Curiosity. In the 48th Lunar and Planetary Science Conference, Abstract# 2258.

Meslin et al. (2018) Detection of Hydrous Manganese and Iron Oxides with Variable Phosphorus and Magnesium Contents in the Lacustrine Sediments of the Murray Formation, Gale, Mars. In the 49th Lunar and Planetary Science Conference, Abstract #1447.

Meslin et al., (2019) Diversity and Areal Density of Iron-Nickel Meteorites Analyzed by ChemCam in Gale Crater. In the 50th Lunar and Planetary Science Conference, Abstract# 3179.

Milliken, R. E., Grotzinger, J. P., & Thomson, B. J. (2010). Paleoclimate of Mars as captured by the stratigraphic record in Gale Crater. *Geophysical Research Letters*, *37*(4). https://doi.org/10.1029/2009GL041870

Minitti, M. E., Malin, M. C., Van Beek, J. K., Caplinger, M., Maki, J. N., Ravine, M., et al. (2019). Distribution of primary and secondary features in the Pahrump Hills outcrop (Gale

crater, Mars) as seen in a Mars Descent Imager (MARDI) "sidewalk" mosaic. *Icarus*, *328*, 194–209. https://doi.org/10.1016/j.icarus.2019.03.005

Morris, R. V., Rampe, E. B., Vaniman, D. T., Christoffersen, R., Yen, A. S., Morrison, S. M., et al. (2020). Hydrothermal Precipitation of Sanidine (Adularia) Having Full Al,Si Structural Disorder and Specular Hematite at Maunakea Volcano (Hawai'i) and at Gale Crater (Mars). *Journal of Geophysical Research: Planets*, *125*(9). https://doi.org/10.1029/2019JE006324

Müller, B., Granina, L., Schaller, T., Ulrich, A., & Wehrli, B. (2002). P, As, Sb, Mo, and Other Elements in Sedimentary Fe/Mn Layers of Lake Baikal. *Environmental Science & Technology*, *36*(3), 411–420. https://doi.org/10.1021/es010940z

Nachon, M., Clegg, S. M., Mangold, N., Schröder, S., Kah, L. C., Dromart, G., et al. (2014). Calcium sulfate veins characterized by ChemCam/Curiosity at Gale crater, Mars. Journal of Geophysical Research: Planets, 119(9), 1991–2016. https://doi.org/10.1002/2013JE004588

Nachon, M., Mangold, N., Forni, O., Kah, L. C., Cousin, A., Wiens, R. C., et al. (2017). Chemistry of diagenetic features analyzed by ChemCam at Pahrump Hills, Gale crater, Mars. Icarus, 281, 121–136. https://doi.org/10.1016/j.icarus.2016.08.026

Nadoll, P., Angerer, T., Mauk, J. L., French, D., & Walshe, J. (2014). The chemistry of hydrothermal magnetite: A review. *Ore Geology Reviews*, *61*, 1–32. https://doi.org/10.1016/j.oregeorev.2013.12.013

Naumov, M. V. (2005). Principal features of impact-generated hydrothermal circulation systems: mineralogical and geochemical evidence. *Geofluids*, *5*(3), 165–184. https://doi.org/10.1111/j.1468-8123.2005.00092.x

Nellessen et al. (2019) Distribution and Analysis of Calcium Sulfate-Cemented Sandstones Along the MSL Traverse, Gale Crater, Mars. In the 50th Lunar and Planetary Science Conference, Abstract# 3031.

Newsom, H. (1980). Hydrothermal Alteration of Impact Melt Sheets with Implications for Mars. *Icarus*, *44*, 207–216.

Newsom, H. E., Hagerty, J. J., & Thorsos, I. E. (2001). Location and Sampling of Aqueous and Hydrothermal Deposits in Martian Impact Craters. Astrobiology, 1(1), 71–88.

Newsom, H. "Heated Lake on Mars" in Cabrol, N. A., & Grin, E. A. (Eds.). (2010). Lakes on Mars. Amsterdam Boston: Elsevier. Pp. 91-110.

Newsom et al. (2017) Increasing Occurrence of Sandstone Cemented with Calcium Sulfate on Mount Sharp, Gale Crater, Mars. In the 48th Lunar and Planetary Science Conference, Abstract# 2495

Ollila, A. M., Newsom, H. E., Clark, B., Wiens, R. C., Cousin, A., Blank, J. G., et al. (2014). Trace element geochemistry (Li, Ba, Sr, and Rb) using Curiosity 's ChemCam: Early results for Gale crater from Bradbury Landing Site to Rocknest. *Journal of Geophysical Research: Planets*, *119*(1), 255–285. https://doi.org/10.1002/2013JE004517

Ollila et al., (2017) Identification of Chromium in Rocks and Soils Using ChemCam's Laser Induced Breakdown Spectroscopy Instrument. In the 48th Lunar and Planetary Science Conference, Abstract# 2347.

Osinski, G. R., Lee, P., Parnell, J., Spray, J. G., & Baron, M. (2005). A case study of impact-induced hydrothermal activity: The Haughton impact structure, Devon Island, Canadian High Arctic. *Meteoritics & Planetary Science*, *40*(12), 1859–1877.

Osinski, G. R., Tornabene, L. L., Banerjee, N. R., Cockell, C. S., Flemming, R., Izawa, M. R. M., et al. (2013). Impact-generated hydrothermal systems on Earth and Mars. *Icarus*, *224*(2), 347–363. https://doi.org/10.1016/j.icarus.2012.08.030

Ovalle, J. T., La Cruz, N. L., Reich, M., Barra, F., Simon, A. C., Konecke, B. A., et al. (2018). Formation of massive iron deposits linked to explosive volcanic eruptions. *Scientific Reports*, *8*(1), 14855. https://doi.org/10.1038/s41598-018-33206-3

Pirajno, F. (2009). Hydrothermal Processes Associated with Meteorite Impacts. In F. Pirajno, Hydrothermal Processes and Mineral Systems (pp. 1097–1130). Dordrecht: Springer Netherlands. https://doi.org/10.1007/978-1-4020-8613-7_11

Pirajno, F. "Halogens in Hydrothermal Fluids and Their Role in the Formation and Evolution of Hydrothermal Mineral Systems" Harlov, D. E., & Aranovich, L. (Eds.). (2018). The Role of Halogens in Terrestrial and Extraterrestrial Geochemical Processes. Cham: Springer International Publishing. pp 759 https://doi.org/10.1007/978-3-319-61667-4

Payré, V., Fabre, C., Cousin, A., Sautter, V., Wiens, R. C., Forni, O., et al. (2017a). Alkali trace elements in Gale crater, Mars, with ChemCam: Calibration update and geological implications. J*ournal of Geophysical Research: Planets*, *122*(3), 650–679. https://doi.org/10.1002/2016JE005201

Payré, V., Fabre, C., Sautter, V., Cousin, A., Mangold, N., Deit, L. L., et al. (2019). Copper enrichments in the Kimberley formation in Gale crater, Mars: Evidence for a Cu deposit at the source. *Icarus*, *321*, 736–751. https://doi.org/10.1016/j.icarus.2018.12.015

Porten, K. W., Walderhaug, O., & Torkildsen, G. (2015). Apatite Overgrowth Cement As A Possible Diagenetic Temperature-History Indicator. *Journal of Sedimentary Research*, *85*(12), 1478–1491. https://doi.org/10.2110/jsr.2015.99

Ramkissoon, N. K., Turner, S. M. R., Macey, M. C., Schwenzer, S. P., Reed, M. H., Pearson, V. K., et al. (2021). Exploring the environments of Martian impact-generated hydrothermal systems and their potential to support life. *Meteoritics & Planetary Science*, *56*(7), 1350–1368. https://doi.org/10.1111/maps.13697

Rampe, E. B., Bristow, T. F., Morris, R. V., Morrison, S. M., Achilles, C. N., Ming, D. W., et al. (2020). Mineralogy of Vera Rubin Ridge from the Mars Science Laboratory CheMin Instrument. *Journal of Geophysical Research: Planets*. https://doi.org/10.1029/2019JE006306

Rapin, W., Meslin, P.-Y., Maurice, S., Vaniman, D., Nachon, M., Mangold, N., et al. (2016). Hydration state of calcium sulfates in Gale crater, Mars: Identification of bassanite veins. *Earth and Planetary Science Letters*, *452*, 197–205. https://doi.org/10.1016/j.epsl.2016.07.045

Rapin, W., Meslin, P.-Y., Maurice, S., Wiens, R. C., Laporte, D., Chauviré, B., et al. (2017). Quantification of water content by laser induced breakdown spectroscopy on Mars. *Spectrochimica Acta Part B: Atomic Spectroscopy*, *130*, 82–100. https://doi.org/10.1016/j.sab.2017.02.007

Rapin, W., Ehlmann, B. L., Dromart, G., Schieber, J., Thomas, N. H., Fischer, W. W., et al. (2019). An interval of high salinity in ancient Gale crater lake on Mars. *Nature Geoscience*, *12*(11), 889–895. https://doi.org/10.1038/s41561-019-0458-8

Rapin, W., Dromart, G., Rubin, D., Le Deit, L. Le Mouélic, S., Gasnault, O. et al., (2021) First Insights on Depositional Environments Recorded in The "Clay-Sulfate" Transition at Gale Crater, presented at the 52nd Lunar and planetary Science Conference, The Woodlands, TX, Abstract 1479.

Richardson, C. K., & Holland, H. D. (1979). Fluorite deposition in hydrothermal systems. *Geochimica et Cosmochimica Acta*, *43*(8), 1327–1335. https://doi.org/10.1016/0016-7037(79)90122-4

Rijniers, L. A., Huinink, H. P., Pel, L., & Kopinga, K. (2005). Experimental Evidence of Crystallization Pressure inside Porous Media. *Physical Review Letters*, *94*(7), 075503. https://doi.org/10.1103/PhysRevLett.94.075503

Rivera-Hernández, F., Sumner, D. Y., Mangold, N., Stack, K. M., Forni, O., Newsom, H., et al. (2019). Using ChemCam LIBS data to constrain grain size in rocks on Mars: Proof of concept and application to rocks at Yellowknife Bay and Pahrump Hills, Gale crater. *Icarus*, *321*, 82–98. https://doi.org/10.1016/j.icarus.2018.10.023

Rivera-Hernández, F., Sumner, D. Y., Mangold, N., Banham, S. G., Edgett, K. S., Fedo, C. M., et al. (2020). Grain Size Variations in the Murray Formation: Stratigraphic Evidence for Changing Depositional Environments in Gale Crater, Mars. *Journal of Geophysical Research: Planets*, *125*(2). https://doi.org/10.1029/2019JE006230

Rossi-Manaresi, R., & Tucci, A. (1991). Pore Structure and the Disruptive or Cementing Effect of Salt Crystallization in Various Types of Stone. *Studies in Conservation*, *36*(1), 53. https://doi.org/10.2307/1506452

Rowe, J. J., Fournier, R. O., Morey, G. W. (1973) Chemical Analysis of Thermal Waters in Yellowstone National Park, Wyoming, 1960-65. Geological Survey Bulletin 1303, US Department of the Interior

Sallet, R. (2000). Fluorine as a tool in the petrogenesis of quartz-bearing magmatic associations: applications of an improved F–OH biotite–apatite thermometer grid. *Lithos*, *50*(1–3), 241–253. https://doi.org/10.1016/S0024-4937(99)00036-5

Schröder, S., Meslin, P.-Y., Gasnault, O., Maurice, S., Cousin, A., Wiens, R. C., et al. (2015). Hydrogen detection with ChemCam at Gale crater. *Icarus*, *249*, 43–61. https://doi.org/10.1016/j.icarus.2014.08.029

Schreiber, B. C., & Tabakh, M. E. (2000). Deposition and early alteration of evaporites: Primary evaporites and their meaning. *Sedimentology*, *47*, 215–238. https://doi.org/10.1046/j.1365-3091.2000.00002.x

Schulte, M., Blake, D., Hoehler, T., & McCollom, T. (2006). Serpentinization and Its Implications for Life on the Early Earth and Mars. *Astrobiology*, *6*(2), 364–376.

Schwenzer, S. P., Abramov, O., Allen, C. C., Bridges, J. C., Clifford, S. M., Filiberto, J., et al. (2012). Gale Crater: Formation and post-impact hydrous environments. *Planetary and Space Science*, *70*(1), 84–95. https://doi.org/10.1016/j.pss.2012.05.014

Schwenzer, S. P., & Kring, D. A. (2013). Alteration minerals in impact-generated hydrothermal systems – Exploring host rock variability. *Icarus*, *226*(1), 487–496. https://doi.org/10.1016/j.icarus.2013.06.003

Schwenzer, S. P., Bridges, J. C., Wiens, R. C., Conrad, P. G., Kelley, S. P., Leveille, R., et al. (2016). Fluids during diagenesis and sulfate vein formation in sediments at Gale crater, Mars. Meteoritics & Planetary Science, 51(11), 2175–2202. https://doi.org/10.1111/maps.12668

Schwertmann, U., & Fanning, D. S. (1976). Iron-manganese Concretions in Hydrosequences of Soils in Loess in Bavaria. *Soil Science Society of America Journal*, *40*, 731–738.

Siebach, K. L., Grotzinger, J. P., Kah, L. C., Stack, K. M., Malin, M., Léveillé, R., & Sumner, D. Y. (2014). Subaqueous shrinkage cracks in the Sheepbed mudstone: Implications for early fluid diagenesis, Gale crater, Mars. *Journal of Geophysical Research: Planets*, *119*(7), 1597–1613. https://doi.org/10.1002/2014JE004623

Sleep, N. H., Meibom, A., Fridriksson, Th., Coleman, R. G., & Bird, D. K. (2004). H2-rich fluids from serpentinization: Geochemical and biotic implications. *Proceedings of the National Academy of Sciences*, *101*(35), 12818–12823. https://doi.org/10.1073/pnas.0405289101

Smith et al. (2021) X-Ray Amorphous Sulfates in Gale Crater. In the 52nd Lunar and Planetary Science Conference, Abstract# 1486.

Stack, K. M., Grotzinger, J. P., Lamb, M. P., Gupta, S., Rubin, D. M., Kah, L. C., et al. (2019). Evidence for plunging river plume deposits in the Pahrump Hills member of the Murray formation, Gale crater, Mars. *Sedimentology*, *66*(5), 1768–1802. https://doi.org/10.1111/sed.12558

Stack, K. M. et al., (2022), Orbital and In-Situ Investigation of Periodic Bedrock Ridges in Glen Torridon, Gale Crater, Mars *Journal of Geophysical research: Planets* (GT Special Issue Paper), in review.

Steiger, M. (2005a). Crystal growth in porous materials—I: The crystallization pressure of large crystals. *Journal of Crystal Growth*, *282*(3–4), 455–469. https://doi.org/10.1016/j.jcrysgro.2005.05.007

Steiger, M. (2005b). Crystal growth in porous materials—II: Influence of crystal size on the crystallization pressure. *Journal of Crystal Growth*, *282*(3–4), 470–481. https://doi.org/10.1016/j.jcrysgro.2005.05.008

Stein, N., Grotzinger, J. P., Schieber, J., Mangold, N., Hallet, B., Newsom, H., et al. (2018). Desiccation cracks provide evidence of lake drying on Mars, Sutton Island member, Murray formation, Gale Crater. *Geology*, *46*(6), 515–518. https://doi.org/10.1130/G40005.1

Stoffregen, R. E., & Alpers, C. N. (1987). Woodhouseite and Svanbergite in Hydrothermal Ore Deposits: Products of Apatite Destruction During Advanced Argillig Alteration. *The Canadian Mineralogist*, *25*(2), 201–211.

Sun, V. Z., Stack, K. M., Kah, L. C., Thompson, L., Fischer, W., Williams, A. J., et al. (2019). Late-stage diagenetic concretions in the Murray formation, Gale crater, Mars. *Icarus*, *321*, 866–890. https://doi.org/10.1016/j.icarus.2018.12.030

B. Sutter, A. C. McAdam, P. R. Mahaffy, D. W. Ming, K. S. Edgett, E. B. Rampe, J. L. Eigenbrode, H. B. Franz, C. Freissinet, J. P. Grotzinger, A. Steele, C. H. House, P. D. Archer, C. A. Malespin, R. Navarro-González, J. C. Stern, J. F. Bell, F. J. Calef, R. Gellert, D. P. Glavin, L. M. Thompson, A. S. Yen, (2017) Evolved gas analyses of sedimentary rocks and eolian sediment in Gale Crater, Mars: Results of the Curiosity rover's sample analysis at Mars instrument from Yellowknife Bay to the Namib Dune, *Journal of Geophysical Research: Planets*, *122*, 2574–2609 https://doi.org/10.1002/2016JE005225

Szymański, W., Skiba, M., & Błachowski, A. (2014). Mineralogy of Fe–Mn nodules in Albeluvisols in the Carpathian Foothills, Poland. *Geoderma*, *217–218*, 102–110. https://doi.org/10.1016/j.geoderma.2013.11.008.

Shearman, D. J. (1981). Displacement of sand grains in sandy gypsum crystals. *Geological Magazine*, *118*(3), 303–306. https://doi.org/10.1017/S0016756800035792

Tebo, B. M., Bargar, J. R., Clement, B. G., Dick, G. J., Murray, K. J., Parker, D., et al. (2004). Biogenic Manganese Oxides: Properties and Mechanisms of Formation. *Annual Review of Earth and Planetary Sciences*, *32*(1), 287–328. https://doi.org/10.1146/annurev.earth.32.101802.120213

Thomas, N. H., Ehlmann, B. L., Meslin, P. -Y., Rapin, W., Anderson, D. E., Rivera-Hernández, F., et al. (2019). Mars Science Laboratory Observations of Chloride Salts in Gale Crater, Mars. *Geophysical Research Letters*, *46*(19), 10754–10763. https://doi.org/10.1029/2019GL082764

Thomas, N. H., Ehlmann, B. L., Rapin, W., Rivera-Hernández, F., Stein, N. T., Frydenvang, J., et al. (2020). Hydrogen Variability in the Murray Formation, Gale Crater, Mars. *Journal of Geophysical Research: Planets*. https://doi.org/10.1029/2019JE006289

Thompson, L. M., Berger, J. A., Spray, J. G., Fraeman, A. A., McCraig, M. A., O'Connell-Cooper, C. D., et al. (2020). APXS-Derived Compositional Characteristics of Vera Rubin Ridge and Murray Formation, Gale Crater, Mars: Geochemical Implications for the Origin of the Ridge. *Journal of Geophysical Research: Planets*, *125*(10). https://doi.org/10.1029/2019JE006319

Tonui, E., Eggleton, T., & Taylor, G. (2003). Micromorphology and chemical weathering of a K-rich trachyandesite and an associated sedimentary cover (Parkes, SE Australia). *CATENA*, *53*(2), 181–207. https://doi.org/10.1016/S0341-8162(02)00200-X

Thorpe, M., et al., (2022), The Mineralogy and Sedimentary History of the Glen Torridon Region, as detailed by the Mars Science Laboratory CheMin Instrument. *Journal of Geophysical research: Planets* (GT Special Issue Paper), in review.

Treiman, A. H., Downs, R. T., Ming, D. W., Morris, R. V., Thorpe, M. T. et al. (2021) Possible Detection of a Jahnsite-Whiteite Group Phosphate Mineral by MSL CheMin in Glen Torridon, Gale Crater, Mars, Presented at the 52nd Lunar and Planetary Science Conference, The Woodlands, TX, Abstract 1200.

Turner, S. M. R., Bridges, J. C., Grebby, S., & Ehlmann, B. L. (2016). Hydrothermal activity recorded in post Noachian-aged impact craters on Mars. *Journal of Geophysical Research: Planets*, *121*(4), 608–625. https://doi.org/10.1002/2015JE004989

Turner, S. M. R., Schwenzer, S. P., Bridges, J. C., Rampe, E. B., Bedford, C. C., Achilles, C. N., et al. (2021). Early diagenesis at and below Vera Rubin ridge, Gale crater, Mars. *Meteoritics & Planetary Science*, maps.13748. https://doi.org/10.1111/maps.13748

Vaniman, D., Dyar, M. D., Wiens, R., Ollila, A., Lanza, N., Lasue, J., et al. (2012). Ceramic ChemCam Calibration Targets on Mars Science Laboratory. *Space Science Reviews*, *170*(1–4), 229–255. https://doi.org/10.1007/s11214-012-9886-0

Vaniman, D. T., Martínez, G. M., Rampe, E. B., Bristow, T. F., Blake, D. F., Yen, A. S., et al. (2018). Gypsum, bassanite, and anhydrite at Gale crater, Mars. *American Mineralogist*, *103*(7), 1011–1020. https://doi.org/10.2138/am-2018-6346

Wan, X., Hu, Q., & Liao, M. (2017). Salt crystallization in cold sulfate saline soil. *Cold Regions Science and Technology*, *137*, 36–47. https://doi.org/10.1016/j.coldregions.2017.02.007

Warren, J. K. (2016). Evaporites. Cham: Springer International Publishing. https://doi.org/10.1007/978-3-319-13512-0

West, I. M., Ali, Y. A., & Hilmy, M. E. (1979). Primary gypsum nodules in a modern sabkha on the Mediterranean coast of Egypt. *Geology*, *7*, 354–358.

Wiens, R. C., Maurice, S., Barraclough, B., Saccoccio, M., Barkley, W. C., Bell, J. F., et al. (2012). The ChemCam Instrument Suite on the Mars Science Laboratory (MSL) Rover: Body Unit and Combined System Tests. *Space Science Reviews*, *170*(1–4), 167–227. https://doi.org/10.1007/s11214-012-9902-4

Wiens, R. C., Maurice, S., Lasue, J., Forni, O., Anderson, R. B., Clegg, S., et al. (2013). Pre-flight calibration and initial data processing for the ChemCam laser-induced breakdown spectroscopy instrument on the Mars Science Laboratory rover. *Spectrochimica Acta Part B: Atomic Spectroscopy*, *82*, 1–27. https://doi.org/10.1016/j.sab.2013.02.003

Wiens, R. C., Maurice, S., & MSL Science Team. (2015). ChemCam: Chemostratigraphy by the First Mars Microprobe. *Elements*, *11*(1), 33–38. https://doi.org/10.2113/gselements.11.1.33

Wiens, R. C., Rubin, D. M., Goetz, W., Fairén, A. G., Schwenzer, S. P., Johnson, J. R., et al. (2017). Centimeter to decimeter hollow concretions and voids in Gale Crater sediments, Mars. *Icarus*, *289*, 144–156. https://doi.org/10.1016/j.icarus.2017.02.003

ROGER WIENS. (2021a). MSL CHEMCAM LASER INDUCED BREAKDOWN SPECTROMETER EDR V1.0 [Data set]. NASA Planetary Data System. https://doi.org/10.17189/1519439

ROGER WIENS. (2021b). MSL MARS CHEMCAM LIBS SPECTRA 4/5 RDR V1.0 [Data set]. NASA Planetary Data System. https://doi.org/10.17189/1519485

ROGER WIENS. (2021c). MSL CHEMCAM REMOTE MICRO IMAGING CAMERA EDR V1.0 [Data set]. NASA Planetary Data System. https://doi.org/10.17189/1519456

ROGER WIENS. (2021d). MSL MARS CHEMCAM REMOTE MICRO-IMAGER CAMERA 5 RDR V1.0 [Data set]. NASA Planetary Data System. https://doi.org/10.17189/1519494

Williams, F. A., Kelley, S. P., Gilmour, I., Jolley, D. W., Gilmour, M. (2013) The Boltysh Impact Crater, Ukraine: Smectites from the Crater-fill Suevites, presented at the European Planetary Science Congress 2013, vol 8, EPSC2013-305. https://meetingorganizer.copernicus.org/EPSC2013/EPSC2013-305.pdf

Worden, R. H. "Halogen Elements in Sedimentary Systems and Their Evolution During Diagenesis" in Harlov, D. E., & Aranovich, L. (Eds.). (2018). The Role of Halogens in Terrestrial and Extraterrestrial Geochemical Processes. Cham: Springer International Publishing. Pp. 185 https://doi.org/10.1007/978-3-319-61667-4

Wu, D., Lai, Y., & Zhang, M. (2017). Thermo-hydro-salt-mechanical coupled model for saturated porous media based on crystallization kinetics. *Cold Regions Science and Technology*, *133*, 94–107. https://doi.org/10.1016/j.coldregions.2016.10.012

Yao, W., & Millero, F. J. (1996). Adsorption of Phosphate on Manganese Dioxide in Seawater. *Environmental Science & Technology*, *30*(2), 536–541. https://doi.org/10.1021/es950290x

Yen, A. S., Ming, D. W., Vaniman, D. T., Gellert, R., Blake, D. F., Morris, R. V., et al. (2017). Multiple stages of aqueous alteration along fractures in mudstone and sandstone strata in Gale Crater, Mars. *Earth and Planetary Science Letters*, *471*, 186–198. https://doi.org/10.1016/j.epsl.2017.04.033

Yingst, R. A., Edgett, K. S., Kennedy, M. R., Krezoski, G. M., McBride, M. J., Minitti, M. E., et al. (2016). MAHLI on Mars: lessons learned operating a geoscience camera on a landed payload robotic arm. *Geoscientific Instrumentation, Methods and Data Systems*, *5*(1), 205–217. https://doi.org/10.5194/gi-5-205-2016

Zhang, M., & Karathanasis, A. D. (1997). Characterization of Iron-Manganese Concretions in Kentucky Alfisols with Perched Water Tables. *Clays and Clay Minerals*, *45*(3), 428–439.

**Supporting Information References**

Anderson, R. B., Finch, N, Clegg, S., Graff, T., Aneece, I., Morris, R. V. (2019) The Python Hyperspectral Analysis Tool (PyHAT) and Laser-Induced Breakdown Spectroscopy Spectral Database, Presented at the 4th Planetary Data Workshop, Abstract 7101. https://www.hou.usra.edu/meetings/planetdata2019/pdf/7101.pdf

Anderson, R. B. et al. (2020) The Python Hyperspectral Analysis Tool. https://github.com/USGS-Astrogeology/PyHAT; https://github.com/USGS Astrogeology/PyHAT_Point_Spectra_GUI

Boyle, F. W., & Lindsay, W. L. (1986). Manganese Phosphate Equilibrium Relationships in Soils. *Soil Science Society of America Journal*, *50*(3), 588–593. https://doi.org/10.2136/sssaj1986.03615995005000030009x

Payré, V., et al. (2017b) Review of trace and minor elements analysed by ChemCam: detection and Quantification using laser induced breakdown spectroscopy, presented at 48th Lunar and Planetary Science Conference, The Woodlands, TX, Abstract 1963.

Pauli Virtanen, Ralf Gommers, Travis E. Oliphant, Matt Haberland, Tyler Reddy, David Cournapeau, Evgeni Burovski, Pearu Peterson, Warren Weckesser, Jonathan Bright, Stéfan J. van der Walt, Matthew Brett, Joshua Wilson, K. Jarrod Millman, Nikolay Mayorov, Andrew R. J. Nelson, Eric Jones, Robert Kern, Eric Larson, CJ Carey, İlhan Polat, Yu Feng, Eric W. Moore, Jake VanderPlas, Denis Laxalde, Josef Perktold, Robert Cimrman, Ian Henriksen, E.A. Quintero, Charles R Harris, Anne M. Archibald, Antônio H. Ribeiro, Fabian Pedregosa, Paul van Mulbregt, and SciPy 1.0 Contributors. (2020) SciPy 1.0: Fundamental Algorithms for Scientific Computing in Python. *Nature Methods*, *17*(3), 261-272.

**Figure 1.**

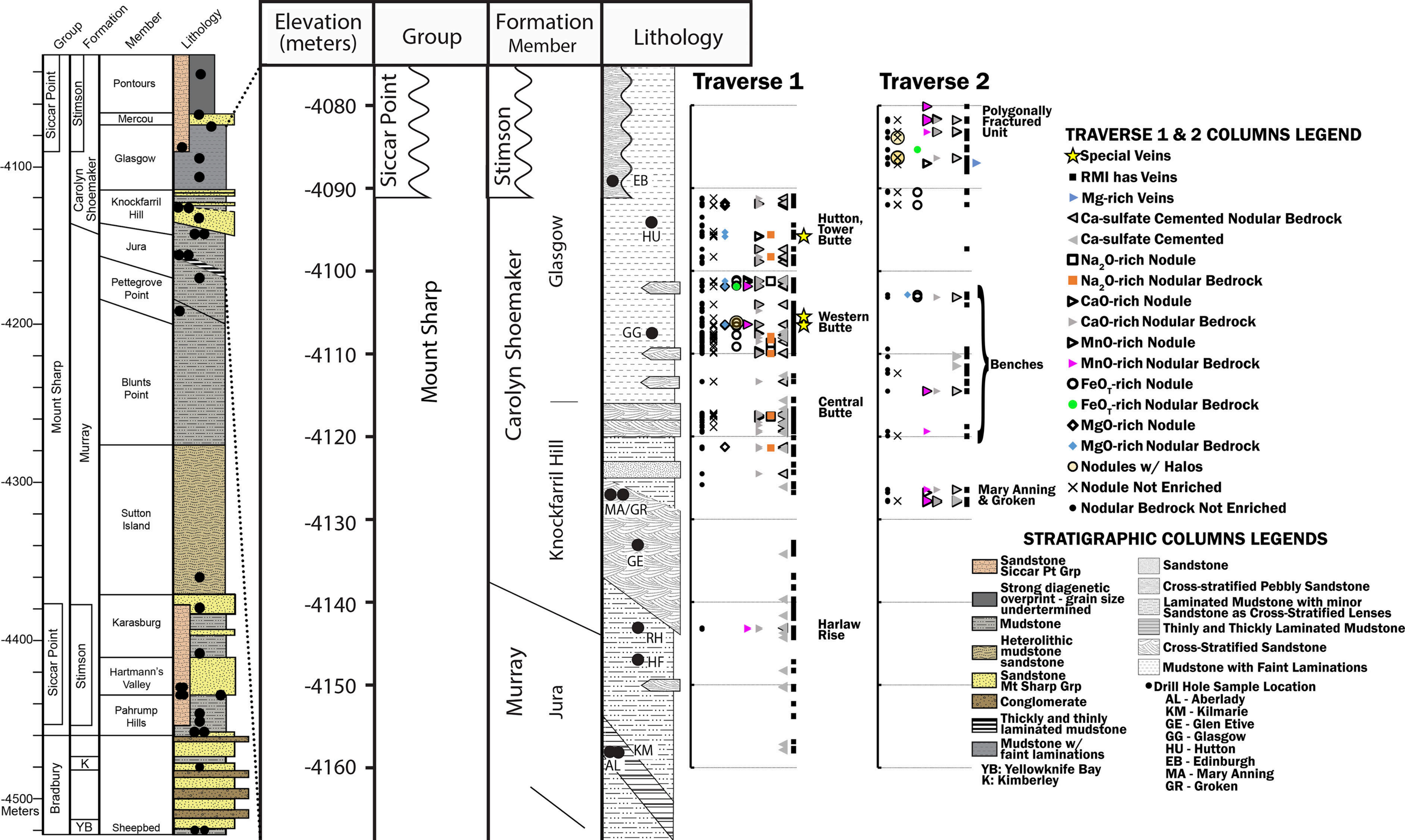
Group
Formation
Member
Lithology
Elevation (meters)
Traverse 1
Traverse 2
Siccar Point
Stimson
Carolyn Shoemaker
Murray
Mount Sharp
Bradbury
Pontours
Mercou
Glasgow
Knockfarril Hill
Jura
Pettegrove Point
Blunts Point
Sutton Island
Karasburg
Hartmann's Valley
Pahrump Hills
K
YB
Sheepbed
-4080
-4090
-4100
-4110
-4120
-4130
-4140
-4150
-4160
-4200
-4300
-4400
-4500
Meters
EB
HU
GG
MA/GR
GE
RH
HF
KM
AL
Hutton, Tower Butte
Western Butte
Central Butte
Harlaw Rise
Polygonally Fractured Unit
Benches
Mary Anning & Groken
TRAVERSE 1 & 2 COLUMNS LEGEND
Special Veins
RMI has Veins
Mg-rich Veins
Ca-sulfate Cemented Nodular Bedrock
Ca-sulfate Cemented
$Na_2O$-rich Nodule
$Na_2O$-rich Nodular Bedrock
CaO-rich Nodule
CaO-rich Nodular Bedrock
MnO-rich Nodule
MnO-rich Nodular Bedrock
$FeO_T$-rich Nodule
$FeO_T$-rich Nodular Bedrock
MgO-rich Nodule
MgO-rich Nodular Bedrock
Nodules w/ Halos
Nodule Not Enriched
Nodular Bedrock Not Enriched
STRATIGRAPHIC COLUMNS LEGENDS
Sandstone Siccar Pt Grp
Strong diagenetic overprint - grain size undertermined
Mudstone
Heterolithic mudstone sandstone
Sandstone Mt Sharp Grp
Conglomerate
Thickly and thinly laminated mudstone
Mudstone w/ faint laminations
YB: Yellowknife Bay
K: Kimberley
Sandstone
Cross-stratified Pebbly Sandstone
Laminated Mudstone with minor Sandstone as Cross-Stratified Lenses
Thinly and Thickly Laminated Mudstone
Cross-Stratified Sandstone
Mudstone with Faint Laminations
Drill Hole Sample Location
AL - Aberlady
KM - Kilmarie
GE - Glen Etive
GG - Glasgow
HU - Hutton
EB - Edinburgh
MA - Mary Anning
GR - Groken

**Figure 2.**

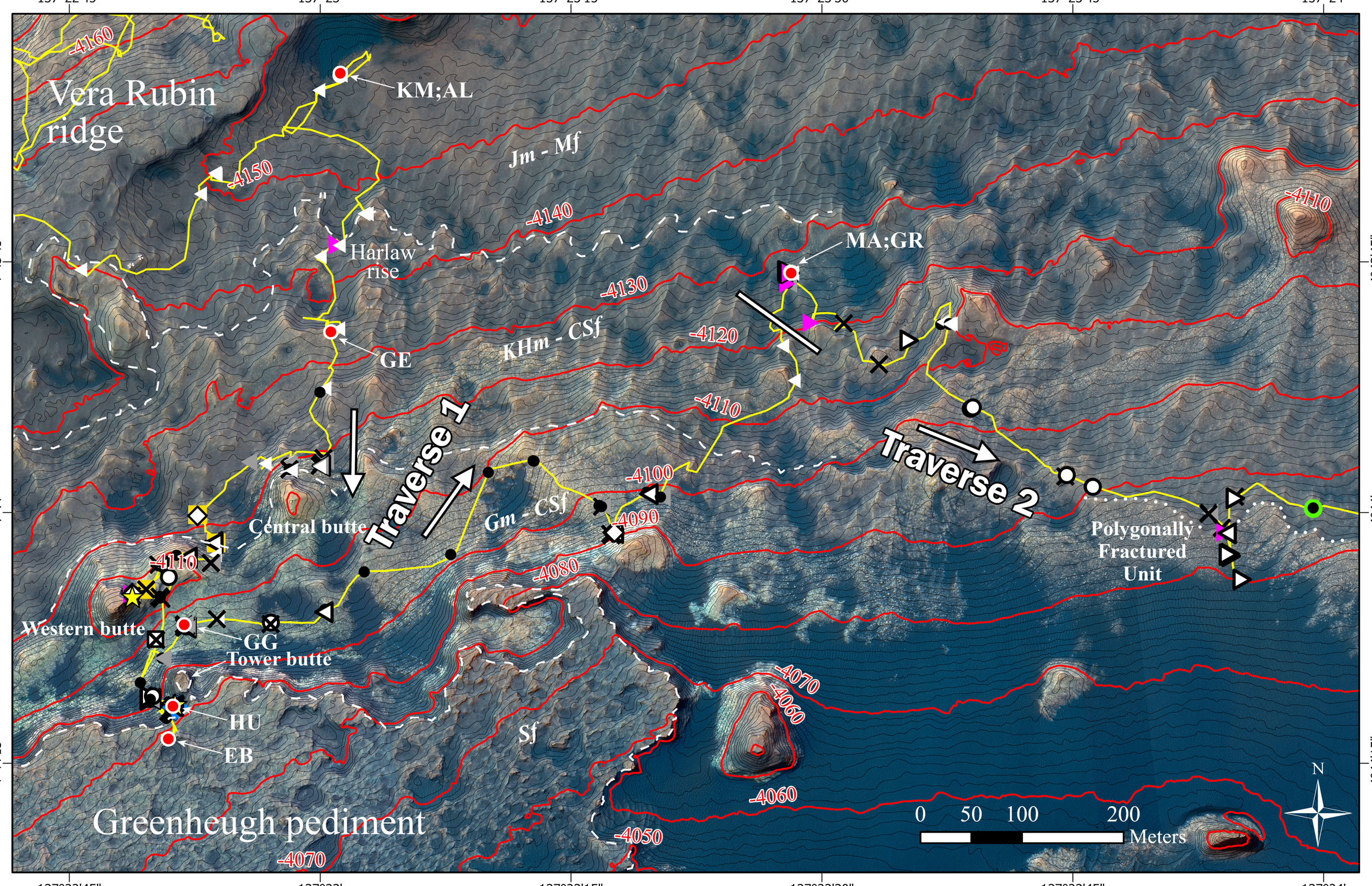


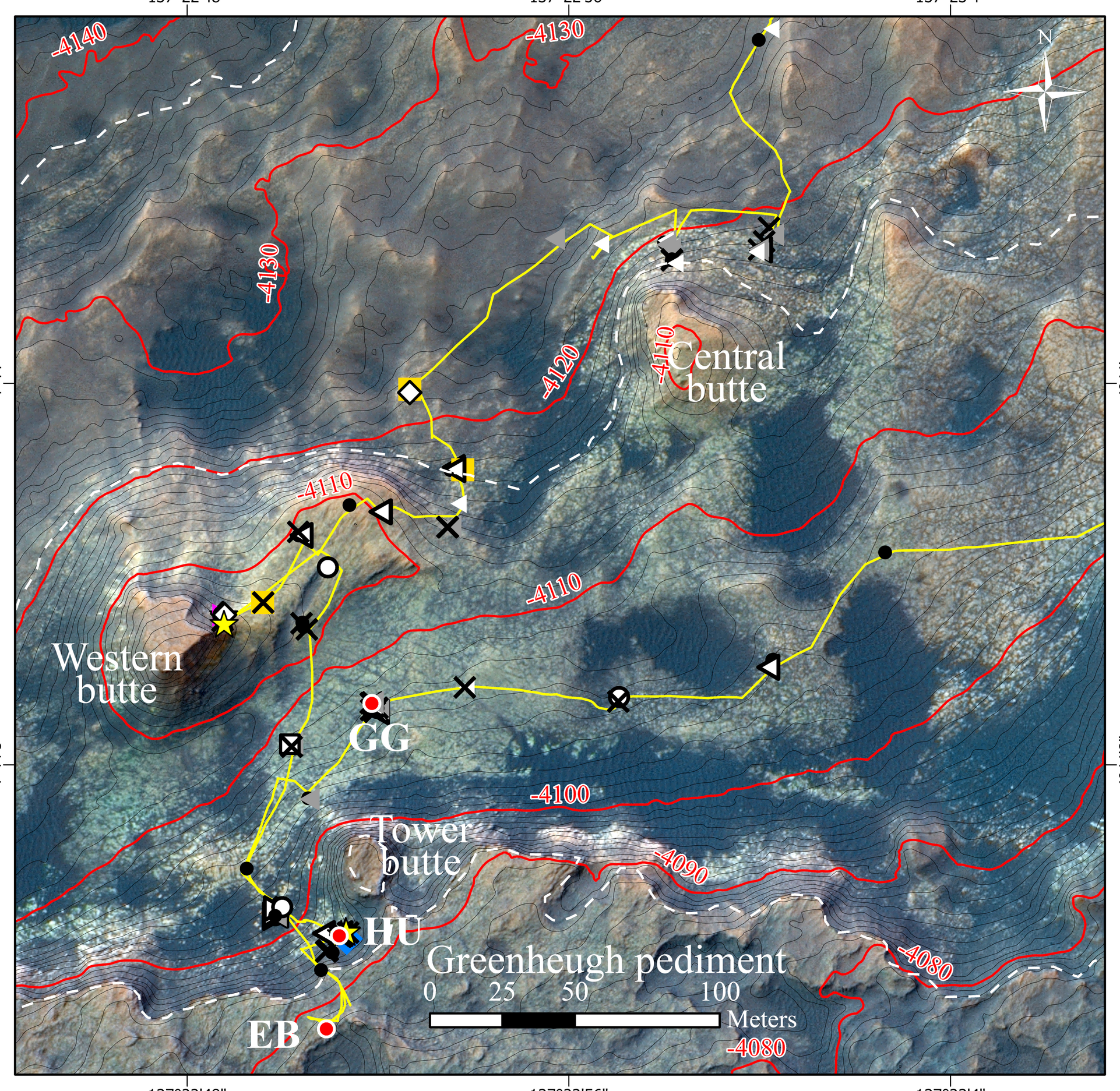


**MAP LEGEND**

- 1 m contours
- 10 m contours
- Rover Traverse Route
- Stratigraphic Boundaries
- Drill Hole Locations
- Special veins
- Ca-sulfate cemented non-nodular bedrock
- $Na_2O$-rich Nodule
- $Na_2O$-rich Nodular Bedrock
- CaO-rich Nodule
- CaO-rich Nodular Bedrock
- MnO-rich Nodule
- MnO-rich Nodular Bedrock
- $FeO_T$-rich Nodule
- $FeO_T$-rich Nodular Bedrock
- MgO-rich Nodule
- MgO-rich Nodular Bedrock
- Nodule Not Enriched
- Nodular Bedrock Not Enriched

**LABEL ABBREVIATIONS**

Drill holes
KM - Kilmarie
AL - Aberlady
GE - Glen Etive
GG - Glasgow
HU - Hutton
EB - Edinburgh
MA - Mary Anning
GR - Groken

Stratigraphy
Jm - Jura member
Mf - Murray formation
KHm - Knockfarril Hill member
CSf - Carolyn Shoemaker formation
Gm - Glasgow member
Sf - Stimson formation

**Figure 3.**

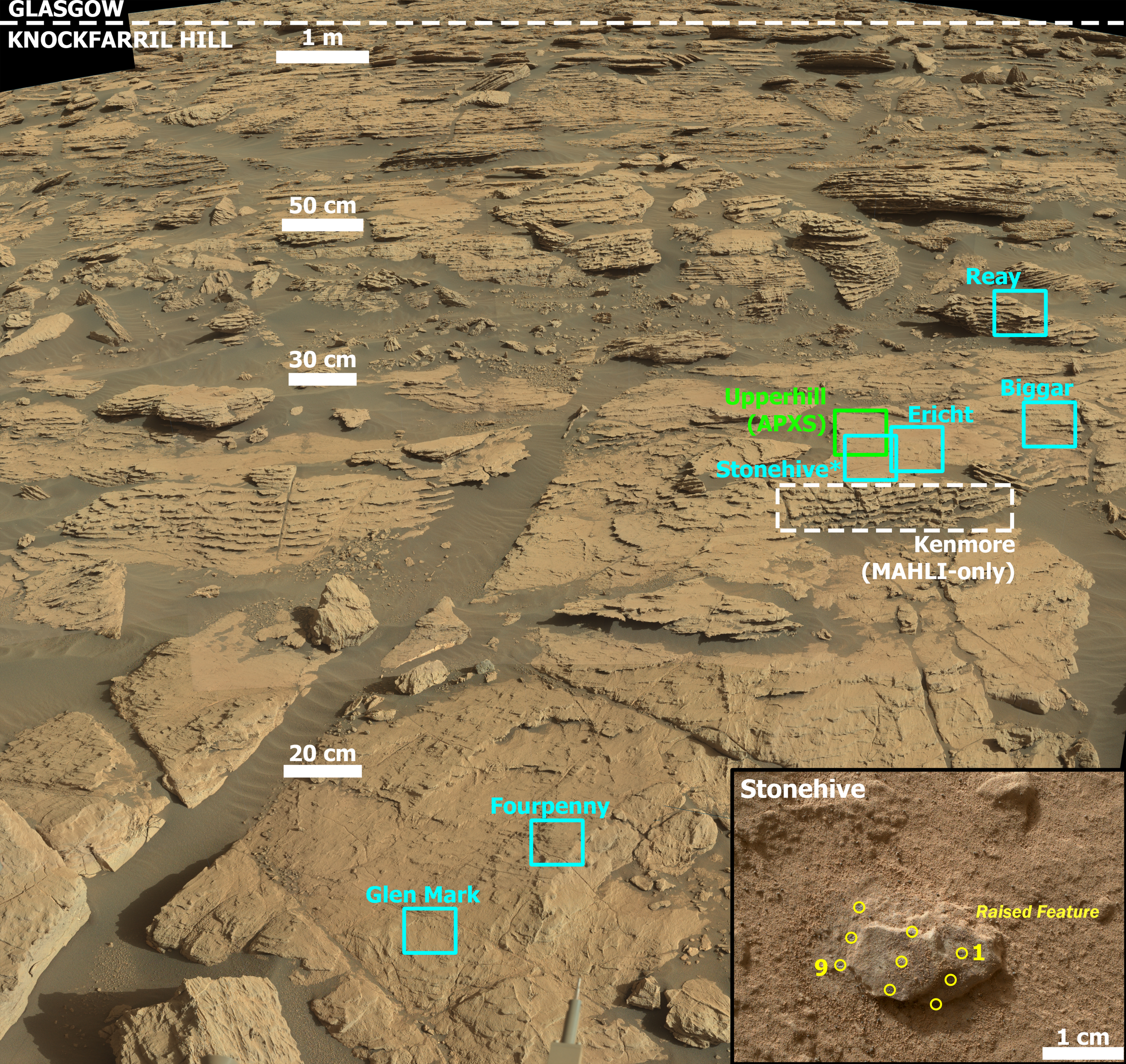
GLASGOW
KNOCKFARRIL HILL
1 m
50 cm
30 cm
20 cm
Reay
Biggar
Upperhill
(APXS)
Ericht
Stonehive*
Kenmore
(MAHLI-only)
Fourpenny
Glen Mark
Stonehive
Raised Feature
1
9
1 cm

**Figure 4.**

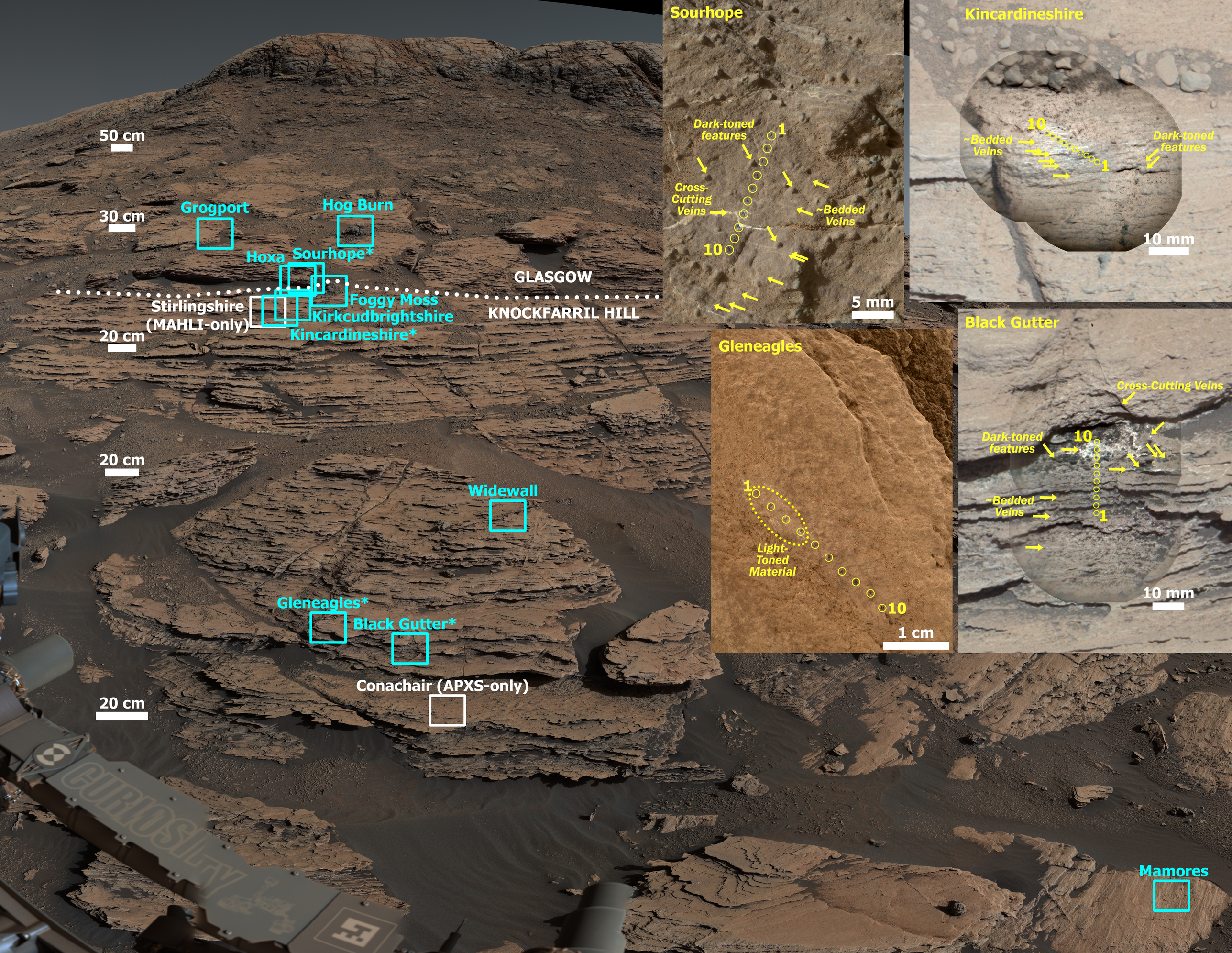
50 cm
30 cm
20 cm
20 cm
20 cm
Grogport
Hog Burn
Hoxa
Sourhope*
GLASGOW
Stirlingshire
(MAHLI-only)
Foggy Moss
Kirkcudbrightshire
KNOCKFARRIL HILL
Kincardineshire*
Widewall
Gleneagles*
Black Gutter*
Conachair (APXS-only)
Mamores
Sourhope
Dark-toned features
1
Cross-Cutting Veins
~Bedded Veins
10
5 mm
Kincardineshire
10
~Bedded Veins
Dark-toned features
1
10 mm
Gleneagles
1
Light-Toned Material
10
1 cm
Black Gutter
Cross-Cutting Veins
Dark-toned features
10
~Bedded Veins
1
10 mm

**Figure 5.**

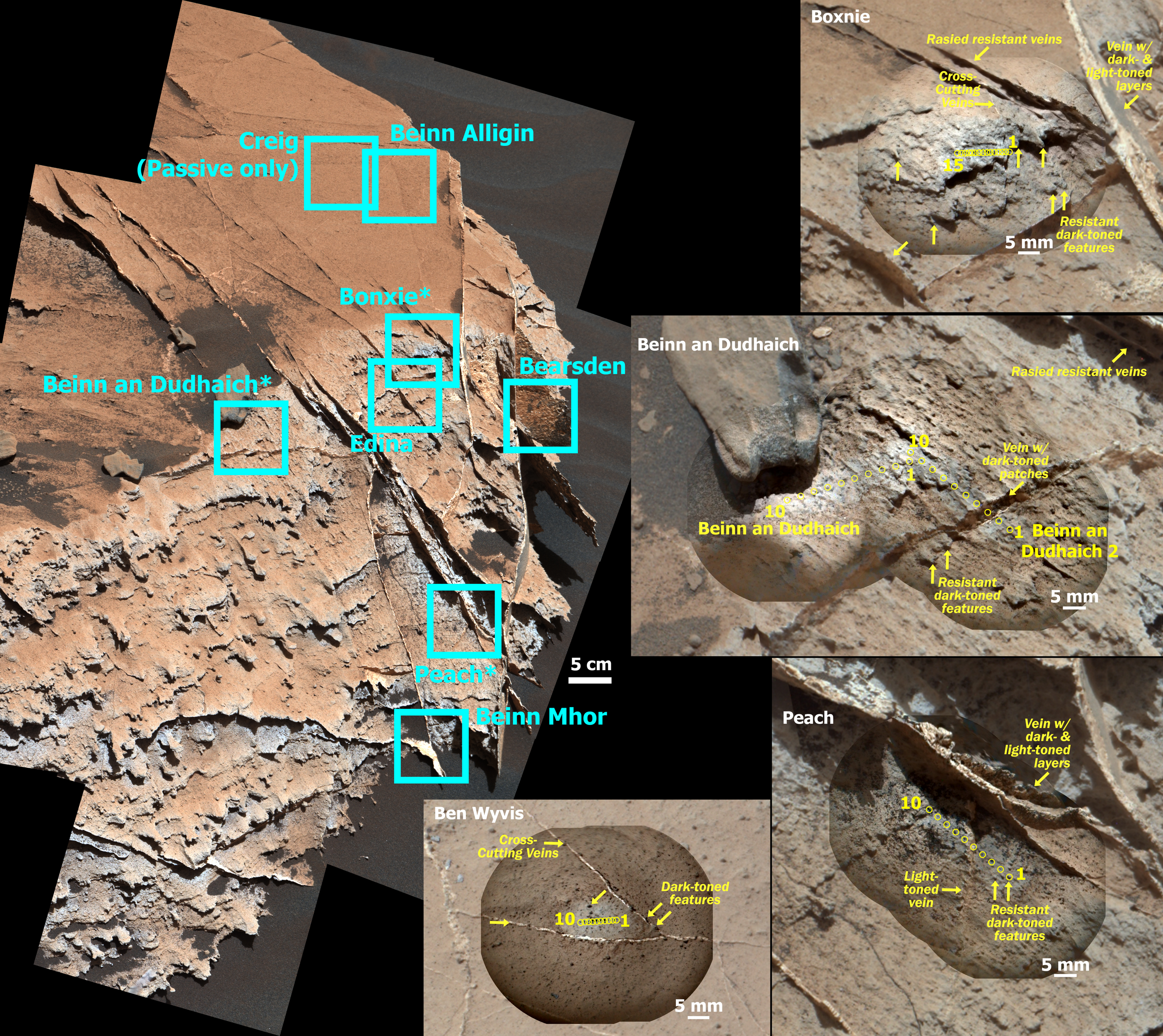
Creig
(Passive only)
Beinn Alligin
Bonxie*
Beinn an Dudhaich*
Bearsden
Edina
Peach*
Beinn Mhor
5 cm
Boxnie
Rasied resistant veins
Cross-Cutting Veins
Vein w/ dark- & light-toned layers
1
15
Resistant dark-toned features
5 mm
Beinn an Dudhaich
Rasied resistant veins
10
1
Vein w/ dark-toned patches
10
Beinn an Dudhaich
1 Beinn an Dudhaich 2
Resistant dark-toned features
5 mm
Ben Wyvis
Cross-Cutting Veins
Dark-toned features
10
1
5 mm
Peach
Vein w/ dark- & light-toned layers
10
1
Light-toned vein
Resistant dark-toned features
5 mm

**Figure 6.**

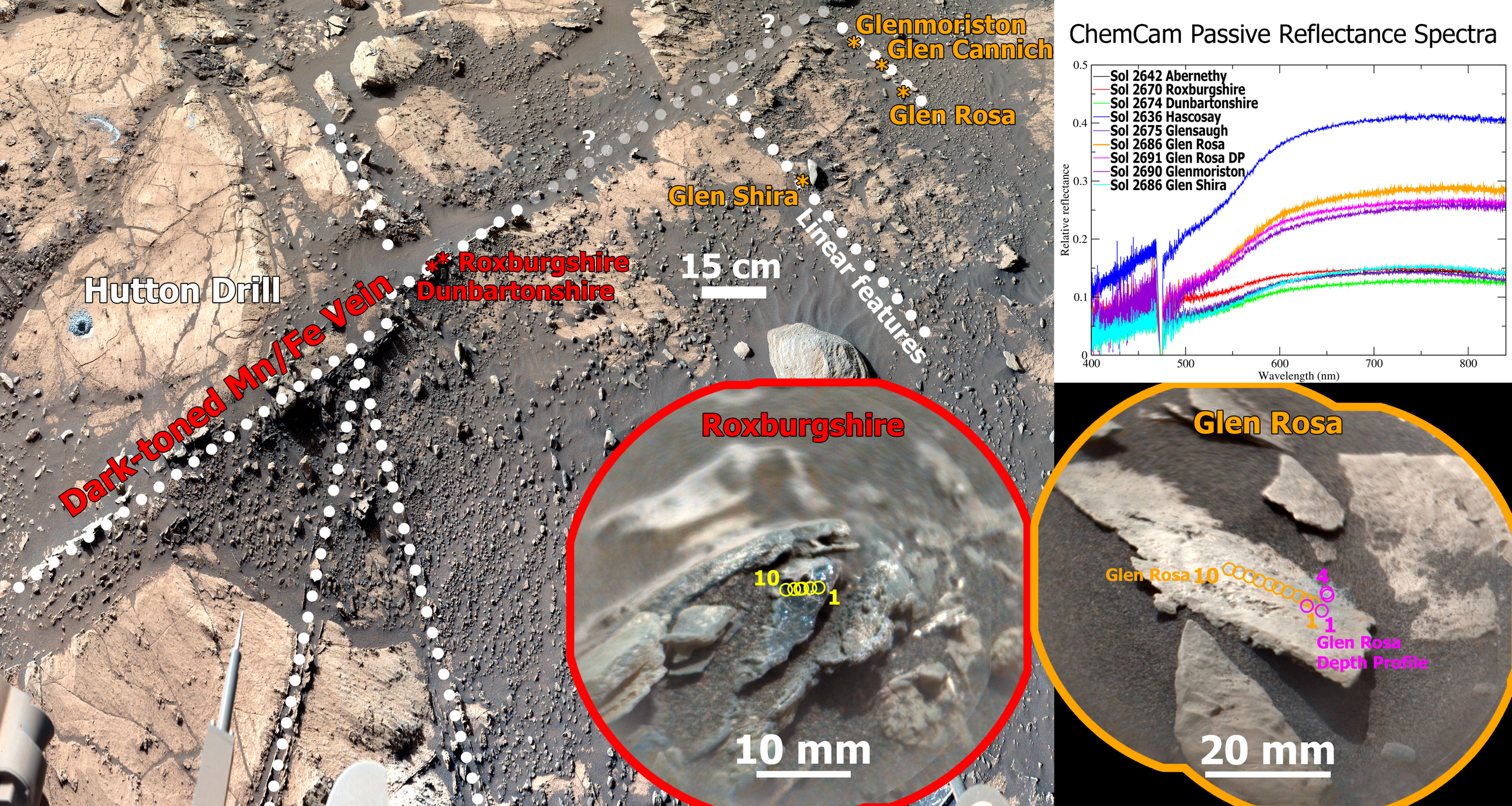
Glenmoriston
Glen Cannich
Glen Rosa
Glen Shira
Linear features
Roxburgshire
Dunbartonshire
15 cm
Hutton Drill
Dark-toned Mn/Fe vein
Roxburgshire
10
1
10 mm
ChemCam Passive Reflectance Spectra
Sol 2642 Abernethy
Sol 2670 Roxburgshire
Sol 2674 Dunbartonshire
Sol 2636 Hascosay
Sol 2675 Glensaugh
Sol 2686 Glen Rosa
Sol 2691 Glen Rosa DP
Sol 2690 Glenmoriston
Sol 2686 Glen Shira
Relative reflectance
Wavelength (nm)
0
0.1
0.2
0.3
0.4
0.5
400
500
600
700
800
Glen Rosa
Glen Rosa 10
4
1
Glen Rosa
Depth Profile
20 mm

**Figure 7.**

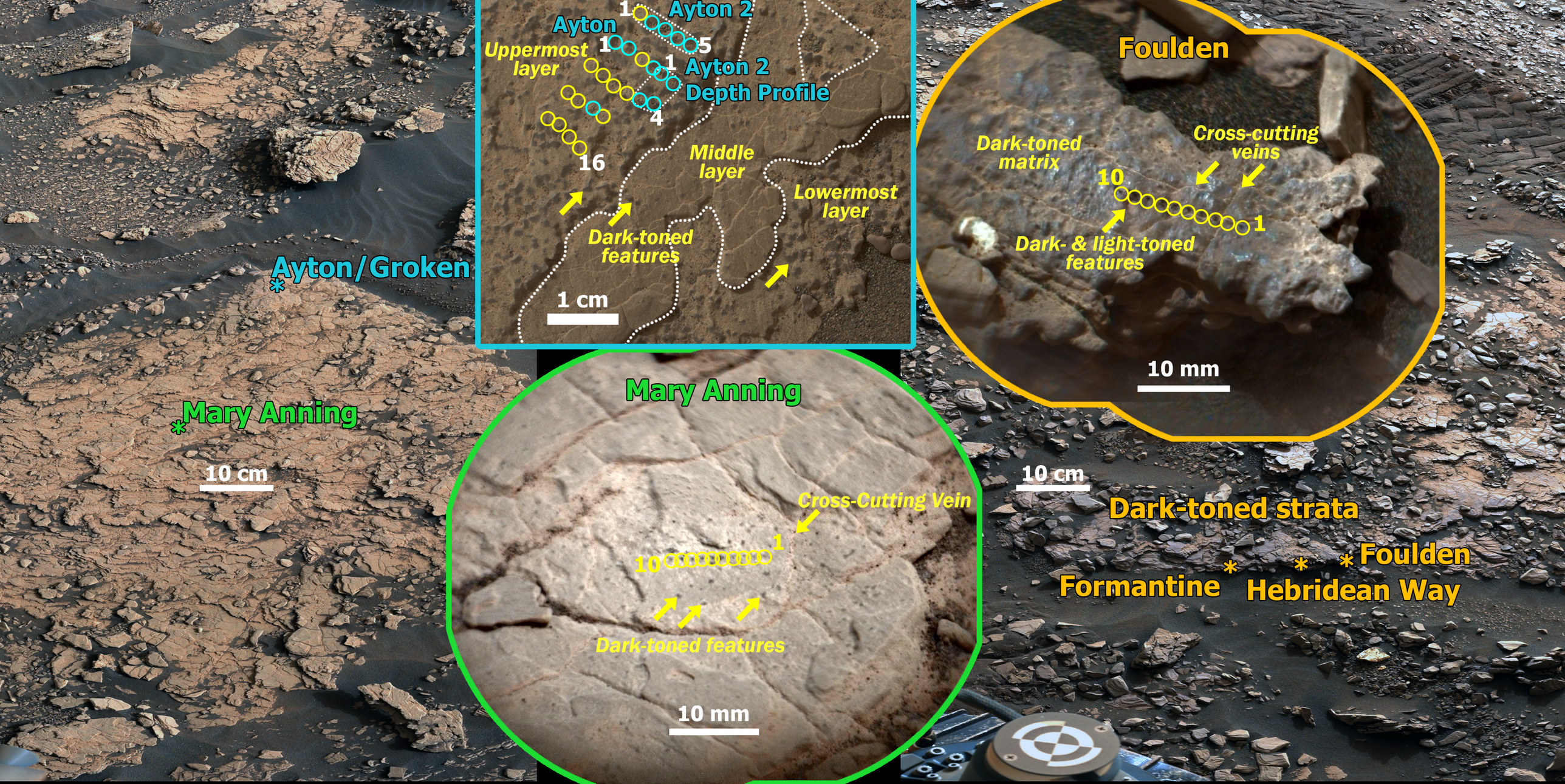
Ayton 2
Ayton
1
1
5
Uppermost layer
1
Ayton 2
Depth Profile
4
16
Middle layer
Lowermost layer
Dark-toned features
1 cm
Foulden
Dark-toned matrix
Cross-cutting veins
10
1
Dark- & light-toned features
10 mm
Ayton/Groken
Mary Anning
10 cm
Mary Anning
Cross-Cutting Vein
1
10
Dark-toned features
10 mm
10 cm
Dark-toned strata
Foulden
Formantine
Hebridean Way

**Figure 8.**

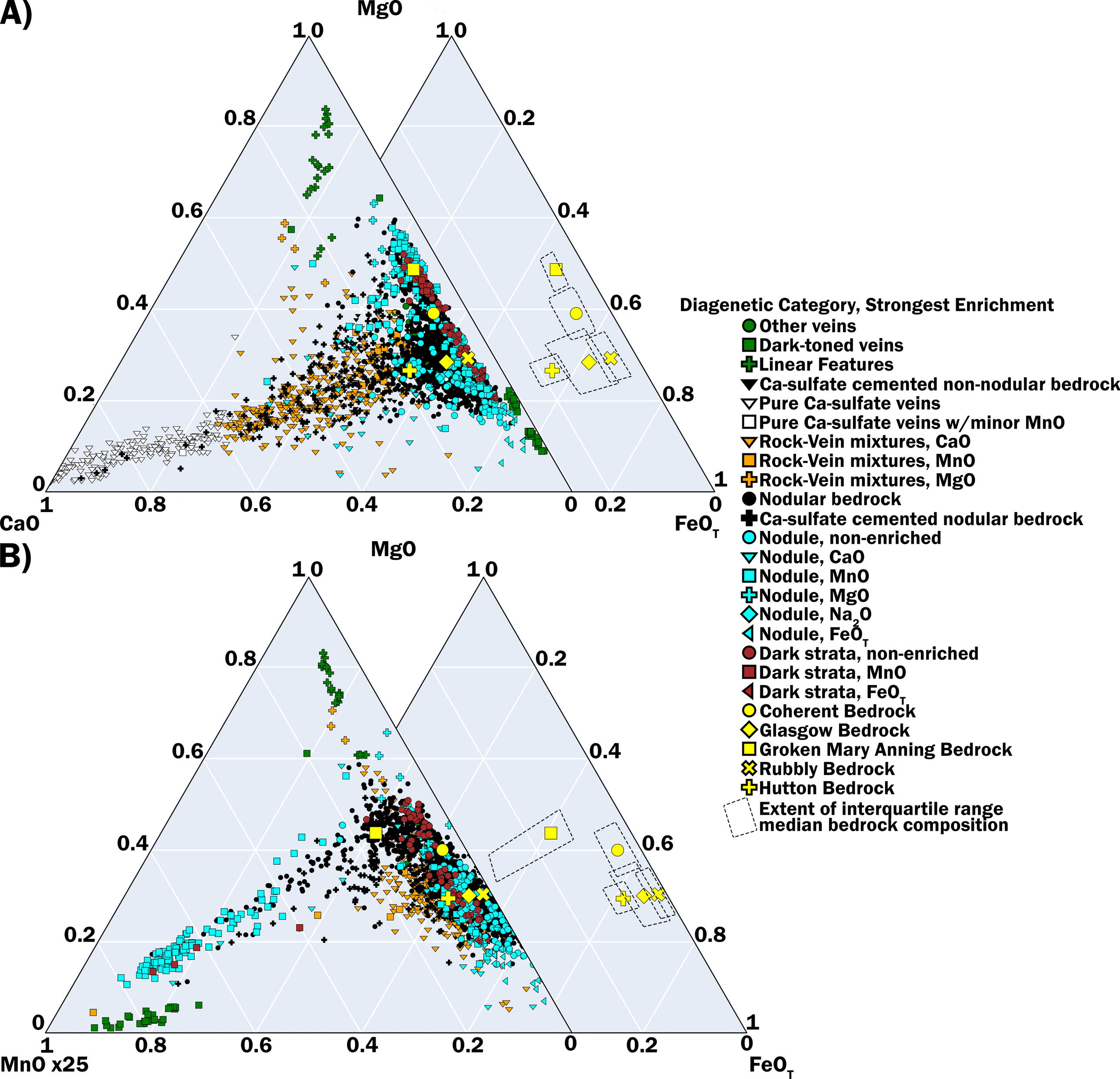
A)
MgO
CaO
FeO$_T$
B)
MgO
MnO x25
FeO$_T$
Diagenetic Category, Strongest Enrichment
Other veins
Dark-toned veins
Linear Features
Ca-sulfate cemented non-nodular bedrock
Pure Ca-sulfate veins
Pure Ca-sulfate veins w/minor MnO
Rock-Vein mixtures, CaO
Rock-Vein mixtures, MnO
Rock-Vein mixtures, MgO
Nodular bedrock
Ca-sulfate cemented nodular bedrock
Nodule, non-enriched
Nodule, CaO
Nodule, MnO
Nodule, MgO
Nodule, Na$_2$O
Nodule, FeO$_T$
Dark strata, non-enriched
Dark strata, MnO
Dark strata, FeO$_T$
Coherent Bedrock
Glasgow Bedrock
Groken Mary Anning Bedrock
Rubbly Bedrock
Hutton Bedrock
Extent of interquartile range median bedrock composition